DESIGN AND IMPLEMENTATION OF A METEOR TRACKING RETROFIT SYSTEM FOR THE HF RADAR AT KODIAK ISLAND, ALASKA

A

Thesis

Presented to the Faculty of the University of
Alaska Fairbanks in Partial Fulfillment of the
Requirements for the Degree of

MASTER OF SCIENCE

By
Richard Todd Parris, B.S.

Fairbanks, Alaska
August 2003

© 2003 Richard Todd Parris

Reproduced with permission of the copyright owner. Further reproduction prohibited without permission.

UMI Number: 1417023

Copyright 2003 by
Parris, Richard Todd

All rights reserved.

INFORMATION TO USERS

The quality of this reproduction is dependent upon the quality of the copy submitted. Broken or indistinct print, colored or poor quality illustrations and photographs, print bleed-through, substandard margins, and improper alignment can adversely affect reproduction.

In the unlikely event that the author did not send a complete manuscript and there are missing pages, these will be noted. Also, if unauthorized copyright material had to be removed, a note will indicate the deletion.

UMI®

UMI Microform 1417023
Copyright 2004 by ProQuest Information and Learning Company.
All rights reserved. This microform edition is protected against unauthorized copying under Title 17, United States Code.

ProQuest Information and Learning Company
300 North Zeeb Road
P.O. Box 1346
Ann Arbor, MI 48106-1346

Reproduced with permission of the copyright owner. Further reproduction prohibited without permission.

DESIGN AND IMPLEMENTATION OF A METEOR TRACKING RETROFIT SYSTEM FOR THE HF RADAR AT KODIAK ISLAND, ALASKA

By

Richard Todd Parris

RECOMMENDED:

Advisory Committee Chair

Chair, Department of Electrical Engineering

APPROVED:

Dean, College of Science, Engineering, and Mathematics

Dean of the Graduate School

August 18, 2003

Date

Reproduced with permission of the copyright owner. Further reproduction prohibited without permission.

Abstract

The HF radar at Kodiak Island, Alaska, is part of the SuperDARN network of radars, and was originally designed to detect echoes from ionospheric field-aligned density irregularities. A new digital receiver has been implemented on the radar to allow provide the capabilities required for increased range resolution detection of meteor echoes. A meteor detection algorithm has also been implemented to detect meteor echoes with a range resolution of 4.5 km. The algorithm measures the velocity, range, and altitude of the echoes. This data can be used to derive information about the meteor region winds. The design and implementation of the receiver, the design and implementation of the meteor detection algorithm, and some meteor region wind data derived from the new system are presented.

Reproduced with permission of the copyright owner. Further reproduction prohibited without permission.

Table of Contents

Reproduced with permission of the copyright owner. Further reproduction prohibited without permission.

Reproduced with permission of the copyright owner. Further reproduction prohibited without permission.

Reproduced with permission of the copyright owner. Further reproduction prohibited without permission.

Reproduced with permission of the copyright owner. Further reproduction prohibited without permission.

List of Figures

Reproduced with permission of the copyright owner. Further reproduction prohibited without permission.

Reproduced with permission of the copyright owner. Further reproduction prohibited without permission.

Reproduced with permission of the copyright owner. Further reproduction prohibited without permission.

List of Tables

Reproduced with permission of the copyright owner. Further reproduction prohibited without permission.

Chapter 1: Introduction

In October of 1983, a team at Johns Hopkins University Applied Physical Laboratory, led by R. A. Greenwald, completed the construction of one of the first HF radars designed specifically for mapping large-scale ionospheric convection [Greenwald et al., 1985]. This radar was the first step in developing a multi-national network of HF radars built for the same purpose. This network is known as the Super Dual Auroral Radar Network (SuperDARN). Currently, there are 15 HF radars in the SuperDARN community. Each of these radars is similar in design and capability.

Since these radars started collecting data, there has been what can best be described as 'quasi-random' echoes in the near range gates. These near-range echoes typically have life spans shorter than the usual integration period of the radars and typically have signal-to-noise ratios (SNRs) that vary greatly from one range gate to the next. Within the SuperDARN community, these echoes have been referred to as "grainy near-range echoes" [Hall et al., 1997]. In 1997, Hall et al. performed a detailed analysis on these grainy near-range echoes and identified the echoes as scatter from meteor trails. Hall et al. also showed good correlation between the mesospheric wind data derived from this meteor scatter data and the mesospheric winds measured by a MF radar in Saskatoon, Canada.

When a meteor falls through the earth's atmosphere, the collisions between the molecules of the meteoroid and the molecules of the atmosphere generate enough energy to free electrons. This leaves a trail of ionized gas, or plasma, behind the meteor. Since at the altitudes at which meteoroids ablate, the ion-neutral collision frequency is significantly greater then the ion-gyro frequency, the plasma tends to drift with the surrounding neutral atmosphere. The free electrons in the plasma trail left by the ablating meteor act to reflect (and scatter) incident electromagnetic waves and provide a radar target that can be used to track the neutral winds in the region of the meteor trail. All of the radars in the SuperDARN network see this scatter from meteor trails as identified by

Reproduced with permission of the copyright owner. Further reproduction prohibited without permission.

Hall et al. [1997]. The meteor scatter data in the existing SuperDARN data sets are considered valuable for mesospheric studies and much research has been done to mine useful information from the existing SuperDARN data [e.g. Dai, 2000]. Also, much research has been done to develop algorithms to extract useful information from the meteor scatter data in real-time without changes to the hardware operation of the existing radar systems [e.g. Yukimatu, 2002].

One problem with the analysis of existing meteor scatter data is that the systems were specifically designed to measure ionospheric convection. The range resolutions for which the existing radars were designed to operate are much greater than typical radars used to measure mesospheric winds. In typical operation, the range resolution of all SuperDARN radars is 45 km. This range resolution is sometimes decreased to 15 km if the radars run special operating modes. This presents a problem because at altitudes where meteors ablate, there are often great variations in the wind velocities with respect to altitude within a single range gate. With the coarse range resolutions currently provided by the SuperDARN radars, much information about the neutral wind in meteor ablation altitudes is unresolved.

The existing hardware of the SuperDARN radar receivers limits their capabilities for high spatial resolution with the use of fixed narrow-bandwidth filtering. Most of the receivers on the SuperDARN radars contain two filters, a 3 kHz filter used for 45 km range resolution, and a 10 kHz filter for 15 km range resolution [Lester, et al., 1998]. These filters are far too narrow for the high resolution required to better resolve the altitude variations of the neutral winds in the meteor ablation region. To overcome the limitations imposed by the existing receiver, a new digital receiver has been designed and implemented at the Kodiak Island SuperDARN radar site. The design and implementation of this system are presented. Also, data processing algorithms have been implemented to extract useful information, with high spatial resolutions, from meteor echoes. These algorithms, along with some example meteor and neutral wind data are also presented.

Reproduced with permission of the copyright owner. Further reproduction prohibited without permission.

Chapter 2: Background

To gain a thorough understanding of the design and implementation of the new digital receiver and the capabilities it provides for collecting neutral wind information from meteor scatter, a brief explanation of both meteors and HF radar techniques is presented. Since entire books have been written on both of these subjects, the explanation presented is brief, as a detailed explanation of both meteors and HF radar techniques is beyond the scope of this thesis. For sake of brevity, some explanations are oversimplified. For a detailed understanding of both meteors and radar, please refer to an appropriate text such as Meteor Science and Engineering by McKinley [1964] and Radar Principles by Levanon [1988].

Meteors

In his text, Meteor Science and Engineering, McKinley describes a meteor as a "streak of light or shooting star that is seen in the night sky when a small object, known as a meteoroid, enters the earth's atmosphere at high speed and dissipates its energy and substance in a brief blaze [1964]." People typically think of meteors as the occasional shooting star seen from the corner of the eye while gazing at the night sky, or the streaks of light seen when the family gathers to watch a meteor shower. Most meteors, however, are not visible to the naked eye. Despite the fact that most people consider it a rare and special occasion to view a meteor, McKinley states that, "over the entire earth it is estimated that from one to two hundred million visible meteors burn themselves out daily in our upper atmosphere [1964]."

The interplanetary regions of our solar system are filled with debris. This debris ranges from microscopic particles to huge chunks of rock and metal. When a piece of this debris enters the earth's atmosphere it is termed a meteorite. As the meteorite falls through ever denser atmosphere, the greater frequency of collisions between the atmospheric particles and the meteorite creates increasing frictional heating. When this

Reproduced with permission of the copyright owner. Further reproduction prohibited without permission.

frictional heating reaches a certain point, the meteorite begins to incandesce and shed mass into the atmosphere. This process is known as ablation. As the meteorite ablates, the frictional energy also strips electrons away from the neutral molecules in the atmosphere. The meteor thus leaves a wake of free electrons and ions in it path. It is this column of plasma left behind a falling meteorite that is referred to as the 'meteor trail'. Because of the electromagnetic wave scattering properties of free electrons, this meteor trail is a good target for radar observations.

Radio properties of Meteor Trails

According to McKinley, the first step in understanding the RF properties of meteor trails in to make some assumptions. One of these assumptions is that a meteor trail is simply a column of free electrons, and that the diameter of the column is much smaller than the wavelength of the interrogating RF signal. Since the RF properties of a given meteor trail depend on the free electrons, meteor trails are categorized by the density of free electrons. The case where the density of electrons in the plasma trail is small enough that the individual electrons can oscillate freely without colliding with other particles is defined as the *underdense* case. McKinley states, "Each electron behaves as if no other were present – secondary radiative and absorptive effects may be neglected. This condition defines the underdense trail." Conversely, if the density of the free electrons in the plasma trail is large such that the electrons do not act as individual scatterers, such that the RF wave does not penetrate the column of plasma, then the meteor trail is said to be *overdense* [McKinley, 1964]. Put simply, if the plasma frequency of the meteor trail is less than the frequency of the incident electromagnetic wave, the meteor trail is said to be underdense. If the plasma frequency of the meteor trail is greater than that of the incident electromagnetic wave, then the trail is considered overdesnse. Underdense meteor echoes are more common than overdense meteor echoes, and they have properties that are more desirable for radar detection and analysis.

Reproduced with permission of the copyright owner. Further reproduction prohibited without permission.

Underdense Meteors

Reflected Electromagnetic Energy

A mathematical model of the underdense trail is presented in McKinley, and is summarized here. To begin the model, the scattering cross section of a single free electron is presented. This will be used to build the scattering cross section of a given underdense trail. The back scatter cross section of a single free electron (assuming back scatter radar) is,

$$\sigma_e = \frac{4\pi e^4}{m^2 c^4} \approx 1\times10^{-28} \text{ [m}^2\text{]} \qquad (1)$$

where e is the charge of an electron, m is the mass of an electron , and c is the speed of light [McKinley, 1964]. All SuperDARN radars and many meteor radars are monostatic radars that use the same antenna array for both transmitting and receiving. A simple model of such geometry is illustrated in Figure 1.

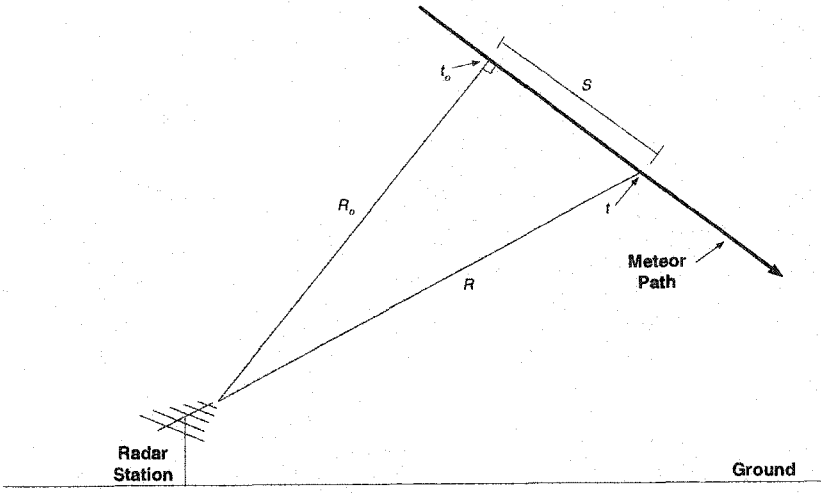

Figure 1: Simplified Geometry of Backscatter from a Meteor Trail Relative to the Radar Station

Reproduced with permission of the copyright owner. Further reproduction prohibited without permission.

Using equation 1 and the geometry of Figure 1, the total power received from the scatter of single free electron is,

$$\Delta P_R = \frac{P_T G^2 \lambda^2 \sigma_e}{64\pi^3 R^4} \tag{2}$$

where P_T is the transmitted power, G is the gain of the antenna (or antenna array), and λ is the wavelength of the interrogating signal [McKinley, 1961]. The backscatter cross section of a free electron is approximately 10^{-28} m^2. Taking q as the number of free electrons per unit length of the meteor trail, the amplitude contribution to the backscattered signal from a differential element of the meteor trail is

$$dA_R = \sqrt{2Z_R \Delta P_R} \cdot q \cdot \sin(2\pi ft - \frac{4\pi R}{\lambda}) ds \tag{3}$$

where Z_R is the impedance of the receiver. Using the approximation $R \approx R_0 + s^2/2R_0$ and the transformations, $\chi = 2\pi ft - 4\pi R_0/\lambda$ and $2s = x(R_0\lambda)^{1/2}$ and integrating over the length of meteor trail seen by the radar, s, the signal at the receiver is

$$A_R = \frac{\sqrt{2Z_R \Delta P_R R_0 \lambda}}{2} q \int \sin\left(\chi - \frac{\pi x^2}{2}\right) dx . \tag{4}$$

Equation 4 can be re-written as

$$A_R = \frac{\sqrt{2Z_R \Delta P_R R_0 \lambda}}{2} q(C\sin(\chi) - S\cos(\chi)) \tag{5}$$

where C and S are Fresnel integrals of argument $2\pi ft - 4\pi R_o/\lambda$. Using the relation, $P_R = A_R^2/2r$, and substituting equation 2 for ΔP_R, the total power received is given by,

$$P_R = \frac{P_T G^2 \lambda^3 \sigma_e}{128\pi^3 R_o^3} \left[\frac{C^2 + S^2}{2}\right] q^2 \tag{6}$$

[McKinley]. This equation is very much analogous to the equations describing the diffraction of light about a hard edge. For this reason, the electromagnetic energy reflected from an underdense meteor trail is often called a 'diffraction echo'. It should be noted at this point that this development of the diffraction echo from an underdense meteor trail is simplified and does not consider diffusion, electron-ion recombination, turbulence, and wind shears.

Reproduced with permission of the copyright owner. Further reproduction prohibited without permission.

Diffusion Echo

At the altitude of typical radar meteor reflections, diffusion is the largest contributor to modification of the electromagnetic energy reflected from underdense meteor trails. The plasma trail left by a meteoroid falling through the upper atmosphere begins as an approximate line distribution of plasma in a neutral medium. As time progresses from the creation of the line distribution, the plasma diffuses radially. The differential equation describing the radial diffusion of a plasma is

$$\frac{\partial N}{\partial t} = \frac{D}{r}\frac{\partial}{\partial r}\left(r\frac{\partial N}{\partial r}\right) \tag{7}$$

where N is the volume density at a radius r from the axis of diffusion and D is the ionic diffusion coefficient in meters per second [McKinley, 1961]. A detailed derivation of the diffusion of plasmas and partial plasmas is presented by Chen [1984]. It should be noted here that in the presence of a magnetic field, the magnetic field tends to slow the diffusion rate across the magnetic field lines. A discussion of this phenomenon is presented in the next section.

Applying the constraint that the total number of electrons in a cross sectional slice of the radially diffusing column of electrons is constant to one of the particular solutions to equation 7 yields the solution for volume density as a function of time, t, and radial distance, r, from the axis of diffusion;

$$N(r,t) = \frac{q}{\pi(4Dt + r_0^{\,2})} e^{-\left(\frac{r^2}{4Dt+r_0^{\,2}}\right)} \tag{8}$$

where q is charge, and r_0 is the initial radius of the meteor trail. Equation 8 describes the volume density of electrons as a function of time and radius for a diffusive column of free electrons.

To understand the problem of electromagnetic wave reflection from this diffusing column, some simplifications are made. First, the diffusive column of electrons is considered as a discrete column with increasing radius and decreasing density. Second, a Gaussian density distribution is assumed across the diameter of the meteor trail. The

Reproduced with permission of the copyright owner. Further reproduction prohibited without permission.

effects of radial diffusion on the echo signal can be understood by considering the geometry in Figure 2.

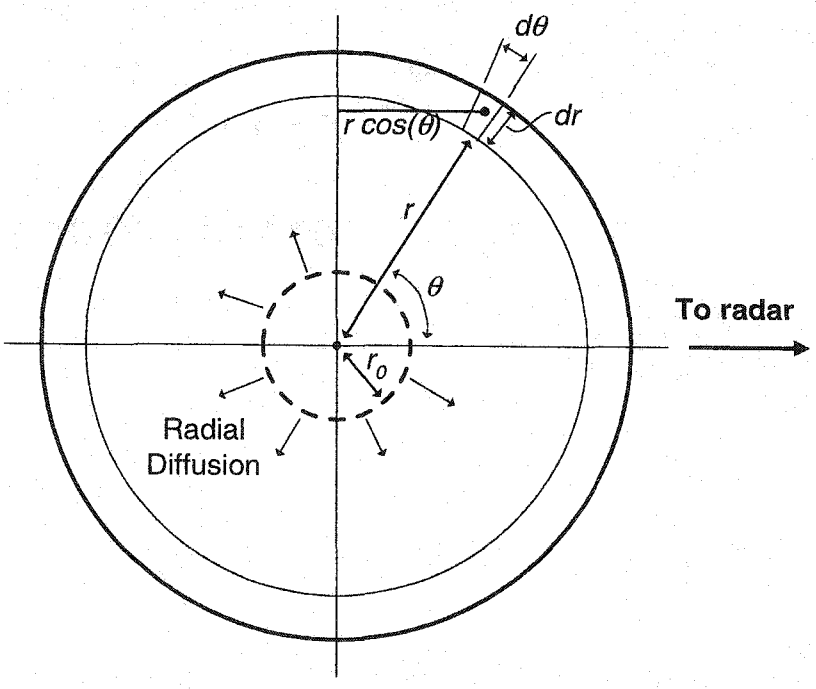

Figure 2: Cross section of ionized meteor trail
[McKinley]

This figure represents a cross sectional slice through the meteor trail at the point of perpendicularity between the interrogating electromagnetic signal and the meteor trail. The trail diffuses radially with time. The phase contribution to the echo signal from a differential element, $r\ dr\ d\theta$, is $\frac{4\pi r}{\lambda}\cos\theta$. Adding this phase to the interrogating signal and integrating over the circumference of the cross sectional slice yields the differential change in the return signal for a certain meteor trail radius, r. This is represented in the equation

$$dA = 2Nrdr\int_0^{\pi}\sin\left(2\pi ft - \frac{4\pi r}{\lambda}\cos\theta\right)d\theta \qquad (9)$$

Expanding and simplifying equation 9 yields

Reproduced with permission of the copyright owner. Further reproduction prohibited without permission.

$$dA = 2\pi N J_0\left(\frac{4\pi r}{\lambda}\right) rdr \sin(2\pi ft) \tag{10}$$

where J_0 is the zeroth-order Bessel function. Equation 18 describes the modification to the echo amplitude related to a change in the radius of the meteor trail. For any trail radius, the overall phase contribution is zero (relative to the center of the trail) and the RF term can be ignored. Integrating for all radii of the meteor trail yields the echo amplitude;

$$A = 2\pi \int_0^\infty N J_0\left(\frac{4\pi r}{\lambda}\right) rdr\,. \tag{11}$$

The amplitude of the echo signal if all of the electrons were at the radial axis is given by

$$A_0 = 2\pi \int_0^\infty N r dr\,. \tag{12}$$

This represents the theoretical initial echo amplitude. The ratio of meteor trail echo amplitude as a function of time relative to the initial echo amplitude is obtained by combining equations 11 and 12 and integrating;

$$\frac{P(t)}{P(0)} = \left(\frac{A}{A_0}\right)^2 = e^{-\left(\frac{32\pi^2 Dt}{\lambda^2}\right)}. \tag{13}$$

If the initial true radius of the meteor trail is considered, then equation 13 becomes

$$\frac{P(t)}{P(0)} = e^{-\left(\frac{32\pi^2 Dt}{\lambda^2}\right)} e^{-\left(\frac{8\pi^2 r_0^2}{\lambda^2}\right)}, \tag{14}$$

where the term $e^{-\left(\frac{8\pi^2 r_0^2}{\lambda^2}\right)}$ represents the attenuation to the echo signal due to the initial true radius of the meteor trail and the term $e^{-\left(\frac{32\pi^2 Dt}{\lambda^2}\right)}$ represents the decay in the echo power as a function of time due to diffusion. The decay time constant, τ, is then

$$\tau = \frac{\lambda^2}{32\pi^2 D}. \tag{15}$$

The decay in echo power due to electron diffusion is the biggest contributor to the decay in echo power. Electron-ion recombination does affect the echo power, but its effects are negligible relative to the effects of diffusion and are not presented [McKinley].

Reproduced with permission of the copyright owner. Further reproduction prohibited without permission.

From equations 13 and 14, it can be seen that the return power from an underdense meteor trial decays exponentially with time. The two parameters in equation 14 that determine the decay time are wavelength and the ionic diffusion coefficient. The wavelength is a system parameter and can be known for any radar system. If the echo power from an underdense meteor trial is measured and the decay time calculated, then the ionic diffusion coefficient can be determined. Other useful information can be derived from the calculated ionic diffusion coefficient.

Diffusion Coefficient

The diffusion coefficient, D, of a single species of particle is presented by Chen [1984] as

$$D = \frac{KT}{mv}, \tag{16}$$

where K is Boltzmann's constant, T is the temperature of the species, m is the molecular mass of the species, and v is the collision frequency of the species. Jones [1995] shows that by applying kinetic theory to the diffusion coefficient, the dependence

$$D \propto \frac{T^{1/2}}{\rho}, \tag{17}$$

where ρ is the number density of atmospheric molecules, can be derived. From equations 16 and 17, it follows that if the species is known, and the diffusion coefficient is known, then the temperature-density relation can be calculated. It is then conceivable that the data from a radar measuring the decay times of meteor echoes could be used to provide temperature profiles in the meteor region if the density is known. Alternatively, if the temperature is known, such radar data could be used to calculate the density. Deriving useful information from the measured diffusion coefficient of a diffusing meteor trail, however, is not very straight forward. The diffusion coefficient presented in equation 16 is for a single species of particle.

Reproduced with permission of the copyright owner. Further reproduction prohibited without permission.

In meteor plasma trails, there are free ions, free electrons, and neutral particles. At the altitudes of the meteor region (between roughly 70 and 130 km), there are also many different species of neutral particles, which correspondingly means there are many different species of ions within a meteor trail. When a meteoroid leaves a wake of plasma deposited in a neutral atmosphere (the meteor trail), this plasma trail diffuses radially. The previous section presented the derivation of a radar echo from such a radially diffusing meteor trail. If the meteor trial is assumed to contain free electrons, free ions and neutral particles, then from equation 16, it is clear that the small mass of the electrons would dictate that they diffuse more quickly than the ions and neutral particles. The separation between the electrons and ions due to more quickly diffusing electrons, however, would set up an electric field that would act to slow the diffusive motion of the electrons and increase the diffusive motion of the ions. The net result is that the ions and electrons diffuse together. This is called ambipolar diffusion, and is the diffusive process present in a meteor trail. Chen [1984] provides a detailed derivation of the ambipolar diffusion coefficient, D_a, for the plasma in these conditions;

$$D_a = \frac{\mu_i D_e + \mu_e D_i}{\mu_i + \mu_e}. \tag{18}$$

where μ_e is the mobility of the electrons, μ_i is the mobility of the ions, D_e is the diffusion coefficient (from equation 16) of the electrons, and D_i is the diffusion coefficient of the ions. The mobility, μ, of a species is defined as

$$\mu \equiv \frac{|q|}{mv} \tag{19}$$

where q is the charge of the particle, m is the mass, and v is the particle velocity. So, given a measured echo decay time constant, the ambipolar diffusion coefficient can be calculated, and, if something is know about the species in the atmosphere, useful information such as temperature can still be derived. Again, however, the environment of meteor trails makes things a little more complicated. Charged particles behave differently in the presence of magnetic fields than they do in the absence of magnetic

Reproduced with permission of the copyright owner. Further reproduction prohibited without permission.

fields. Since meteor trails exist in the presence of the magnetic field of the earth, the ambipolar diffusion coefficient is not entirely applicable.

A magnetic field does not hinder the motion of particles parallel to that magnetic field. It is only when there is a component of motion perpendicular to the magnetic field that the magnetic field acts to retard motion. Chen [1984] again provides a detailed derivation of the cross magnetic field diffusion coefficient, $D_{\perp}$, of a single species;

$$D_{\perp} = \frac{D}{1+\frac{\omega_c^{\,2}}{\nu^2}} . \qquad (20)$$

where ω_c is the particle cyclotron frequency, and ν is the particle collision frequency. From equation 20 it can be seen that the diffusion coefficient across a magnetic field becomes the same as the standard diffusion coefficient if the particle cyclotron frequency is significantly less than the particle collision frequency.

In the case of the partial plasma of a meteor trail, the electron-neutral collision frequency is significantly higher than the electron gyro frequency for the lower altitudes of the meteor region, and is significantly lower in the higher altitudes of the meteor region. Conversely, the ion-neutral collision frequency is significantly higher that the ion cyclotron frequency for most of the ion species in the meteor region. A sample ionosphere taken from the International Reference Ionosphere (IRI) model, and neutral densities taken from the Mass Spectrometer & Incoherent Scatter (MSIS) extended atmospheric model were used to generate the cyclotron and collision frequency profiles shown in Figure 3.

Reproduced with permission of the copyright owner. Further reproduction prohibited without permission.

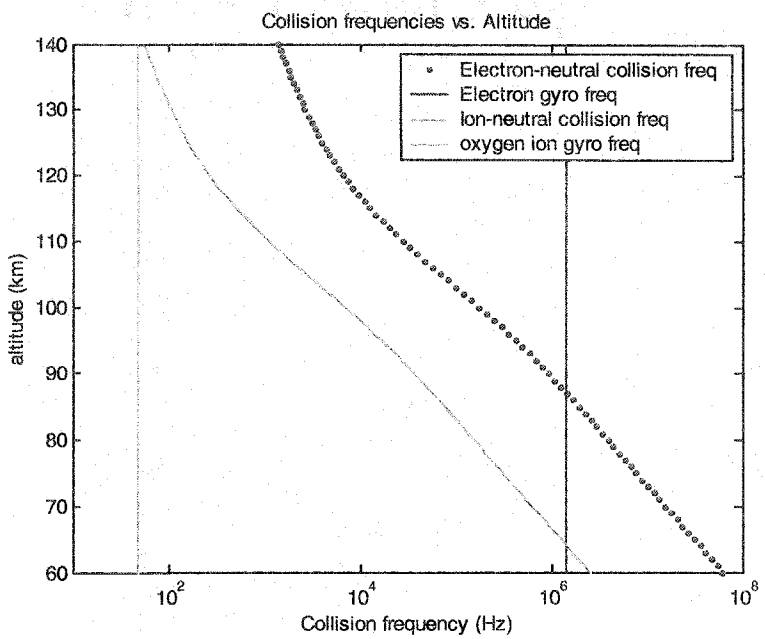

Figure 3: Electron and ion gyro frequency and neutral collision frequency profiles for the meteor region above Anchorage, AK

This figure shows that the ion-neutral collision frequency (for diatomic oxygen) is significantly greater than the ion gyro frequency for the meteor region. This means that for the cross magnetic field diffusion of the ions can be approximated by the standard diffusion coefficient. The electron-neutral collision frequency, however, is significantly lower than the electron cyclotron frequency for the upper reaches of the meteor region. This means that the cross field diffusion of the electrons is significantly different than the diffusion in the absence of the earth's magnetic field. When the ambipolar effects due to the attraction between the ions and electrons are taken into account, things get even more complicated. The ions, which are not bound by the magnetic field act to pull the electrons across the magnetic field. The net result is that through much of the meteor region, the effects of the magnetic field can be neglected, and the standard definition of ambipolar diffusion can be assumed. So, if the electromagnetic echo decay rate can be measured, some useful information, such as temperature-density relation, can be derived.

Reproduced with permission of the copyright owner. Further reproduction prohibited without permission.

HF Radar

A discussion of HF radar basics is important for the understanding of the new digital receiver system and the meteor scatter data processing algorithms it presented. HF radar is a broad topic and a thorough discussion would be extensive. The material presented here will provide the background necessary for the thesis project.

Radar (RAdio Detection And Ranging) refers simply to the active process of sending an electromagnetic wave, then detecting the reflections of that wave from a target for the purpose of gathering some sort of information about that target. Radar principles were developed in the early 1900's. There was a rapid increase in radar development and implementation in World War II in response to the military advantages of being able to detect and locate enemy aircraft [Peebles]. Since World War II, radars have been adapted to countless applications. While many radar systems can be complicated, the fundamental principles are simple.

Radar Fundamentals

The two simplest measurements that are made by a radar system are the range and line-of-sight velocity of a target. Assume there is some target at some distance, d, from the radar transmitter. Also assume, for simplicity, that the radar transmits and receives interrogating electromagnetic waves with the same antenna. Then the range to the target can be determined from the time, t, it takes for an electromagnetic wave to travel from the transmitting antenna to the target and back. This equation that defines this range is

$$d = \frac{ct}{2} \tag{21}$$

where c is the mean speed of light during its trip to the target and back. In free space c is roughly 3e8 meters per second. The line-of-sight velocity of a target can be determined by a change in the frequency of the RF signal reflected from the target. As a target

Reproduced with permission of the copyright owner. Further reproduction prohibited without permission.

moves with respect to the radar, the range at which the signal is reflected changes with time. This acts to compress or elongate the reflected signal, which changes the echo frequency. This is similar to the tone of a car horn changing as it passes a listener. This is known as Doppler shift. The equation for the line-of-sight velocity, v_{LOS}, of a target as related to the Doppler frequency as

$$v_{LOS} = -\frac{cf_D}{2f_0} \tag{22}$$

where f_D is the Doppler frequency, and f_0 it the frequency of the RF signal. So, if the time it takes the signal to travel to the target and back is known, the range to the target is known. Also, if the frequency of the return signal is known, then the line-of-sight velocity is known.

Pulsed Radar

There are two main types of radars, pulsed, and continuous wave. The radar type of interest in this discussion is a pulsed radar. In a pulsed radar system, the RF signal, at the frequency of operation, is essentially amplitude modulated with a rectangular function. The transmitted signal is then an RF signal that lasts for time finite time, and then repeats. The concept of a pulsed signal is illustrated in Figure 4.

Reproduced with permission of the copyright owner. Further reproduction prohibited without permission.

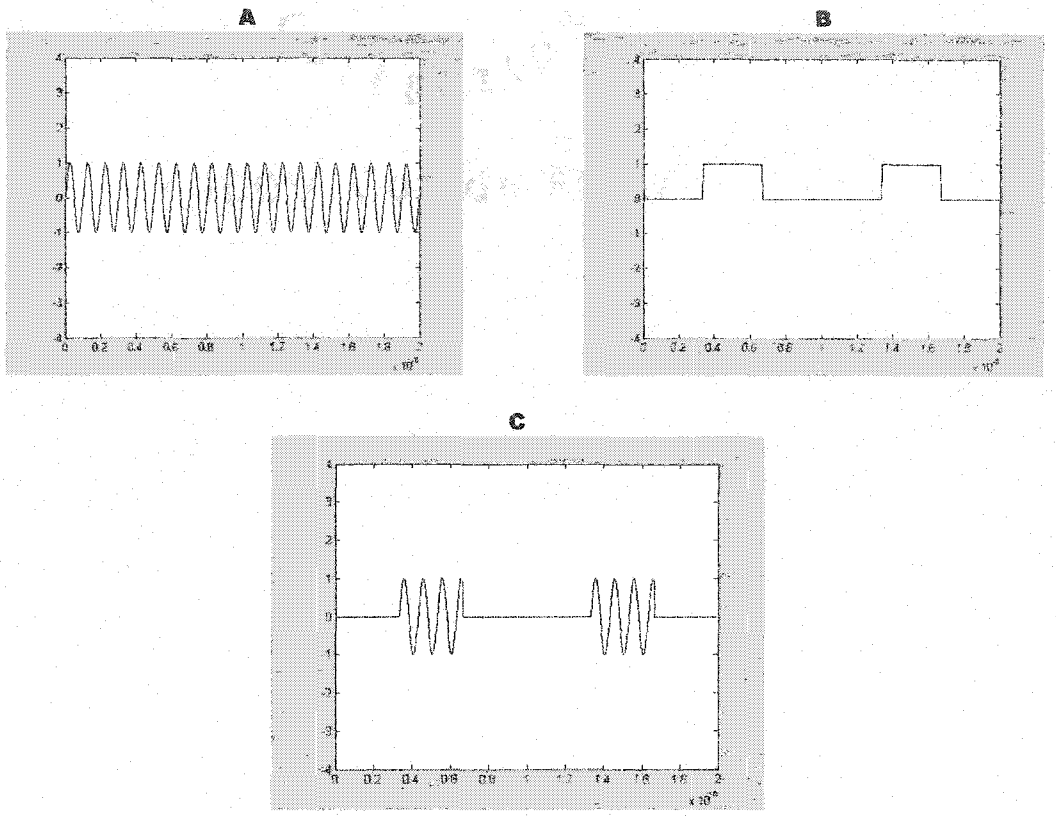

Figure 4: Coherent Pulsed Radar Signal Development

A) Continuous wave of frequency *f*.
B) Rectangular modulating signal. Pulse width is τ. Pulse separation is ψ
C) Total pulsed radar signal

Autocorrelation and Crosscorrelation

As has been mentioned previously, there are many different implementations of radar systems for the purpose of identifying characteristics of many different targets. If a target is stationary, much useful information can be derived from the autocorrelation of the signal reflected from that target. A stationary target is not defined as a target that is not moving, but rather as a target that has an echo signal with an autocorrelation function

Reproduced with permission of the copyright owner. Further reproduction prohibited without permission.

that depends only on the time difference between samples. Childers [1997] presents a development of the autocorrelation function for a stationary process. The complex auto correlation function for times t_1 and t_2 is

$$R_{XX^*}(t_1,t_2) = E[X(t_1)X^*(t_2)] \tag{23}$$

where E[] is the expected value. This can be written as a continuous function in terms of τ as

$$R_{XX^*}(\tau) = E[X(t)X^*(t+\tau)] \tag{24}$$

where $\tau = t_2 - t_1$ [Childers, 1997]. Since the expected value of a process is the infinite time average, equation 24 can be approximated as the time average,

$$R_{XX^*}(\tau) = \overline{X(t)X^*(t+\tau)}. \tag{25}$$

If $X(t)$ is taken as the complex function with a real part, $I(t)$, and an imaginary part, $Q(t)$, such that

$$X(t) = I(t) + Q(t), \tag{26}$$

then the complex autocorrelation can be written as

$$R_{XX^*}(\tau) = \overline{[I(t)+Q(t)]\cdot[I(t+\tau)-Q(t+\tau)]}. \tag{27}$$

I(t) is chosen as the real part and Q(t) is chosen as the imaginary part to relate the generation of the autocorrelation to the in-phase (I) and quadrature (Q) sampling capabilities of many radars. The autocorrelation function provided in equation 27 can then be broken into its real and imaginary parts such that

$$\mathrm{Re}(R_{XX^*}) = \overline{I(t)I(t+\tau)+Q(t)Q(t+\tau)} \tag{28}$$

and

$$\mathrm{Im}(R_{xx^*}) = \overline{Q(t)I(t+\tau)-I(t)Q(t+\tau)}. \tag{29}$$

When in-phase and quadrature sampling is employed, the in-phase and quadrature baseband samples are 90° out of phase with respect to each other, just as are the real and imaginary planes. When the in-phase samples of a radar echo signal are taken as I(t) and the quadrature samples are taken as Q(t), the complex autocorrelation of the echo signal is that of equation 27. Since a typical modern radar system uses baseband digital

Reproduced with permission of the copyright owner. Further reproduction prohibited without permission.

sampling techniques, the discrete I(t) and Q(t) samples can be used to calculate the discrete autocorrelation function of the echo signal.

Specialized techniques have been developed to determine the ACF of radar returns from targets that are extended in space. One technique that is designed for mitigating range aliasing problems, developed by Farley [1972], uses a specially designed sequence of unequally spaced pulses to generate a series of discrete time lags, τ. These sequences have the property that returns for only a single range will correlated for a given lag spacing. An example pulse sequence is provided in Figure 5.

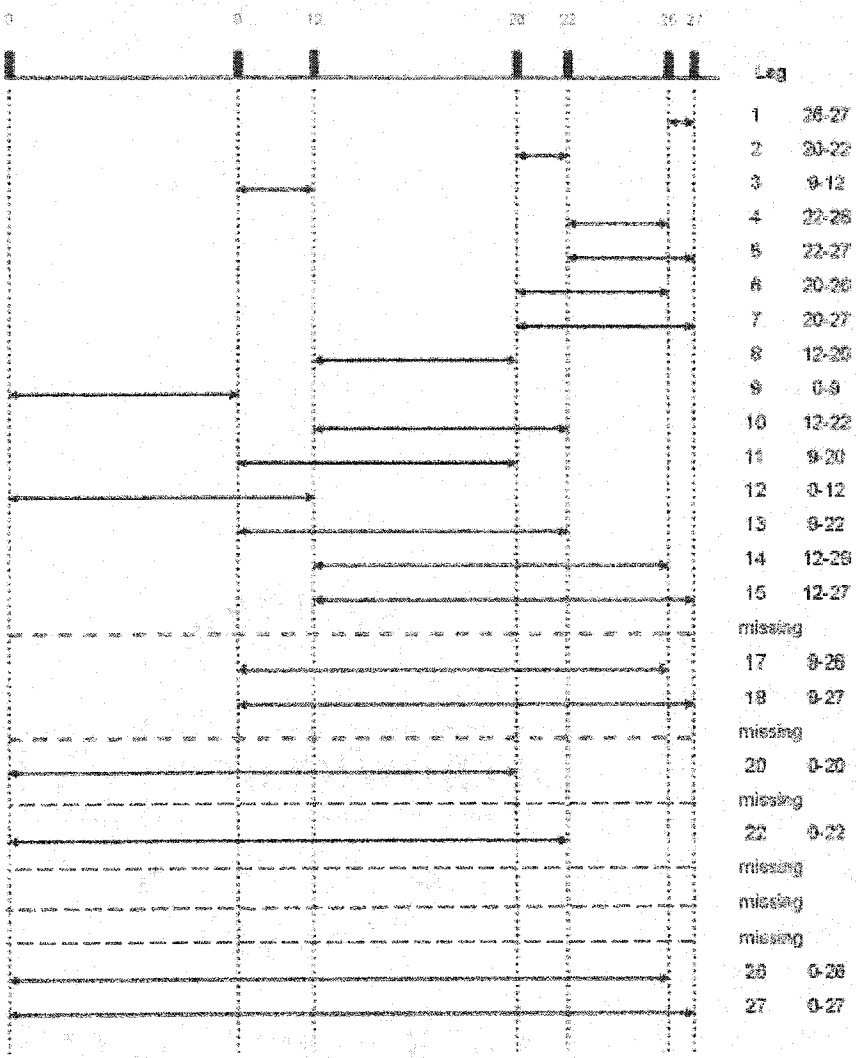

Figure 5: Example multipulse sequence and lag chart

[McWilliams, 2003]

Reproduced with permission of the copyright owner. Further reproduction prohibited without permission.

The figure shows an example pulse transmission sequence. This sequence, which has only seven pulses can be used to generate ACF lags to $\tau = 27$. In the pulse sequence implementation shown in Figure 5, a pulse is transmitted at 0, 9, 12, 20, 22, 26, and 27 times τ, where τ is some fundamental time separation. By taking the time difference between different pulses in the sequence a series of lags can be constructed. For example, for a lag of $\tau = 0$,

$$R_{XX^*}(0) = \overline{[I(t+0\tau)+Q(t+0\tau)]\cdot[I(t+0\tau)-Q(t+0\tau)]} \qquad (30)$$

where t corresponds to the time of the sample for a given range of interest. This should become more clear when a lag of $\tau = 1$ is considered. For a lag of $t = 1$, the pulses separated in time by τ should be considered. In the case of the pulse sequence shown in Figure 5, pulses at times 26τ and 27τ are separated by τ. Then the autocorrelation at $\tau = 1$ becomes

$$R_{XX^*}(1) = \overline{[I(t+26\tau)+Q(t+26\tau)]\cdot[I(t+27\tau)-Q(t+27\tau)]}. \quad (31)$$

To further illustrate the idea of generating the autocorrelation of the echo signal using this multipulse technique, consider one more lag of $\tau = 2$. The autocorrelation value at this lag is

$$R_{XX^*}(2) = \overline{[I(t+20\tau)+Q(t+20\tau)]\cdot[I(t+22\tau)-Q(t+22\tau)]}. \quad (32)$$

If all of the available lags, which are shown in Figure 5, are used, then a 22 point autocorrelation can be calculated. The 22 points come from the maximum lag of 27 minus the 6 missing lags. When all available lags are considered a discrete autocorrelation of the echo signal is created. The spacing between points is the fundamental pulse spacing, τ. If $\tau = t_2 - t_1 = 2.4$ ms, then the separation between points in the autocorrelation is 2.4 ms. Figure 6 shows a real autocorrelation of ionospheric echo data taken from a SuperDARN radar.

Reproduced with permission of the copyright owner. Further reproduction prohibited without permission.

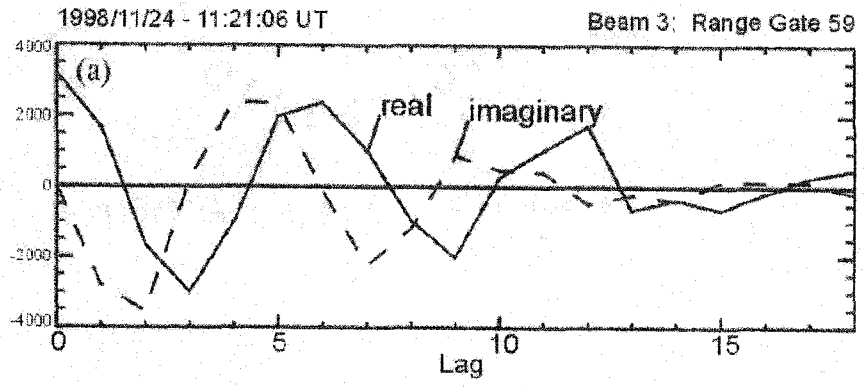

Figure 6: Example autocorrelation function of an ionospheric echo taken from a SuperDARN radar [McWilliams, 2003]

In this figure only the first 19 lags are shown. This is real ionospheric echo data taken from a SuperDARN radar in November of 1998. Figure 6 shows the autocorrelation as a real part and an imaginary part. These correspond to the real and imaginary parts given by equations 28 and 29 and are 90° out of phase as expected.

The application of the multi-pulse autocorrelation development is based in the property of autocorrelations that relates them to power spectra. The Fourier transform of an autocorrelation function is the power spectral density of the original signal. From the power spectral density, such parameters as spectral width, peak Doppler shift, and multi-peak Doppler shifts can be derived. In the case of most radars, obtaining information such as range, Doppler shift, and spectral width of given targets is the design goal of the radar.

Range Resolution and Range Accuracy

The accuracy to which a radar system can determine the range of a target is determined by the design of the radar system. Most radar systems mix the target echo with the local oscillator used to generate the original base-band signal. This base-band signal is then sampled with an analog-to-digital (A/D) converter. The resulting samples are then processed digitally to extract information about the target. This is the type of

Reproduced with permission of the copyright owner. Further reproduction prohibited without permission.

radar system discussed here. In an ideal situation, the range resolution of the radar would be directly related to the sampling frequency of the receiver. Assuming a hard targets, and a single radar pulse, the sampling period of the receiver would correspond to a fixed distance in space along the line of sight of the radar. Given a receiver sampling period, T_s, the range resolution, d, would be given by,

$$d = T_s\left(\frac{c}{2}\right), \tag{33}$$

where c is the velocity of the interrogating waveform. This resolution applies only to hard targets. For distributed targets, the resolution is directly related to the transmit pulse and the receiver filters. The development for range the resolution of a distributed target is not presented. As shown in equation 33, the ideal range resolution for hard targets is simply half of the distance that the interrogating wave can travel between two receiver samples. This simple concept of range resolution is illustrated in Figure 7.

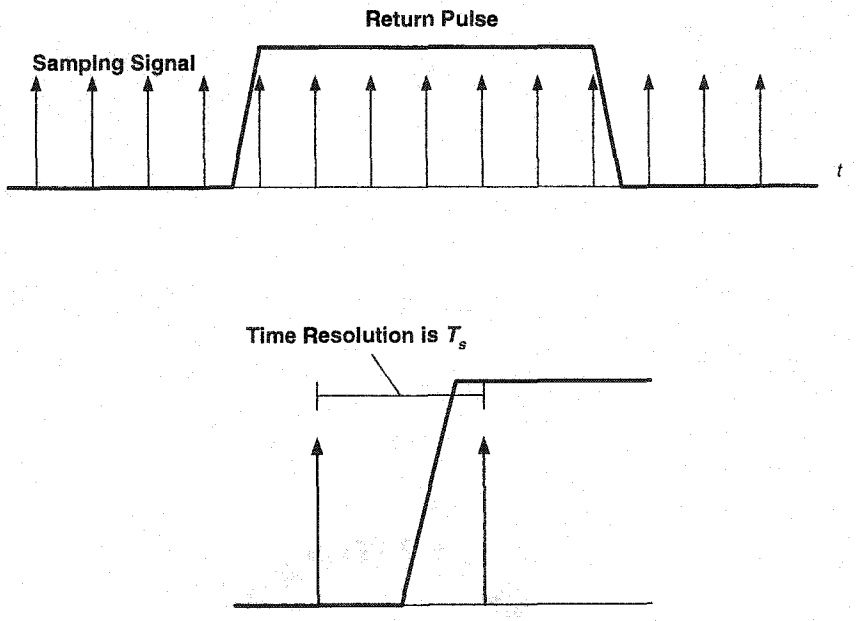

Figure 7: Ideal range resolution is determined by receiver sampling period

Reproduced with permission of the copyright owner. Further reproduction prohibited without permission.

Figure 7 illustrates that the leading edge of the return signal envelope may occur at any time between sampling pulses. This means that the time of return is not known precisely between those pulses. This time between sample pulses corresponds directly to a range resolution, d, as described by equation 33.

In a real radar system, however, the leading edge of the pulse envelope has some finite rise time, and the echo signal being processed contains noise. Levanon [1988] presents an analysis of delay estimation when noise is present. The analysis, assumes envelope detection of a pulsed radar return signal that has been passed through a band pass filter of bandwidth f_B, which defines the rise time of the pulse envelope. The pulse width is t_P and there is additive white noise with a two-sided power spectral density of $N_O/2$. Given this configuration, the rise time of the filtered pulse is $t_R = 1/f_B$. When the RMS noise power is considered, the noise can modeled as a near DC power. Near to the threshold crossing, the relationship

$$\frac{n(t)}{\Delta t} \approx \frac{A}{t_R} \approx A \cdot f_B \tag{34}$$

where A is the envelope amplitude, can be assumed. This is conceptually illustrated in Figure 8.

Reproduced with permission of the copyright owner. Further reproduction prohibited without permission.

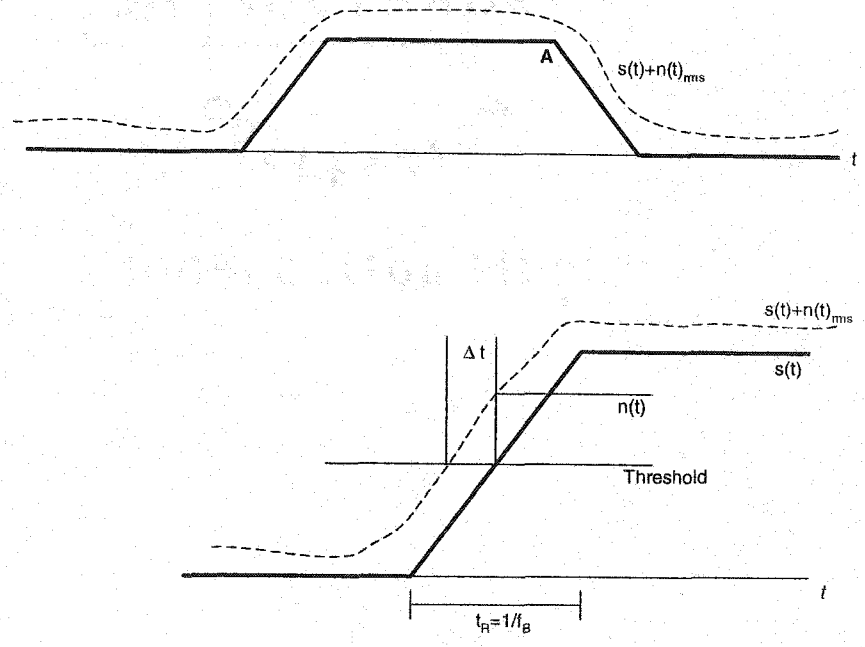

Figure 8: Return pulse after filter with additive noise

Based on the RMS noise, the RMS delay error is then given by

$$\sigma_{\tau 1} = \left[\overline{(\Delta t)^2}\right]^{\frac{1}{2}}. \tag{35}$$

Applying equation 34 to equation 35 yields the relation,

$$\sigma_{\tau 1} \approx \frac{\left[\overline{n^2(t)}\right]^{1/2}}{A \cdot f_B}. \tag{36}$$

Since the mean square noise is $N_O \cdot f_B$, equation 36 can be re-written as

$$\sigma_{\tau 1} \approx \left(\frac{N_O}{A^2 \cdot f_B}\right)^{1/2}. \tag{37}$$

Also, since the energy of the return pulse is $E = \frac{1}{2}A^2 t_P$, equation 37 becomes

$$\sigma_{\tau 1} \approx \left(\frac{t_P}{2 f_B E / N_O}\right)^{1/2}. \tag{38}$$

This error can be further reduced by a factor of $1/\sqrt{2}$ if both the leading edge and trailing edge of the pulse are considered [Levanon, 1988]. Considering the ratio of signal power, S, to the noise power, N, equation 38 becomes

Reproduced with permission of the copyright owner. Further reproduction prohibited without permission.

$$\sigma_{\tau 1} \approx \left(\frac{1}{4 f_B{}^2 S/N} \right)^{1/2} \tag{39}$$

for edge detection of both the leading and trailing edges. This time delay error can be directly converted into a range error using the relation $\sigma_R = \sigma_{\tau 1} \cdot c$. It should also be noted that the bandwidth term, f_B, in equation 38 is not necessarily related to the bandwidth of the receiver. In real radar systems, there is always a bandwidth limitation on the transmitted pulse. If the bandwidth of the transmitter is less than the bandwidth of the receiver, then the transmitter bandwidth should be substituted for f_B in equation 38.

Angle of arrival

Many radar systems use a technique called interferometry for determining the location from which an echo is returned. A simple radar system provides range information about a target. If this range information could be combined with information about the angles from which the echo is received, the location of the target can be known. Interferometry provides this angle information. For ease of discussion, a derivation of one dimensional interferometry is presented.

Consider a radar with two receiving antennas, separated by a distance, d, as shown in Figure 9.

Reproduced with permission of the copyright owner. Further reproduction prohibited without permission.

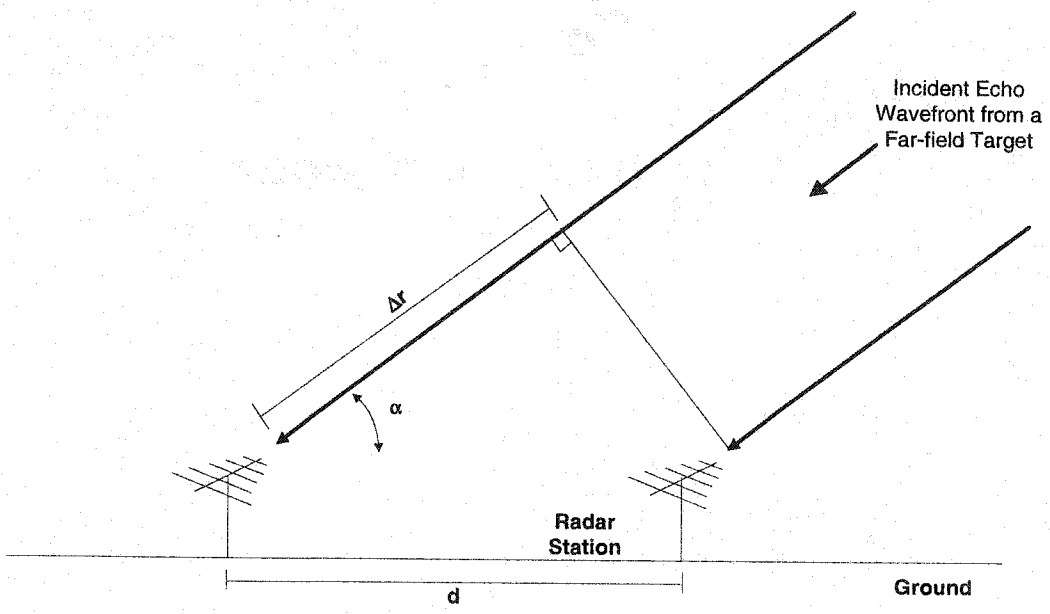

Figure 9: Interferometry geometry

The angle of arrival (AOA), α, can be calculated as

$$\alpha = \cos^{-1}\left(\frac{\Delta r}{d}\right). \tag{40}$$

So, if the difference in range, Δr, can be determined, then the angle of arrival can be calculated. There are two popular methods for measuring Δr. In the first method, the time delay, Δt, between the signals received at the two antennas is measured and Δr is calculated with the relation

$$\Delta r = c\Delta t\,. \tag{41}$$

The second method measures the phase difference, $\Delta\phi$, of the signal at the two antennas. Δr is then calculated with the relation

$$\Delta r = \frac{\Delta\phi}{2\pi}\lambda\,, \tag{42}$$

where λ is the wavelength of the reflected electromagnetic wave. In a real radar system, the total phase difference between the radars is not always measurable. Many radar systems that use interferometry only measure the modulo 2π phase difference between

Reproduced with permission of the copyright owner. Further reproduction prohibited without permission.

the antennas. This is not a problem if the antenna spacing, d, is less than $\lambda/2$, but such is not the case for many radar systems. If the antenna spacing is greater than $\lambda/2$, then the calculation for Δr becomes

$$\Delta r = \frac{\Delta\phi}{2\pi}\lambda + n\lambda \tag{43}$$

where $n = 0,1, 2, 3, \ldots$, such that

$$\frac{\Delta\phi}{2\pi}\lambda + n\lambda < d \ .$$

Often, there can be several values of n that satisfy this equation. If there is more than one value of n, then the AOA cannot be determined with certainty. There are many methods employed to limit the possible values of α and thus overcome the uncertainty, but these methods are beyond the scope of this discussion.

Reproduced with permission of the copyright owner. Further reproduction prohibited without permission.

Chapter 3: HF Radar at Kodiak

SuperDARN Overview

In the early 1980's a group of scientists and engineers at Johns Hopkins University designed and implemented an HF ionospheric radar at Goose Bay, Canada. This radar was the first radar in a network of radars that has now grown into SuperDARN. SuperDARN (Dual Auroral Radar Network) is a network of similarly designed radars, operating under the control of various scientific and education institutions, with the common goal of global ionospheric studies. Currently, there are fifteen radars, located near the magnetic poles, monitoring the convection of field-aligned irregularities in the ionosphere. The locations of these radars and their fields-of-view are illustrated in Figure 10.

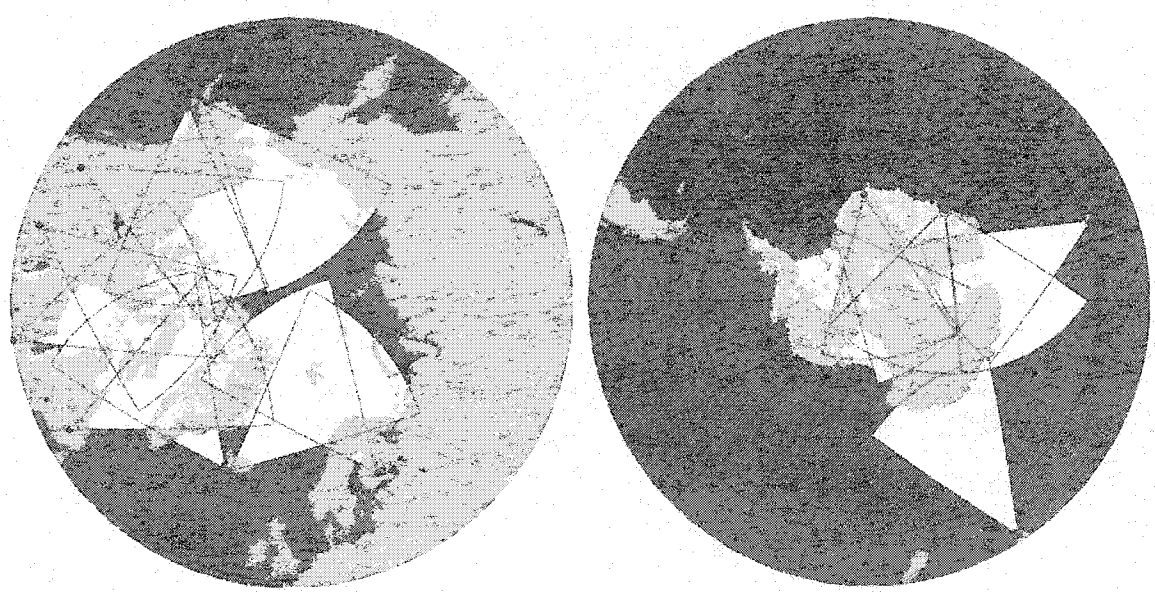

Figure 10: Locations and fields-of-view for both the northern hemisphere SuperDARN radars and the southern hemisphere SuperDARN radars

Reproduced with permission of the copyright owner. Further reproduction prohibited without permission.

The fifteen radars in the SuperDARN network are operated by ten different institutions. The Applied Physics laboratory at Johns Hopkins University, where the SuperDARN network was first conceived, operates radars at Kapuskasing, Ontario, and Goose Bay, Newfoundland. The University of Saskatchewan operates a radar at Prince George, British Columbia, and one at Saskatoon, Saskatchewan. The University of Leicester operates a radar a Pykkvibaer, Iceland, and a radar at Hankasalmi, Finland. Communications Research Laboratory, in Japan, operates a radar in King Salmon, Alaska, and the Geophysical Institute at the University of Alaska operates the radar at Kodiak, Alaska. The Centre National de la Recherche Scientifique (CNRS) in France operates the radars at Stokkseyri, Iceland, and Kerguelen Island. The National Institute of Polar Research in Japan has two radars at Syowa Station, Antarctica. LaTrobe University operates a radar in Tasmania, and the University of Natal, in South Africa, operates a radar at Sanae Station in Antarctica. Finally, the British Antarctic Survey operates a radar at Halley Station, Antarctica. Table 1 summarizes the locations and controlling institutions of all the radars in the SuperDARN network.

Reproduced with permission of the copyright owner. Further reproduction prohibited without permission.

Table 1: Geographic and Geomagnetic Locations of the radars in the SuperDARN network

Location	Institution	Geographic Latitude	Geographic Longitude	Geomagnetic Latitude	Geomagnetic Longitude
Halley Station, Antarctica	British Antarctic Survey	75.52 S	26.63 W	61.68 S	28.92 W
Sanae, Antarctica	University of Natal	71.68 S	2.85 W	61.52 S	43.18 E
Syowa, Antarctica	National Institute of Polar Research	69.00 S	39.58 W	55.25 S	23.00 E
Syowa, Antarctica	National Institute of Polar Research	69.01 S	39.61 W	55.25 S	22.98 E
Kergulen Island	CNRS	49.35 S	70.26 E	58.73 S	122.14 E
Tasmania	LaTrobe Univeristy	43.38 S	147.23 E	55.31 S	133.36 W
King Salmon, Alaska	Communications Research Lab.	58.68 N	156.65 W	57.43 N	100.51 E
Kodiak Island, Alaska	University of Alaska Fairbanks	57.60 N	152.2 W	57.17 N	96.28 W
Prince George, British Columbia	University of Saskatchewan	53.98 N	122.59 W	59.88 N	65.67 W
Saskatoon, Saskatchewan	University of Saskatchewan	52.16 N	106.53 W	61.34 N	45.26 W
Kapuskasing, Ontario	Johns Hopkins Applied Physics Lab.	49.39 N	82.32 W	60.06 N	9.22 W
Goose Bay, Newfoundland	Johns Hopkins Applied Physics Lab.	53.32 N	60.46 W	61.94 N	23.02 E
Stokkseyri, Iceland	CNRS	63.86 N	22.02 W	65.04 N	67.33 E
Pykkvybaer, Iceland	University of Leicester	63.86 N	19.20 W	64.59 N	69.65 E
Hankasalmi, Finland	University of Leicester	62.32 N	26.61 E	59.78 N	105.53 E

There are currently plans to implement several more radars in the SuperDARN network and to expand the network equatorward to get better coverage for observing global scale convection during magnetically active intervals.

The SuperDARN network was implemented with the design goal of generating ionospheric convection maps near the polar regions. To this end, the network is designed such that field-of-view of each radar overlaps with the field-of-view of at least one other.

Reproduced with permission of the copyright owner. Further reproduction prohibited without permission.

As the field-aligned irregularities drift with the surrounding plasma due to $E \times B$ drifts (E is the electric field and B is the magnetic field), this provides a 'stereoscopic' view which allows two-dimensional $E \times B$ velocity vectors to be realized. Polar region ionospheric convection maps can be created by combining the velocity information obtained from all of the radars in the network. An example convection map is shown in Figure 11.

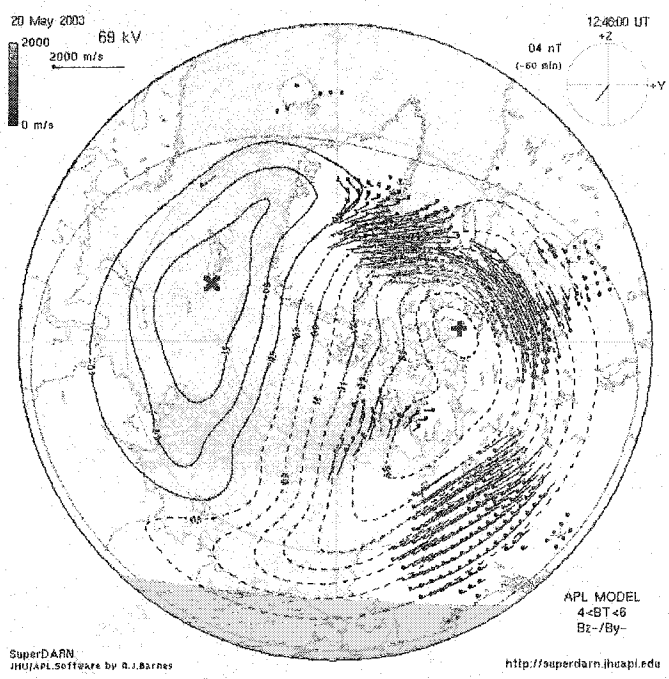

Figure 11: Example northern hemisphere convection map for May 20, 2003 at 12:48 UT

In this figure, the colored dots represent the location of the measured velocity data, the 'tails' on the dots indicate the direction of the velocity, and the length of the tails and the color represent the magnitude of the velocity. Since the magnetic field is known and the drift velocity is measured, the electric field can be derived. The contour lines represent the derived equipotentials of the electric field. While convection data such as that shown in Figure 11 is one of the main science missions for the SuperDARN network of radars, the data from these radars is used for an amazing variety of other research. Often, some or all of the radars are operated in special modes to support this research. A detailed

Reproduced with permission of the copyright owner. Further reproduction prohibited without permission.

overview of the operation and scientific goals of the SuperDARN network is provided by Greenwald et al. [1995].

Brief Overview of the HF Radar at Kodiak

The fifteen radars in the SuperDARN network are operated by ten different institutions around the world. The radar located on Kodiak Island is operated by the Geophysical Institute at the University of Alaska Fairbanks. While this radar is actually located near the town of Chiniak, Alaska, this radar is known throughout the SuperDARN community as the radar at Kodiak and will be referred to as such within this thesis.

The HF radar at Kodiak is fairly simple in design. It consists of 16-log periodic antennas in the main array, 4 antennas in the interferometry array, sixteen 600 W transmitters, two synthesizers, a receiver, phasing electronics, and two control and processing computers.

The main antenna array is a linear array consisting of 16 log-periodic antennas separated by 15.24 meters. Time delay phasing is implemented to steer the main beam of this array over ± 26 degrees off perpendicular in 16 discrete increments. The typical field of view of the radar, along with some typical data, is shown in Figure 12.

Reproduced with permission of the copyright owner. Further reproduction prohibited without permission.

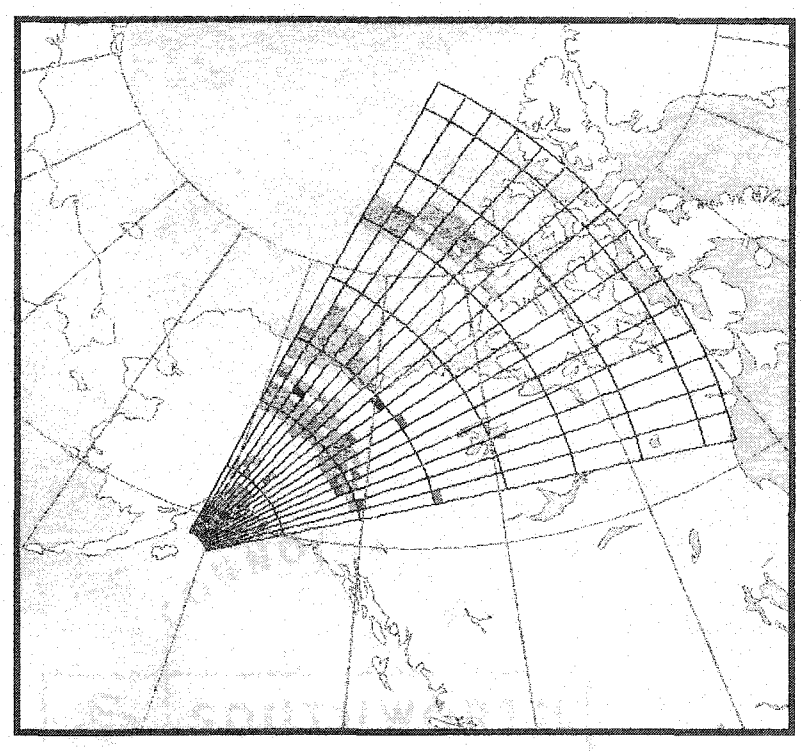

Figure 12: Typical field of view for the HF radar at Kodiak Island

The figure shows data from a typical operating mode. Data is typically collected for ranges from 180 km to 3555 km distance from the radar. Since the radar operates in the HF band, refraction plays an important role in the operation of the radar. Typically, the scattering targets of the radar are small-scale field-aligned density irregularities the E-region and F-region. Irregularities with a scattering cross-section large enough to be detected are not expected much higher in altitude than the attitude corresponding to the peak of F-region electron density. While this altitude varies greatly with ionospheric conditions, a practical altitude limit for the typical radar echoes is very roughly set at 450 km. In Figure 12, each line in range represents ten 45 km range gates, or 450 km, starting at the first range of 180 km. Each line in azimuth bounds one of the 16 discrete beam directions.

One-hundred meters behind the main array is a second array of four antennas. The main array and the secondary array form a one-dimensional interferometer. Since the secondary array forms an interferometer with the main array, it will hereinafter be

Reproduced with permission of the copyright owner. Further reproduction prohibited without permission.

referred to as the interferometry array. Time delay phasing is also used in the interferometry array to steer the beam. The beams of both arrays are synchronized so that the main beams of both arrays are always pointing in the same direction. Sitting between the arrays is a small shelter that contains the control and data processing hardware. Two computers control the system. One is used solely to control the precise timing signals for the radar functions. The other is used to host the radar control programs, to sample the baseband signal, and to do all of the data processing, collection, and storage. The shelter also contains the phasing matrix, the signal generators, the mixers, and the receiver. A photograph of the radar site at Kodiak Island is provided in Figure 13.

Figure 13: Photograph of the HF radar site at Kodiak Island

The photograph shows the sixteen log-periodic antennas that constitute the main array of the radar, the four antennas of the interferometry array, and the shelter housing most of the radar hardware.

The SuperDARN HF radar at Kodiak is very similar in design to most of the other radars in the network. While a detailed discussion of the design and implementation of

Reproduced with permission of the copyright owner. Further reproduction prohibited without permission.

this radar system is beyond the scope of this thesis, a brief discussion will be presented. Greenwald et al. [1985 and 1995] provides a fairly detailed overview of the system.

Important Details of the HF Radar at Kodiak

Frequency of Operation

All of the radars in the SuperDARN network, including the radar at Kodiak, are designed to scatter from field-aligned irregularities drifting with the plasma of the ionosphere. Scatter from the irregularities is specular, so to receive the scatter, the incident wave must be nearly orthogonal to the magnetic field lines along which the irregularities form. At high latitudes, refraction of the incident radar signal is required to achieve orthogonality. Refraction of electromagnetic waves requires that the frequency be close to the ionospheric plasma frequency. The radars in the SuperDARN network have a wide frequency band over which they can operate to maximize the scatter from the field-aligned irregularities during a wide variety of ionospheric conditions. Each of the radars is designed to operate from 8 to 20 MHz. Since the propagation conditions in the ionosphere are highly variable, and propagation path of an electromagnetic wave within the ionosphere is a function of the frequency of that wave, this wide operating band maximizes the likelihood that some field-aligned irregularities are observable.

Within the radar hardware bandwidth capabilities of 8-20 MHz, not all frequencies can be used. Since the HF radar at Kodiak is within the United States, it falls under the regulation of the Federal Communication Commission (FCC). The FCC license for the radar governs the frequencies at which the radar can transmit. The license permits operation on 15 bands within the operating range of the radar. These frequency bands are provided in Table 2.

Reproduced with permission of the copyright owner. Further reproduction prohibited without permission.

Table 2: FCC frequency allocations for operation of the HF radar at Kodiak

Band	Start Freq (kHz)	Stop Freq (kHz)	Width (kHz)
1	8000	8100	100
2	9040	9500	460
3	9900	9995	95
4	10150	11175	1025
5	11400	11650	250
6	12050	12230	180
7	13410	13600	190
8	13800	14000	200
9	14350	14970	620
10	15600	16360	760
11	17410	17550	140
12	18030	18068	38
13	18168	18780	612
14	18900	19680	780
15	19800	19990	190

The FCC license also dictates the bandwidth of the transmitted signal. The current license limits the signal bandwidth to 22 kHz. The bandwidth puts limits on the operating potential of the radar. This puts practical limits on the pulse width and modulation bandwidth, which limits the achievable range resolution of the radar.

Clear Frequency Search

The bands of operation allocated by the FCC for the HF radar at Kodiak are used all over the world by various governments, institutions, corporations, and citizens for HF communications and instrumentation. This means that the radar is sharing frequency space with many other transmitters worldwide. The ionospheric refraction properties that make the radar an effective ionospheric research tool also allow HF signals to propagate great distances. This means that much of the HF band, including the frequency allocations of the radar, are desirable for long range communication. This also means that the signals from transmitters located very far from Kodiak Island can interfere with the operation of the radar. For these reasons, the radar must search for frequencies within its operating bands that are not cluttered with interference from distant or not too distant

Reproduced with permission of the copyright owner. Further reproduction prohibited without permission.

transmitters. To accomplish this, in normal operating modes, the radar performs a clear frequency search.

A clear frequency search is simply an algorithm in the radar operating software that searches over a band near the desired operating frequency to find a frequency that is not in use. The frequency with the lowest received power, or noise, is chosen as the frequency of operation. Depending on the operating mode, a new frequency is typically chosen every 3 to 6 seconds.

Antennas

The antennas used at the Kodiak HF radar are Model 608 log-periodic antennas manufactured by Sabre Communications Corporation out of Sioux City, Iowa. These antennas are specified for use over the band of 8 to 20 MHz. Sabre specifies a forward gain of at least 12 dBi for 8 to 15 MHz, and of at least 14 dBi for 15 to 20 MHz. The front-to-back ratio is specified at 14 dB averaged over the band. The voltage-standing-wave-ratio (VSWR) is specified at less than 2.0 over the band.

A numerical electromagnetic code (NEC) model of the antenna yields a pattern consistent with the specifications of the antenna. Modeling the radiating structure in a NEC software package called EZNEC yields the azimuthal radiation pattern shown in Figure 14.

Reproduced with permission of the copyright owner. Further reproduction prohibited without permission.

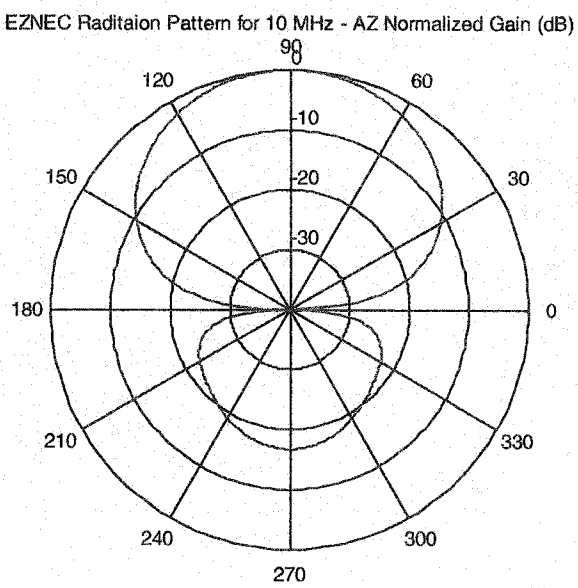

Figure 14: Normalized azimuthal radiation pattern of a single antenna at the Kodiak HF radar at 10 MHz

The plot of the azimuthal radiation pattern is normalized and the angles are referenced to the line of the array. Ninety degrees is the forward-looking direction. The gain of the antenna at the shown frequency of 10 MHz is 13.4 dBi. The front to back ratio is 16.8 dB. Similarly, the elevation radiation pattern for the log-periodic antenna 50 ft above a ground plane is shown in Figure 15.

Reproduced with permission of the copyright owner. Further reproduction prohibited without permission.

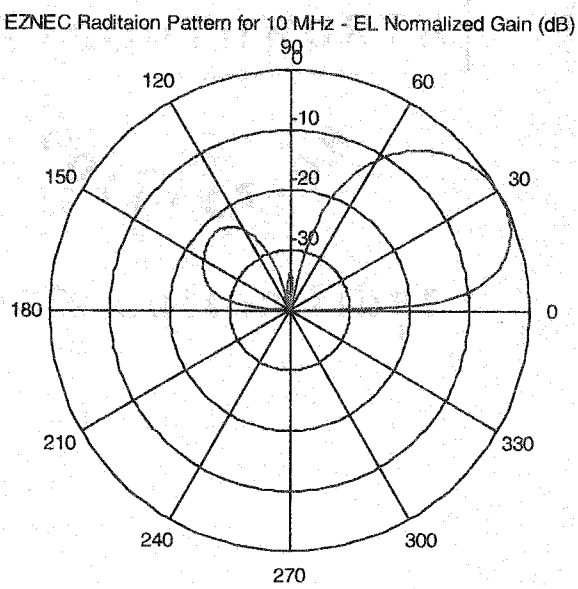

Figure 15: Normalized elevation radiation pattern of the main array at 10 MHz with a ground plane

Here, the peak of the main lobe is at 27° above the horizon, with a 3 dB beam width of 30.7°. The geometry, with this main lobe peak angle, is ideal for probing the upper atmosphere. As per the manufacturer specifications, this antenna should have very good radiating properties for the application of the HF radar at Kodiak. It should be noted, however, that these radiation patterns have not been experimentally verified at the radar site.

The HF radar at Kodiak implements the Sabre Communications Corp. Model 608 log-periodic antennas in two linear arrays. One of the arrays, the main array, consists of 16 antennas. This array is used for both transmission and reception. The seconds array, the interferometry array, consists of 4 antennas and is used only for reception.

The antennas in both arrays are positioned atop 50 ft towers, and are spaced 50 ft apart. A top view of the array geometry is provided in Figure 16.

Reproduced with permission of the copyright owner. Further reproduction prohibited without permission.

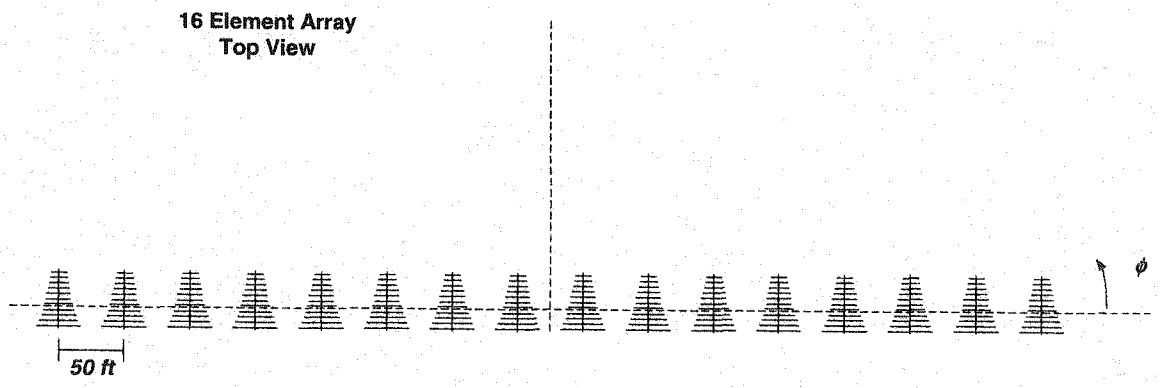

Figure 16: Top view of the main array geometry

The array acts to increase the radiative gain of the system and allows electronic steering of the radiative beam of the system. Using equations developed in Kraus [1992], the azimuthal pattern of the array can be determined for various feed phase delays. The equation describing the normalized azimuthal pattern of the array is given as,

$$E = \frac{1}{n}\frac{\sin(n\psi/2)}{\sin(\psi/2)}, \tag{44}$$

where n is the number of elements in the array (16 for SuperDARN main array) and ψ is the phasing, given by,

$$\psi = d_r \cos(\phi) - \delta . \tag{45}$$

In Equation 45, d_r is the element spacing in radians ($d_r = 2\pi d/\lambda$), where λ is the wavelength of the transmitted signal, and δ is the introduced phase delay.

Using the properties of arrays as described by Kraus [1992] the gain of the array can be calculated. The relation that the maximum possible electric field, E_{array}, from an array is equal to the number of elements, n, in the array times the electric field, E_0, due to one of the elements in the array. This is indicated by the equation

$$E_{array} = nE_0 \tag{46}$$

Reproduced with permission of the copyright owner. Further reproduction prohibited without permission.

[Kraus, 1992]. Since the radiated power, P_{array}, is directly proportional to the square of the electric field, equation 46 can be written in terms of power as

$$P_{array} = n^2 P_0 \tag{47}$$

where P_0 is the power radiated from a single antenna. This means the peak gain due to the array is $n^2 = 16^2 = 256$. This a gain of 24.1 dBi due to the array. Since each antenna is rated at a minimum of 12 dBi over the band of operation, the total gain, G_{total}, of the main antenna array is

$$G_{total} = 12 + 10\log(256) = 36.1 \text{ [dBi]}. \tag{48}$$

Taking equations 44 and 45, and setting the introduced phase delay between elements in the array, δ, to zero, the radiation pattern due to the array can be determined. The azimuthal radiation pattern due to the array is shown in Figure 17.

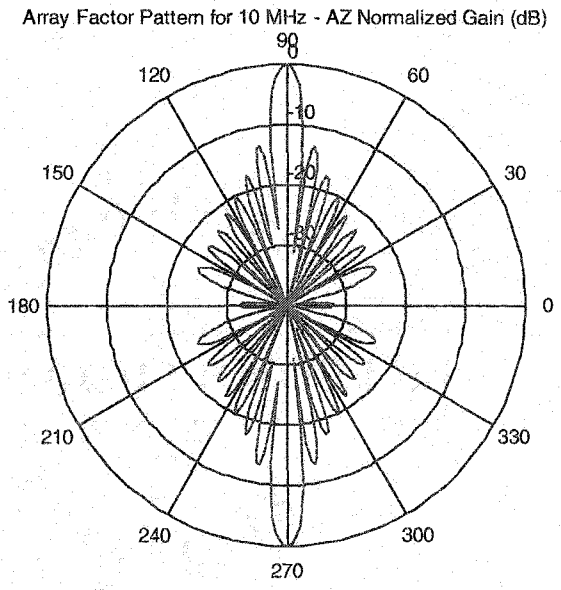

Figure 17: Normalized azimuthal array pattern for the main array at 10 MHz

The figure shows that there is a large backlobe and significant sidelobes in the array pattern. This backlobe, however, is drastically reduced when the 16.8 dB front to back ratio of the antenna is considered. This is evident when the total radiation pattern, which

Reproduced with permission of the copyright owner. Further reproduction prohibited without permission.

is the product of the antenna pattern and the array factor, is examined. The total azimuthal radiation pattern of the main array is shown in Figure 18.

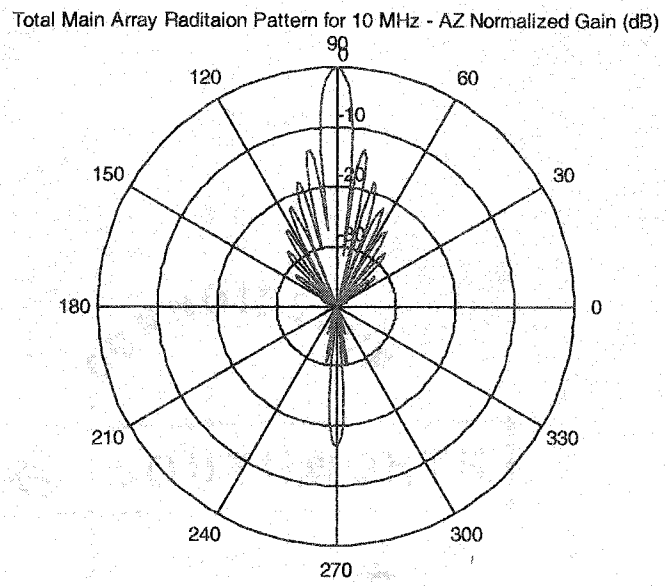

Figure 18: Normalized azimuthal total radiation pattern for the main array at 10 MHz

Since the array is linear, the elevation radiation pattern of the main array is simply the elevation pattern of a single antenna, as shown in Figure 15. When a phase delay, δ, is added between the elements of the array, the main beam can be steered in azimuth. This is clear when a phase shift of 79 degrees is introduced as illustrated in Figure 19.

Reproduced with permission of the copyright owner. Further reproduction prohibited without permission.

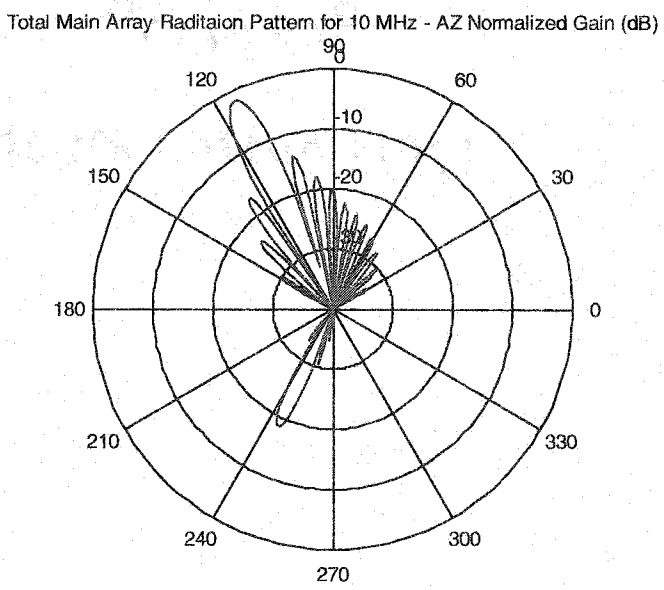

Figure 19: Azimuth pattern for the main array at 10 MHz with 79° phase shift introduced between the elements of the array

Because the spacing of the antennas is greater than $\lambda/2$ for frequencies greater than 9.84 MHz, beam steering leads to the rise of significant sidelobes, called grating lobes, in the radiation pattern. This is evident in the array pattern for a 20 MHz transmit frequency at the same beam angle as that shown in Figure 19. The normalized radiation pattern for this configuration is shown in Figure 20.

Reproduced with permission of the copyright owner. Further reproduction prohibited without permission.

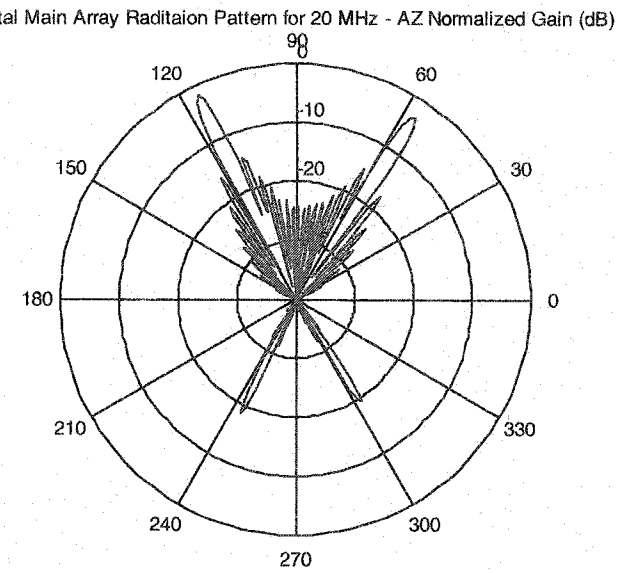

Figure 20: Azimuthal radiation pattern of the main array at 20 MHz at a main beam angle of 24° off perpendicular

The figure clearly shows that toward the 20 MHz upper limit of the radar operating band, large grating lobes can arise. If these side lobes are not considered, then the data from the radar can easily be misinterpreted.

Power

The HF radar at Kodiak has 16 transmitters associated with its 16 antennas. Each transmitter is rated for 600 W of transmitted power for a total transmit peak power of 9600 W. In typical operation, there are 70 pulses transmitted per second. Given the typical pulse width of 300 μs, the average transmitted power is 201.6 W. With a total gain of 36.1 dBi, the maximum effective radiated power, ERP, of the main array is

$$ERP = G_{total} + P_0 \tag{49}$$

where G_{total} is specified in dBi and P_0 is given in dBW. Taking G_{total} as 36.1 dBi, and P_0 as 600 W = 27.8 dBW, the effective radiated power is 63.9 dBW or 2.44 MW. So, for a

Reproduced with permission of the copyright owner. Further reproduction prohibited without permission.

average transmitted power of only 201.6 W, an effective radiated peak power of 2.44 MW is achieved.

Range Resolution

In typical operation, a pulse width of 300 μs is used, corresponding to a range resolution of 45 km for extended targets. There exist several special operating modes for the radar that operate with a 100 μs pulse width, corresponding to a range resolution of 15 km. While some of the radars in the SuperDARN network have a bank of several receiver filters that can be switched for matched filtering of several different pulse widths, the HF radar at Kodiak does not have such capability. The radar at Kodiak has only a single 10 kHz filter, which is matched to a pulse width of 100 ms. Also, since no frequency modulation or pulse coding is used, the maximum achievable distributed target range resolution for the radar is 15 km. For hard targets, an edge detection method can be used to increase the achievable range resolution of the system. Applying the typical filter bandwidth of 10 kHz to equation 39, the maximum achievable edge detection range resolutions are determined as a function of SNR. Table 3 shows the achievable range resolutions as a function of SNR.

Reproduced with permission of the copyright owner. Further reproduction prohibited without permission.

Table 3: Edge detection range error (resolution) as a function of SNR for the typical operating mode of the HF radar at Kodiak

SNR (dB)	Time error (s)	Range Error (m)
0	5.00E-05	15000
2	3.97E-05	11915
4	3.15E-05	9464
6	2.51E-05	7518
8	1.99E-05	5972
10	1.58E-05	4743
12	1.26E-05	3768
14	9.98E-06	2993
16	7.92E-06	2377
18	6.29E-06	1888
20	5.00E-06	1500
22	3.97E-06	1191
24	3.15E-06	946
26	2.51E-06	752
28	1.99E-06	597
30	1.58E-06	474
32	1.26E-06	377
34	9.98E-07	299
36	7.92E-07	238
38	6.29E-07	189

With the current hardware and operating code, the radar is capable of sampling the baseband signal at a minimum time resolution of 20 μs. This minimum sampling period sets the minimum achievable range resolution to 3 km. So, the sampling period of the existing radar hardware and the existing hardware receiver filter act to limit the minimum achievable range resolution to 3 km or less, depending on the SNR of the echo signal.

Pulsing

The HF radar at Kodiak transmits a multi-pulse sequence that is used to generate an autocorrelation function of the echo signal. The autocorrelation function is then used to derive information such as Doppler frequency, power, and spectral width. The sequence that is currently implemented in all of the radars in the SuperDARN network, including the HF radar at Kodiak, is shown in Figure 21.

Reproduced with permission of the copyright owner. Further reproduction prohibited without permission.

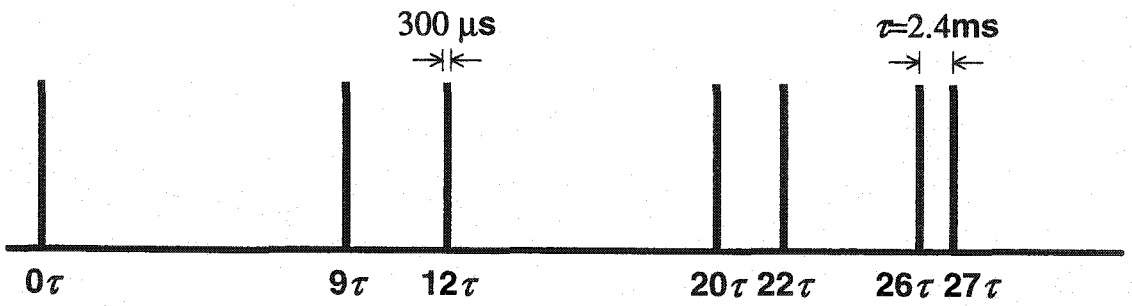

Figure 21: Pulse sequence currently used on all the HF radar at Kodiak

The fundamental pulse separation, τ, is 2.4 ms, and the pulse width is 300 μs. The pulse sequence contains seven pulses with one pulse transmitted at times of 0τ, 9τ, 12τ, 20τ, 22τ, 26τ, and 27τ. The lag table for this pulse sequence is provided in Figure 5. The total time required to transmit a pulse sequence is 65 ms. Allowing 35 ms for the last pulse of the sequence to travel to an adequately far range such that no more echo power should return permits a pulse sequence to be transmitted every 100 ms. This corresponds to the transmission of 70 pulses every second. There is currently a new pulse sequence being tested on the SuperDARN network that would have 8 pulses with a shorter fundamental separation time. The pulse sequence presented, however, is still used in typical operations.

Reproduced with permission of the copyright owner. Further reproduction prohibited without permission.

Chapter 4: Digital Receiver Design

Purpose

Initially, the goals of the thesis project presented here were very straight forward. They were to adapt the HF radar at Kodiak for increased range resolution detection of meteors and to derive wind profiles within the meteor region. This was to happen without adversely affecting the typical operations of the radar. When methods to accomplish this goal were examined, it was clear that the HF radar at Kodiak was not designed with this goal in mind, and that the radar receiver, with a fixed bandwidth and a limited sampling rate, was not adequate. It was determined that a completely new, digital receiver system would not only allow the goals of the project to be reached, but would also allow much more flexibility in the control and operation of the radar for other experimental purposes. The design and implementation of this new digital receiver is presented.

Receiver Card Overview

An 'off the shelf' digital receiver system was chosen to be incorporated into the HF radar at Kodiak. The receiver chosen was the Echotek Corporation digital receiver model GC214-PCI/TS, which shall be hereinafter referred to as the GC214. The GC214 is a commercially available receiver card designed for use as a receiver for the cellular communications industry. The GC214 is a short PCI card containing two high-speed analog-to-digital converters (ADCs), four numerically controlled oscillators (NCOs), four digital mixers, 12 finite impulse response (FIR) filters, data framing and control chips, and a PCI bus interface. These components work to provide two RF or IF (intermediate frequency) inputs, which can be sampled independently and processed through any or each of four narrowband receiver channels, two mid band channels, or a single broadband channel. A photograph of the GC214 is provided as a reference in Figure 22.

Reproduced with permission of the copyright owner. Further reproduction prohibited without permission.

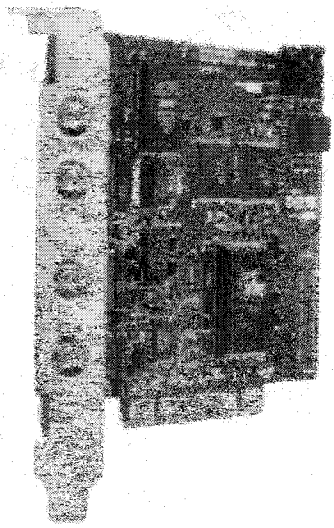

Figure 22: Photograph of the ECRD GC214-PCI/TS digital receiver card [Echotek, 2001]

This picture shows the two RF/IF inputs, a synchronization line, and a clock input. The two RF inputs are ideal for use at the HF radar at Kodiak. One input is used for the main array and one is used for the interferometry array. The synchronization line allows an external TTL signal to control the synchronization of functions on the card. The application of this synchronization line will be discussed in detail later. The clock input allows an external clock to provide all of the timing signals for the receiver. Also shown are the integrated circuits which constitute the ADCs, the NCOs, the filters, the framing and data control, and the PCI interface. A block diagram of the GC214 is provided in Figure 23.

Reproduced with permission of the copyright owner. Further reproduction prohibited without permission.

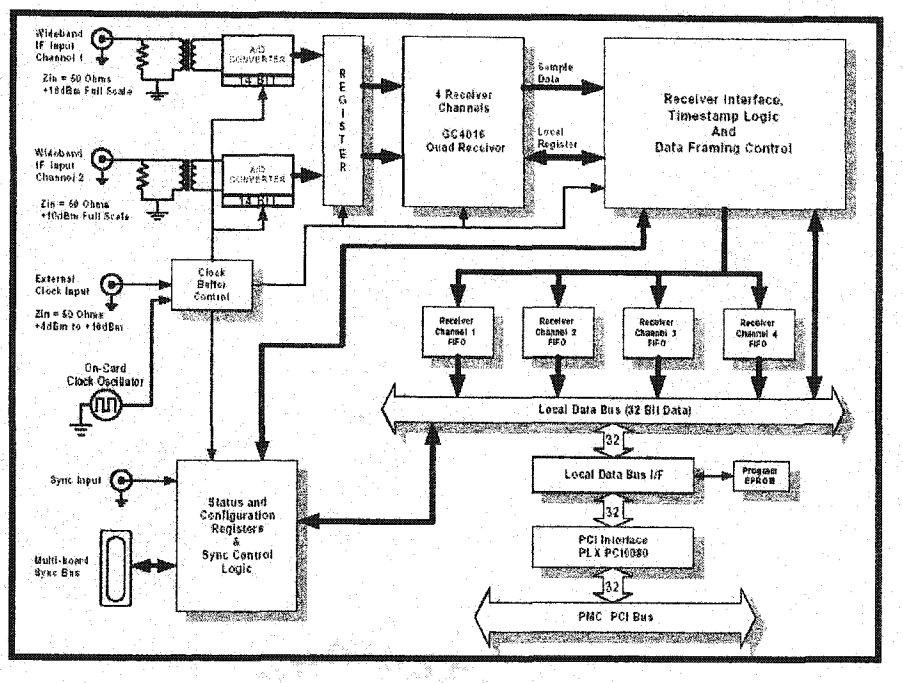

Figure 23: Block diagram of the ECDR GC214-PCI/TS

[Echotek, 2001]

Figure 23 shows the layout and operation of the GC214 in more detail. The two wideband RF/IF inputs are each transformer coupled to the inputs of a corresponding 14 bit ADC. The 3 dB bandwidth of the couplers is specified as 60 kHz to 250 MHz. Since the HF radar at Kodiak operates over 8-20 MHz, this bandwidth is more than adequate. The band pass properties of the transformers also prevent DC coupling to the ADCs, which alleviates the concern of DC coupling which is common in analog receiver design.

The ADCs used on the GC-214 are Analog Devices model AD6644AST-65 chips. These are 14 bit differential ADCs operated in common mode. These ADCs are capable of sampling rates up to 65 MHz. The manufacturer specified spurious-free dynamic range is 100 dB. Sampling jitter is less than 300 fs [Analog Devices, 2000]. The maximum scale input of these ADCs is 2 V_{p-p}, which corresponds to a 10 dBm signal at 50 Ω impedance. The outputs of the ADCs are passed to the digital receiver chip which does all of the receiver processing.

Reproduced with permission of the copyright owner. Further reproduction prohibited without permission.

The gut of the GC-214 digital receiver is the Grey Chip GC4016 quad receiver chip which is manufactured and sold by Texas Instruments. For reference, a block diagram of the GC4016 is provided in Figure 24.

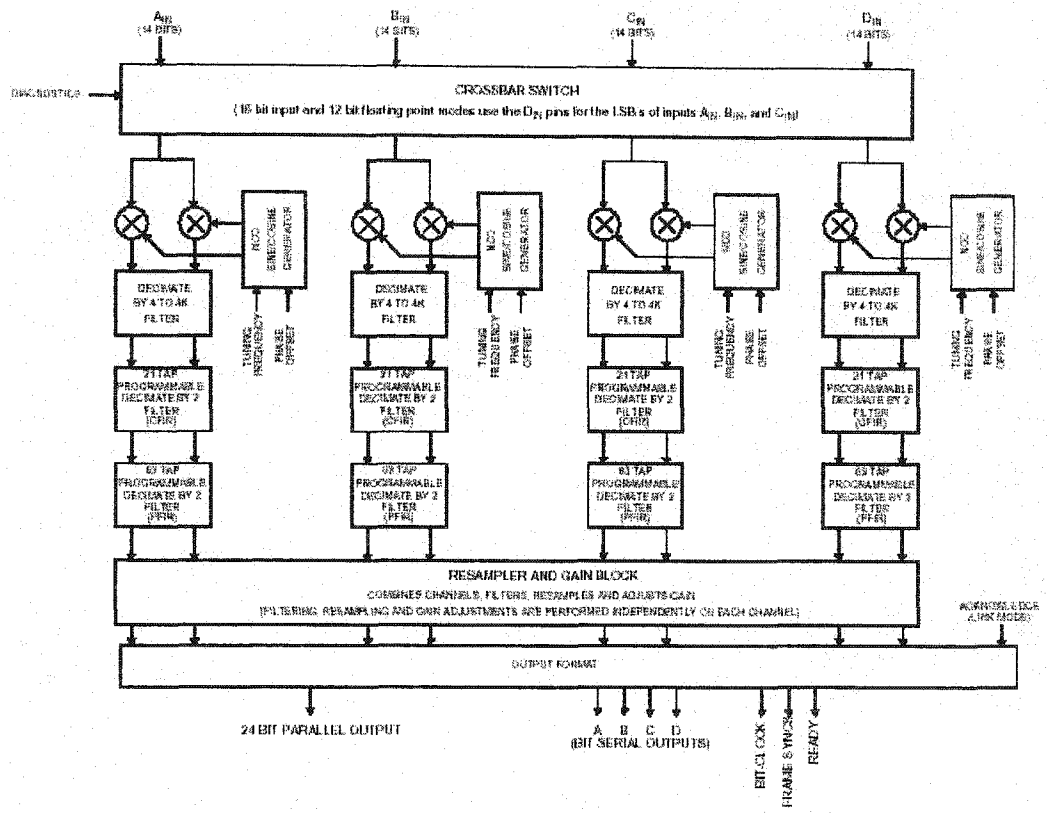

Figure 24: Block diagram of the GC4016 quad receiver chip
[Texas Instruments, 2001]

The GC4016 contains four receiver channels, which can be operated as four completely independent 'narrowband' receiver channels, as two mid band receiver channels, or as a single broadband receiver channel. When the GC4016 is operated as four independent receivers, the maximum bandwidth of each is 2.1875 MHz. If the GC4016 is operated as two mid band receivers, the maximum bandwidth of each is doubled to 4.375 MHz. If the GC4016 is operated as a single broadband receiver, the maximum bandwidth is doubled again to 8.75 MHz [Texas Instruments, 2001]. Figure 24 shows that there are four 14-bit inputs to the GC4106. On the GC214 receiver card, there are only two RF/IF

Reproduced with permission of the copyright owner. Further reproduction prohibited without permission.

inputs with an ADC for each. This means that only two of the 14-bit inputs on the GC 4016 are used. The inputs of the GC4016 pass through a crossbar switch which allows any of the inputs to be switched to any or all of the receiver channels. Each receiver channel then has a numerically controlled oscillator (NCO) and a digital mixer. The frequency and phase offset of each oscillator can be set independently. The frequency of each NCO is set by a 32 bit register that divides the clock frequency. For a clock frequency of 65 MHz, the tuning resolution of each NCO is 0.015 Hz. The phase offset of each NCO is set by a 16 bit register that is divided into 360 degrees. This corresponds to a phase resolution of less than 0.006 degrees. Each NCO outputs two frequency signals, one in phase (I) and one in quadrature (Q). These I and Q signals are mixed with the sampled signal from the A/D converters, providing in phase and quadrature mixed signals. The I and Q signals are the passed to a coherent integrator comb (CIC).

The CIC takes a number of samples from the signals and integrates, or averages, them, increasing the signal-to-noise ratio and providing decimation. The CIC in each receiver channel of the CIC is has selectable decimation factors of 4 to 4096. If the GC4106 is operated as two mid band receivers, the decimation factors double to 8 to 8192. Similarly, if the GC4016 is operated as a single broadband receiver, the decimation factors double again to 16 to 16384. The output of the decimator goes to a 21 tap finite impulse response (FIR) filter.

This filter has 21 register-programmable 16-bit coefficients. In a typical configuration, the NCO is set to mix the input sampled RF signal to baseband, and the 21-tap FIR, designated CFIR in Figure 24, is used for coarse filtering. This CFIR filter further decimates the signal by a factor of two. After the CFIR filter is another stage of filtering. This next stage of filtering is a 63-tap register-programmable FIR filter. This filter is used for more precision filtering and is designated PFIR (precision finite impulse response filter) in Figure 24. Again, this stage of filtering decimates the digital signal by a factor of two. After the PFIR stage of filtering, the digital signals are passed to a digital resampler.

Reproduced with permission of the copyright owner. Further reproduction prohibited without permission.

The digital resampler can resample the filtered signal to any arbitrary data rate between almost 0 Hz to the clock rate, which is nominally 65 MHz. The resampler contains several stages of bit shifting and fine gain which allow the amplitude levels of the output data to be adjusted. Also in the resampler is a 512 tap symmetric filter which can be switched arbitrarily between output receiver channels or can be divided into four 128 tap filters, one for each receiver channel.

The output of the resampler is passed on the GC214 bus to some data framing and control chips, the stored as I and Q samples in first-in-first-out (FIFO) memory. There is a FIFO memory region on the GC214 designated for each of the four receiver channels. The data stored in these FIFOs can be accessed by the PCI controller for distribution over the PCI bus. Direct memory access (DMA) can be used to transfer data over the PCI bus from the FIFOs to local memory space on the host computer.

The GC214 is a small, compact system that can be run on any suitably fast desktop computer. The GC214 can sample two RF signals with frequencies up to half the clock rate (due to Nyquist limitations). These two sampled RF signals can be passed to any of four independent receiver channels. Each receiver channel can mix, filter, and resample the signal, providing four independent I and Q sample outputs over the PCI bus for processing on the host computer.

Implementing the Digital Receiver

Since the HF radar at Kodiak is part of an international network of radars, operating in cooperation to provide a real-time data product, it was vital that the upgrade of the receiver have as little impact as possible on the normal operations of the radar. Also, since the radars that constitute the SuperDARN network are used for global scale research, all of the radars run the same operating software. For this reason also, it was vital that the new receiver not impact or require changes in the operating software. The new digital receiver had to be essentially transparent to the typical operations of the radar. At the same time, however, the new receiver has the ability to add new

Reproduced with permission of the copyright owner. Further reproduction prohibited without permission.

experimental capabilities. This means that the implementation of the receiver had to allow for future radar control software to take full advantage of the capabilities of the receiver. The following sections present the thought processes and steps taken to get the new receiver to work transparently with the existing operating code, while allowing flexibility for future experiments.

QNX

The first thing to consider in implementing the digital receiver for the HF radar at Kodiak was how to write the software to run the receiver. The HF radar at Kodiak is controlled by two personal computers, as are all of the other radars in the SuperDARN network. The main computer hosts the operating and data processing software. The other computer, the timing computer, controls the precise timing signals necessary to operate the radar. Both of the computers employ a real-time operating system called QNX.

QNX is a real-time operating system that is ideally suited for the real-time control and processing required for a radar system. There were no drivers available for the GC214 digital receiver under QNX, so all of the software required to run the GC214, and to interface it with the existing radar control software had to be written from scratch.

All of the software used to control and perform real-time processing on all of the radars in the SuperDARN network is written in C. Since all of the software is common to all of the radars, the source code for the control and operation of the radars is distributed to each radar site and compiled locally. To get the new receiver to work with this system, some modifications to the source code had to be made.

Existing control code structure

Within the radar operating software there are several layers of operating code. The uppermost layer is the radar control program (RCP). There are numerous RCPs installed on each radar, and each can be run at any time. There are only a couple RCPs

Reproduced with permission of the copyright owner. Further reproduction prohibited without permission.

that are used typically. Others are used for specific experiments at specific times. A RCP is the code that coordinates the operation of the radar at the highest level. Each RCP makes calls to lower level functions that actually control the hardware of the radar, and process the data. These lower level functions make calls to even lower level functions. Often there are many layers of function calls between the RCP and the actual control of the radar hardware and processing of the collected data. The RCPs coordinate the functions required to initialize the radar, set many parameters in the radar, make high level calls to collect data, send the collected data to the high level functions to be processed, gather the processed data, and make calls to store and save the processed data.

As has been mentioned, the control code for the HF radar at Kodiak is very complex, and there are many layers of code. There is code to run the GPS timing receiver, code to run an A/D converter that samples the baseband signal, and code to interface with the digital input/output system that sends timing and control signals. There is code to turn the raw baseband signals into autocorrelation functions, code to determine fitted parameters based on the autocorrelation functions, and code to analyze and extract useful information from the fitted parameters. There is code to store the data, send real-time data over the internet, and code to monitor the functions and operation of the radar. At a higher level there is code, control programs and scheduling programs, to orchestrate all of the previously mentioned functions and to schedule the operation of the radar. There is also visualization software to allow incoming data, both raw and fitted, to be monitored in real-time. All said, the software that controls the radar is very complex. Figure 25 shows a simplified, albeit still rather complex, flow chart of the software that runs the HF radar at Kodiak.

Reproduced with permission of the copyright owner. Further reproduction prohibited without permission.

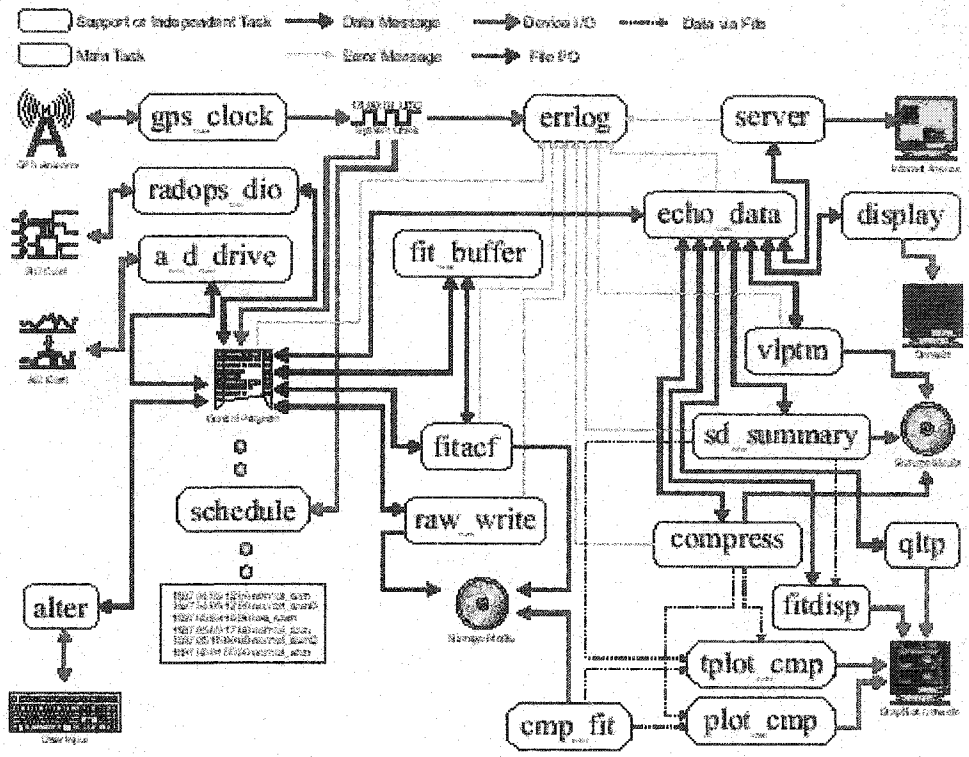

Figure 25: Software flow diagram for the HF radar at Kodiak Island [University of Leicester, 2001]

This figure shows that the software functions of the radar are very complex and interconnected. Fortunately, most of the radar control software did not need to be changed to implement the new digital receiver. There were two main concerns in implementing the new digital receiver for the radar at Kodiak. The first was to create a receiver system that is efficient, reliable and adequate for the purposes of the radar. The second is implementing it in such a way that it integrated seamlessly with the existing system and operates without major modification to the existing structure of the radar operating code.

Hardware control

Computer Interactions

Reproduced with permission of the copyright owner. Further reproduction prohibited without permission.

The two parts of the radar code illustrated in Figure 25 that interact directly with the hardware of the radar are the ADC driver, *a_d_drive*, and the digital input/output driver, *radops_dio*. The code *gps_clock* also interacts with the hardware of the GPS receiver, but is used only to set the system clock on the both the control computer and the timing computer. The digital input/output (DIO) driver controls the digital input/output card, which resides in the timing computer, and the ADC driver controls the A/D converter, which resides on the main computer. The timing computer has all interrupts disabled, and is solely responsible for the timing signals that control the radar. These timing signals are sent to the hardware of the radar over the digital output lines of the DIO card. The radar control program generates a description of the timing signals require for the current operation of the radar, and send this description over a local area network to the timing computer. The timing computer then distributes the proper control signals precisely. A diagram of this interaction is provided in Figure 26.

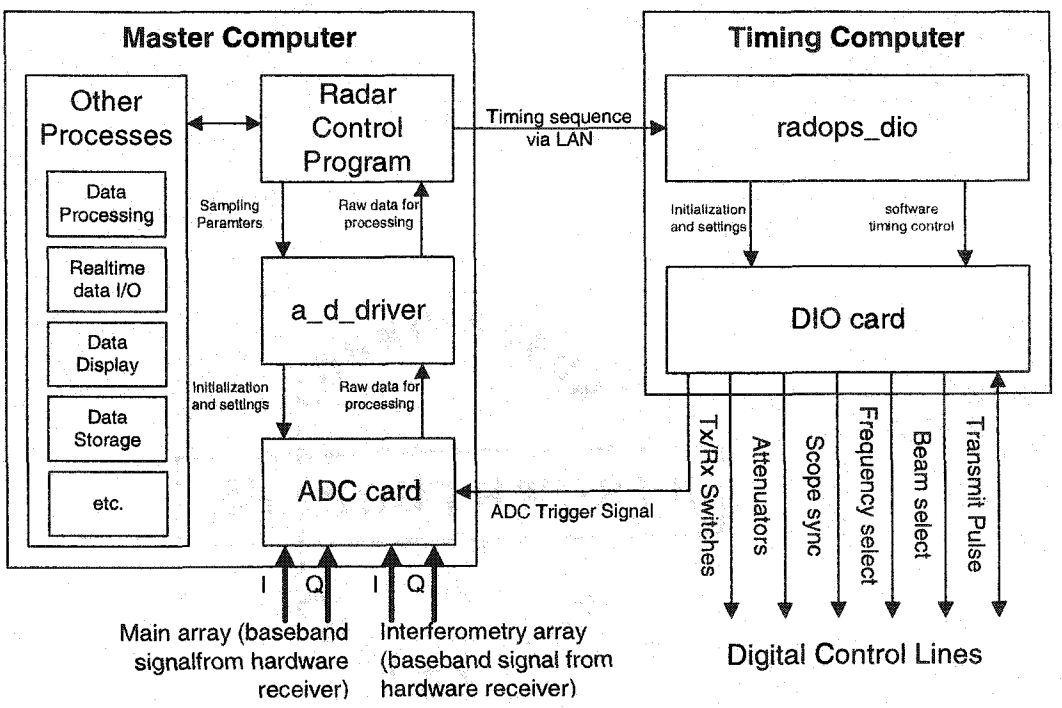

Figure 26: Block diagram of the radar control computers

Reproduced with permission of the copyright owner. Further reproduction prohibited without permission.

The digital output lines of the timing computer control such functions as transmitter frequency, transmission and reception via several stages of transmit/receive switches, beam positions, and diagnostic functions including an oscilloscope synchronization signal used to trigger an oscilloscope for looking at the received signal. The DIO card on the timing computer also provides the sampling signal that controls when the ADC in the main computer samples the baseband signal. The ADC driver, *a_d_drive*, signals the main control program when the proper number of samples has been collected and the control program then processes and handles the data.

Timing sequence

The desired radar hardware control signals are created as a timing sequence by the RCP. The timing sequence is then sent over a local area network (LAN) to the timing computer. The timing computer then converts the timing sequence into a number of digital signals that are interfaced with the radar hardware via the DIO card. A typical timing sequence is illustrated in Figure 27.

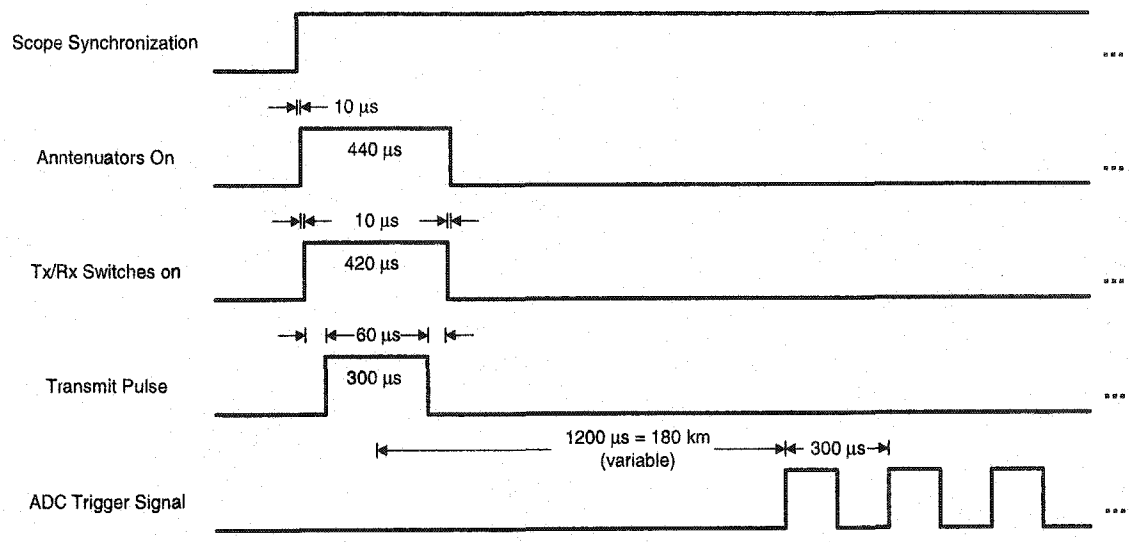

Figure 27: Hardware control signals from the timing computer

Reproduced with permission of the copyright owner. Further reproduction prohibited without permission.

The scope synchronization signal is the first signal in the timing sequence. This signal provides a rising edge for oscilloscope triggering, which allows all of the other control signals, transmit signals, and received signals to be viewed accurately on an oscilloscope. Ten μs after the scope sync signal rises, the attenuators in the receiver are switched on. There are several attenuators in the pre-existing hardware receiver, and switching them on prior to transmitting provides a level of protection between the transmit path and receive path of the radar system. Another 10 μs after the attenuators are switched on, the transmit (Tx) and receive (Rx) switches are switched to the transmit position. Sixty μs after the Tx/Rx switches are switched, the transmit pulse is sent. This 60 μs delay allows the switches enough time to properly switch and helps ensure that little to no transmit power is routed directly into the receiver. After the transmitted pulse is completed, the Tx/Rx switch is returned to the receive position, and the attenuators are returned to their previous state. At a lag of 1200 μs after the middle of the transmit pulse, the triggering signal for the ADC is started. This 1200 μs delay corresponds to 180 km in range. In the typical operating modes on the pre-existing radar system, there was no data collected before 180 km. A leading edge is generated in the ADC trigger signal every 300 μs. This corresponds to the pulse witch of 300 μs and the typical range resolution of 45 km. It should be noted that all of the time separations in the timing sequence are multiples of 10 μs. While the timing sequence is changeable in software, ten μs is the fundamental timing unit in the timing computer, allowing the output of the DIO card to change states only every 10 μs. This is the reason that the maximum attainable sampling period of the pre-existing system is 20 μs, corresponding to a sampling frequency of 50 kHz.

Interfacing with the existing system

To fulfill the design requirement that the new digital receiver have as little impact as possible on the structure of the radar control software and to maintain compatibility with existing RCPs it was decided that the driver for the digital receiver should mimic the

Reproduced with permission of the copyright owner. Further reproduction prohibited without permission.

driver for the old ADC. This is a logical decision because the ADC driver is the piece of code that provides the raw baseband samples to the rest of the radar software for processing and analysis. To make the upgrade as seamless as possible, the driver for the digital receiver will replace the ADC driver, and will maintain all of the original functions of the ADC driver. To understand the development of the new digital receiver driver, a brief overview of the old ADC driver is presented.

ADC Driver

In QNX, the standard form of driver development divides a driver into two parts. One part, which will be referred to as the 'driver front-end', contains all of the functions of the driver. When a call is made to one of the functions, the driver front-end passes a message to the second part of the driver, which will be referred to as the 'body' of the driver. The body of the driver is the code that actually controls the hardware. So, in a typical QNX driver, the front-end contains the functions that can be incorporated into software that uses the driver. The body of the driver waits for messages from the front-end, and, when a message is received, performs some task controlling the hardware.

In the existing ADC driver, the front-end contains seven functions. These functions are summarized in Table 4.

Reproduced with permission of the copyright owner. Further reproduction prohibited without permission.

Table 4: Summary of the ADC driver functions

Function Name	Description
do_scan	Requests that a 'scan', or the collection of data, should begin. This function sets the ADC to wait for the sample clock signals from the DIO card, and sample accordingly
get_buf_adr	The ADC driver sets up several memory buffers into which the raw samples can be placed. This function requests the memory address of these buffers.
get_buf_num	The ADC driver sets up several memory buffers into which the raw samples can be placed. This function requests the number of memory buffers that have been created.
get_buf_size	The ADC driver sets up several memory buffers into which the raw samples can be placed. This function requests the size of the memory buffers.
get_scan_reset	The ADC driver sets up an interrupt proxy that indicates when the ADC has places a specified number of samples in a memory buffer. This function request the process identifier of that interrupt proxy so that it can be triggered by software.
get_scan_status	This function request the staus of the last DMA tranfer of data from the ADC into one of the memory buffers. This serves as a flag to the rest of the software indicating whether the data in the buffers is valid.
scan_reset	This function triggers the interrupt proxy which has the effect of reseting the ADC driver if a DMA transfer fails.

When these front-end functions are called, the driver front-end passes a message to the body of the driver which actually executes the function. For example, the function *do_scan* is the one function that tells the ADC to prepare to start sampling. When *do_scan* is called, the front-end messages the body to set all of the proper control and status registers on the ADC card, and sets the ADC card to sample when clocking signals are received from the DIO card. The buffer related functions, such as *get_buf_adr*, *get_buf_num*, and *get_buf_size*, are used to get parameters about the data buffers to which the ADC will store the baseband samples. The functions *get_scan_reset*, and

Reproduced with permission of the copyright owner. Further reproduction prohibited without permission.

scan_reset are used to reset the ADC driver should part of the driver fail. The function *get_scan_status* allows other parts of the radar control and processing code to check the validity of the samples in the current buffer.

As has been mentioned, the body of the ADC driver simply sits and waits for messages from the driver front-end. When a message is received, the body of the driver performs the function. The pseudo code provided in Figure 28 illustrates the operation of the body of the driver.

```
MAIN
    • Create four 8 kB data buffers in memory
    • Initialize any interrupts
    • Initialize the ADC
    • Etc.
    INFINITE LOOP
        Wait for message
        If message is received, then
                If message is GET_BUF_NUM, then
                        Return number of buffers
                If message is GET_BUF_SIZE, then
                        Return size of buffers
                If message is GET_BUF_NUM, then
                        Return number of buffers
                If message is DO_SCAN
                        Set the A/D converter to wait for clock signals, collect x number
                        of samples, and put them in a buffer
                .
                .
                .
    BACK TO BEGINNING OF LOOP
```

Figure 28: Pseudo code illustrating the ADC driver structure

When the body of the driver is initially started, it performs some initialization functions, such as configuring the PCI bus for DMA (Direct Memory Access) transfers, creating data buffers, initializing the ADC card, etc. Once the initialization functions are complete, the driver essentially sits in an infinite loop waiting for messages from the driver front-end. Again, when a message is received, the body of the driver performs the functions associated with that message, and then returns to the infinite loop waiting for the next message.

Reproduced with permission of the copyright owner. Further reproduction prohibited without permission.

Changing the pre-existing ADC driver into a digital digital receiver driver

To maintain compatibility with the rest of the existing radar software, all of the ADC driver functions had to remain in the digital receiver driver and had to function equivalently. To accomplish this goal, parts of the pre-existing ADC driver were not changed, and parts were changed drastically. In addition, new functions and controls were added.

One minor change to the pre-existing ADC driver was adapting the initialization process performed when the driver is first started to initialize the digital receiver rather than the ADC. In this initialization process, the ADC driver set up several memory buffers in which to place the baseband sample for access by the rest of the radar control code. The old ADC driver allowed the number of buffers created to be specified as a parameter of the system. The driver allowed between two and eight buffers to be created, depending on the desired operation of the radar. This buffer allocation was changed to a fixed number of four buffers, one for each of the GC214 receiver channels. Another small change in the initialization process was the allocation of the size of the data buffers. Originally, the ADC driver allocated 8 kB buffers. This size allocation was changed to 32 kB to allow for the greater number of samples required for the edge detection of meteor echoes. The initialization process of the ADC driver also sets the driver priority. The priority defines how processor time is allocated to the driver. The driver priority of the original ADC driver was maintained for the new digital receiver driver. The register settings on the old ADC card were very straight forward. Little initialization was required to set-up the ADC for interaction with the software. On the GC214, there are a number of configuration registers that must be assigned before the digital receiver will interact properly with the software. A routine to assign these configuration registers was added to the initialization process of the new digital receiver driver. There are no interrupts used on the new digital receiver, so the interrupt initialization routines present in the original ADC driver were removed.

Reproduced with permission of the copyright owner. Further reproduction prohibited without permission.

As has been mentioned, the pre-existing ADC driver had several functions that retrieved parameters about the data buffers into which the driver placed the baseband samples. All of the code that reports the number of buffers, size of the buffers, and addresses of the buffers has remained unchanged. Because there are no interrupts used in the implementation of the new digital receiver, the function *get_scan_reset* was obsolete. However, to maintain compatibility with existing code that makes use of *get_scan_reset* this function was kept in the new digital receiver driver. The new version of the function *get_scan_reset* simply returns a dummy value for the interrupt proxy. The function *scan_reset*, which receives the interrupt proxy provided by *get_scan_reset*, now simply resets the digital receiver card. Put simply, the old system requested a proxy from the ADC driver, and then reset the ADC driver by triggering the proxy. The new system simply passes a dummy proxy, and resets when *scan_reset* is called, without triggering a proxy. The function *do_scan* is where the significant changes that allow the new digital receiver to behave like the old ADC have been made.

Data collection Triggering

In the pre-existing radar control software, *do_scan* simply set some configuration registers on the ADC configuring it to collect a number of samples based on an external trigger signal, and then, when the specified number of samples had been collected, perform DMA transfer of those samples into a data buffer and trigger an interrupt. To maintain compatibility between the new digital receiver and the rest of the radar operating software, this basic model of operation is used in the new digital receiver driver.

The old ADC received a sample trigger signal from the timing computer. This signal told the ADC exactly when to take a sample of the baseband signal. When the implementation of the new digital receiver was considered, there were a couple available options for triggering the collection of data. One option was to use software to write a register triggering the start of data collection on the GC214. A software trigger such as

Reproduced with permission of the copyright owner. Further reproduction prohibited without permission.

this, however, has some problems. The biggest problem is timing. When a software trigger is used, there is some ambiguity in when the trigger is actually initiated. This is especially true when a multitasking operating system such as QNX is used. For example, if a transmit sequence is initiated, then some other process takes control away from the driver for a short time before the software data collection routine is triggered, then there will be some unknown time delay between the start of the transmit cycle and the data collection cycle. While QNX is considered a real-time operating system, there can still be timing ambiguities on the order of several microseconds, which is unacceptable in a timing dependent system such as a radar. The other option for triggering the start of a data collection cycle was to use a time accurate control line from the timing computer.

There are several digital timing control lines coming from the timing computer as illustrated in Figure 27. The GC214 has four external inputs. Two of the inputs are the RF/IF inputs to the ADC on the digital receiver. One of the inputs is a clock reference for controlling the clocking functions on the GC214. The fourth input is a synchronization input. This input is intended to allow the functions of several GC214 digital receivers to be synchronized with each other or to some external synchronization control source. This synchronization line is an ideal means by which to trigger data collection on the GC214. The sampling trigger signal from the timing computer would not work as a synchronization source for the new digital receiver because it triggers many times in a data collection sequence. Fortunately, however, there is a timing signal in the timing sequence of the timing computer that is triggered only once per data collection cycle. The scope synchronization signal is triggered at the beginning of each transmission/data collection cycle, and is used to trigger the synchronization line on the new digital receiver. There are some minor problems with triggering the start of data collection on the scope sync signal, namely that the old ADC did not begin sampling until some time after the middle of the first transmit pulse. The new system begins data collection well before the first transmit pulse. This problem was solved easily, however, by simply ignoring the several data points taken before 1200 μs after the transmit pulse.

Reproduced with permission of the copyright owner. Further reproduction prohibited without permission.

The new interactions between the timing computer and the master computer are shown in Figure 29.

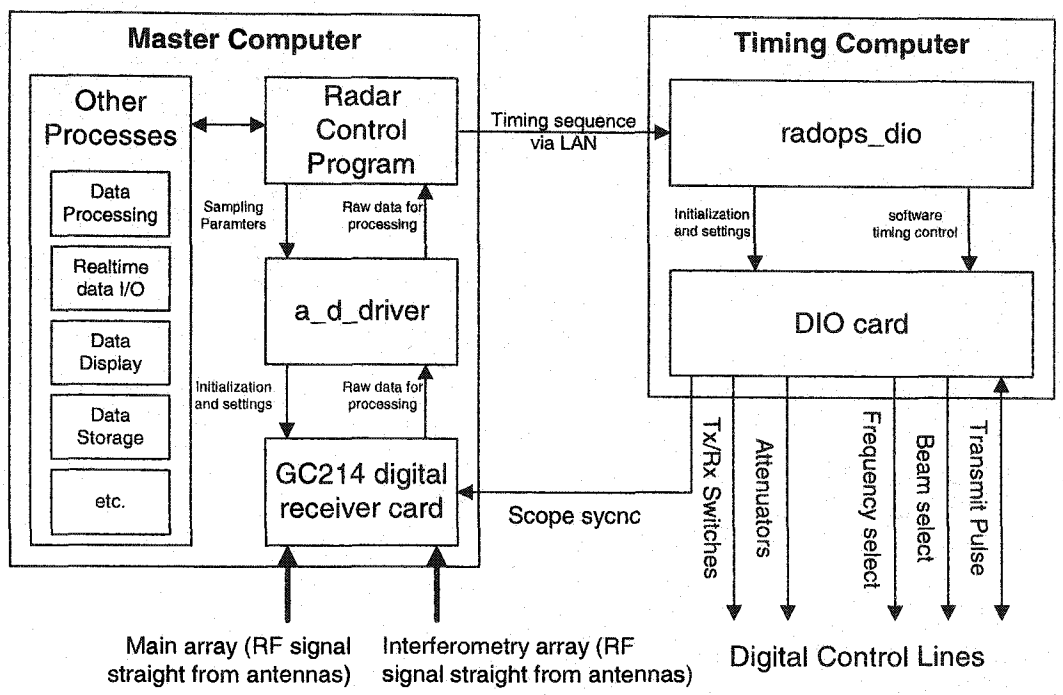

Figure 29: Block diagram of the radar control computers after the digital receiver implementation

In the implementation of the digital receiver, the data collection control signal is still generated by the timing computer. Originally the ADC trigger signal was used to trigger the collection of data for each sample. Now, in the new system, the scope sync signal is used to trigger the beginning of data collection. In the old implementation of the ADC driver, the function *do_scan* initialized the ADC and set it to wait for a sample trigger signal from the timing computer. In the implementation of the new digital receiver, the function *do_scan* initializes the GC214 and sets it to wait for the scope sync signal to start collecting data.

Reproduced with permission of the copyright owner. Further reproduction prohibited without permission.

Initializing the receiver – Receiver functions

In the pre-existing receiver implementation there was a hardware receiver that amplified the RF signal from the antennas, mixed the RF signal to an IF, amplified and filtered the signal, mixed the IF signal to baseband and provided the baseband signals to the ADC on the master computer for sampling and processing. In the implementation of the new digital receiver, all of the functions of the old hardware receiver are now on the GC214 and must be controlled in software. These receiver functions include sampling the RF signal, mixing the RF signal to baseband, decimating the signal, filtering the signal, formatting the output and providing the filtered baseband samples to the rest of the radar control software.

Clock signal

In a typical backscatter radar system, a local oscillator, or a series of local oscillators and mixers, is used to generate the transmitted signal. Typically, the same local oscillators are used to mix the echo signal to some IF or to baseband. In the GC214 there are four numerically controlled oscillators used for mixing the echo signal to baseband. Since the oscillators used to create the transmit signal are different from the oscillators used to mix the echo signal to baseband, frequency and phase drift are a concern. For example, if the frequencies of the transmit oscillator and the receive oscillator drift with respect to each other even slightly, then the baseband data will provide erroneous information about the target. One way to overcome such a problem is to provide some phase or frequency reference to both the transmitter local oscillator and the receiver local oscillator. This ensures that the frequencies and phases of the two oscillators do not drift with respect to each other. Fortunately, the pre-existing transmitter and receiver system on the HF radar at Kodiak used IF mixing. There are two local oscillators used to generate the transmit signal. Both of these local oscillators are

Reproduced with permission of the copyright owner. Further reproduction prohibited without permission.

phase-locked to a 10 MHz source. One of the local oscillators is fixed to a frequency of 40.625 MHz. In the implementation of the digital receiver, this 40.625 MHz is used as the clock reference on the GC214 digital receiver. This clock reference provides the sampling trigger to the two ADCs on the GC214 and provides the frequency reference to the four NCOs. Using a phase-locked reference for both the hardware transmitter and the digital receiver ensures that frequency and phase drift between the transmitter and receiver is not a problem.

Sampling

There are two RF/IF inputs on the GC214 digital receiver. Each of these inputs is digitized by an Analog Devices model AD6644AST-65 analog-to-digital converter. The ADC6644AST-65 is a 14-bit ADC that is triggered by the external clock input on the GC214 provided by the 40.625 MHz reference signal. Since the HF radar at Kodiak is designed for operation over the frequency range of 8 to 20 MHz, a sampling rate of 40.625 fulfills the Nyquist criterion, which states that the sampling frequency be at least twice the maximum frequency of the signal to be sampled. A lowpass filter with a cutoff frequency of 21.4 MHz sits between the antennas and the digital receiver to act as an anti-aliasing filter. The sample rate is fixed to the reference clock of 40.625 MHz and is not software controllable.

Mixing

The output of each of the two ADCs can be routed to the input of any of the four GC4016 digital receiver channels on the GC214 digital receiver. The first stage in each of the receiver channels is a digital mixer. The sampled RF signals from the ADCs are mixed with signals from a numerically controlled oscillator (NCO). There is one NCO in each of the four receiver channels. The frequency of each NCO is programmed by a 32 bit register that defines a clock division factor. There is a routine in the new digital receiver driver that reads the transmit frequency of the radar as a parameter from the DIO

Reproduced with permission of the copyright owner. Further reproduction prohibited without permission.

driver, then sets the frequency division register accordingly. The sampled RF signal is mixed in the digital mixer with the local NCO to provide a baseband signal at the output of the mixer.

Decimation

After the mixing stage in each of the four receiver channels, there is a coherent integrator comb (CIC) decimator. The CIC has several control registers associated with it. One of these registers sets the decimation factor. In the implementation of the new digital receiver, decimation is used to set the output data rate. For example, in a typical operating mode, the HF radar at Kodiak has a range resolution of 45 km. This rage corresponds to a sample period of 300 μs and a sample frequency of 3.333 kHz. All of the existing radar processing code expects a buffer of samples taken at a sample rate of 3.333 kHz. In the case of the new digital receiver the RF signal is sampled at 40.625 MHz. To attain an output sample rate of 3.333 kHz, a decimation factor of 12189 is required (40.625 MHz / 3.333 kHz = 12189). There is an algorithm the new digital receiver driver that reads the desired range resolution as a parameter of the radar software and sets the decimation of the CIC accordingly. It should be noted that there are two stages of finite impulse response filtering after the CIC. Each of these stages of filtering decimates the signal by a factor of two, so the decimation factor of the CIC is set to be one-fourth of the total decimation value required. Each receiver channel on the GC2014 is capable of total decimation factors from 16 to 16384. With the input clock rate of 40.625 MHz, and these decimation factors, the GC214 is capable of output data rates between 2.48 kHz and 2.539 MHz. There are capabilities in the new digital receiver driver to take advantage of this range of output sample rates, but typical operation the new digital receiver sets the output data rate to the same data rates used in the old analog receiver system. New functions that allow use of the added capabilities of the digital receiver will be discussed later.

Reproduced with permission of the copyright owner. Further reproduction prohibited without permission.

Filtering

Following the CIC decimator in each of the receiver channels, there are two stages of filtering. The first is a 21 tap FIR filter. This filter provides coarse filtering and is designated CFIR in Figure 24. The second stage of filtering is a 63 tap filter which provides more precise filtering. This filter is labeled PFIR in Figure 24. Combined, these two filters provide all of the baseband filtering in the new digital receiver.

The filter coefficients for both of these filters are determined by first defining the ideal frequency response of the filters in the frequency domain. An frequency response of and ideal discrete lowpass filter, $H_{LP}(e^{jw})$, is simply a step function defined by

$$H_{LP}\left(e^{j\omega}\right)=\begin{cases}1, & |\omega| \le \omega_c, \\ 0, & \omega_c < \omega \le \pi.\end{cases} \tag{50}$$

where ω is frequency in radians, and ω_c is the desired cutoff frequency, and 2π is the sample frequency [Mitra, 2001]. The impulse response coefficients, $h_{LP}[n]$, of this ideal filter are

$$h_{LP}[n]=\frac{\sin(\omega_c n)}{\pi n}, \quad -\infty \le n \le \infty. \tag{51}$$

Since there are only 21 coefficients in the CFIR filter and 63 in the PFIR filter, the infinite impulse response presented in equation 51 cannot be realized. A truncated impulse response must be used, but this introduces the oscillatory behavior of Gibbs phenomenon [Mitra, 2001]. To minimize the effects of Gibbs phenomenon, the truncated filter coefficients are multiplied by a Hamming window. Also, to provide linear phase through the filter, symmetric filter coefficient filters are used. The 21 filter coefficients of the both the CFIR filter and PFIR filter are shown in Figure 30.

Reproduced with permission of the copyright owner. Further reproduction prohibited without permission.

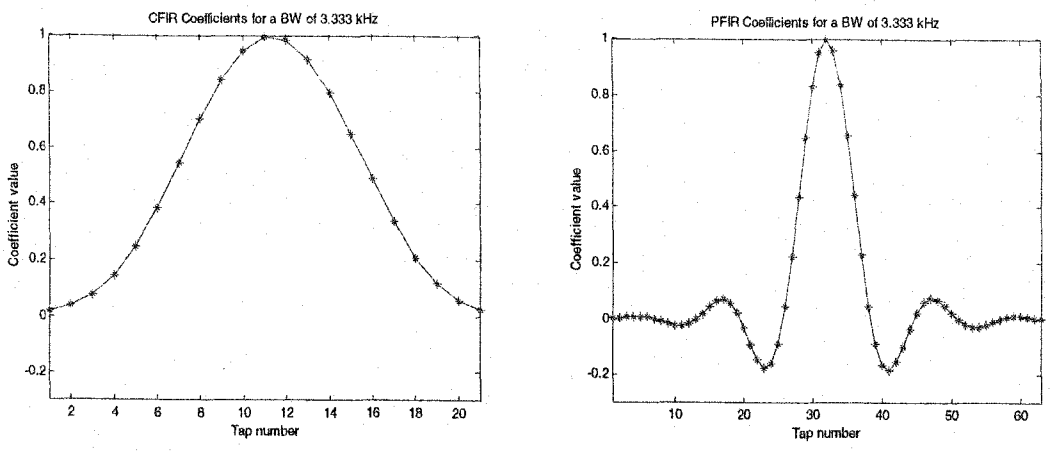

Figure 30: CFIR and PFIR filter coefficients for a filter bandwidth of 3.333 kHz

It should be noted that since the CFIR filter decimates by a factor of two, the sample rate into the PFIR filter is half of the sample rate into the CFIR filter. Since the sample rate into the CFIR is twice the sample rate into the PFIR, and the CFIR has fewer filter coefficients, the frequency response of the CFIR for narrow bandwidths is less than ideal. When the two filters are used together, however, a good frequency response with good out-of-band rejection can be achieved. The frequency responses of both the CFIR filter and the PFIR filter are provided in Figure 31.

Reproduced with permission of the copyright owner. Further reproduction prohibited without permission.

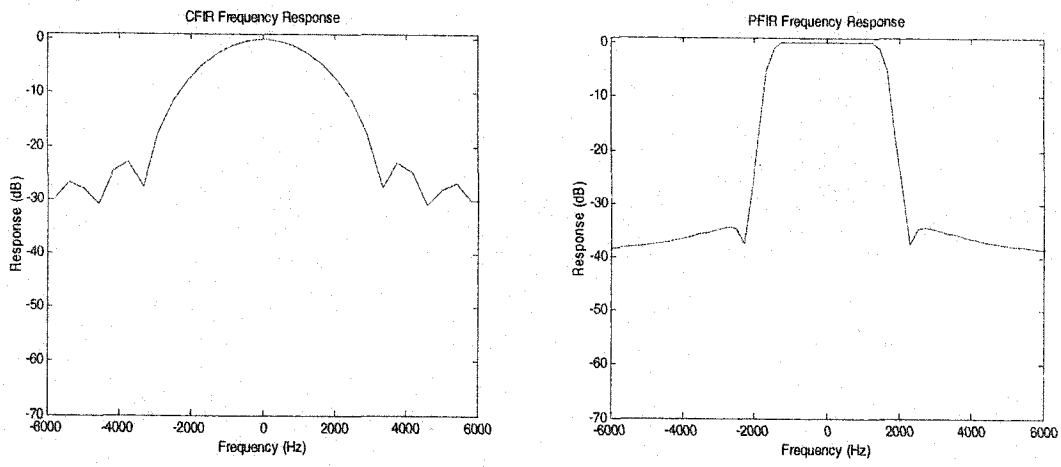

Figure 31: Frequency responses of the CFIR and PFIR filters for a bandwidth of 3.333 kHz

Since the CFIR filter and PFIR filter are cascaded, the frequency response of the two filters in series acts on the baseband signal in the digital receiver. The frequency response of the two filters in series is provided in Figure 32

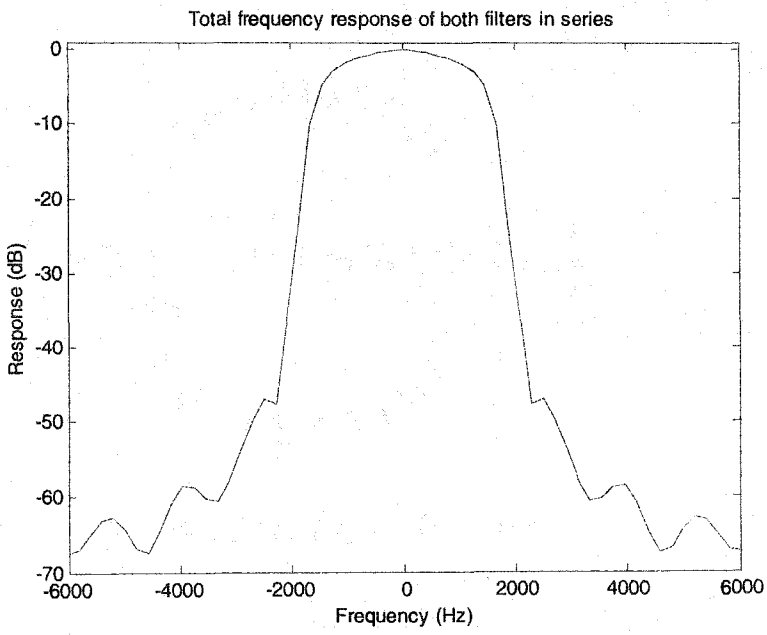

Figure 32: Total frequency response of the filtering stages on the digital receiver with a specified bandwidth of 3.333 kHz

Reproduced with permission of the copyright owner. Further reproduction prohibited without permission.

The final filter has a 6 dB bandwidth of 3.333 kHz, and the frequency response drops to less than -55 dB in an octave and less than -65 dB in two octaves. This filter provides a more than sufficient frequency response for the typical baseband filtering required for the HF radar at Kodiak.

In typical operation, the SNR of the radar is maximized when a matched filter is used. For the typical pulse width of 300 μs, the corresponding matched filter bandwidth is 3.333 kHz. The typical matched filter used in the new digital receiver is illustrated in Figure 32. There is an algorithm in the new driver that reads the transmit pulse width as a parameter of the system, and then calculates the appropriate matched filter coefficients. There is also a new function that allows arbitrary filter bandwidths to be specified. This function is not implemented in typical operation because a matched filter is ideal for ionospheric echoes, but is available for other experimental goals, such as increased range resolution edge detection of meteor trails.

Resampling

The GC4016 receiver chip on the GC214 digital receiver contains a resampler that is capable of resampling the baseband signal at rates up to half the input clock, which allows filtered baseband data to be clocked from the GC214 at an arbitrary rate. This feature is ideal for a system that requires a specific data rate, but the resampler does, however, introduce some time latency into the signal path through the digital receiver. To avoid this added latency in the digital receiver, the resampler is not used. All of the output data rate control is implemented in the CIC decimation stage.

Gain

Each of the receiver channels has two stages of gain control. One stage, which offers coarse gain control, is a simple bit shifter that provides gain factors that are multiples of 2. The other stage provides fine gain control from a factor of 0.001 to a

Reproduced with permission of the copyright owner. Further reproduction prohibited without permission.

factor of 16. These gain stages are designed to allow gain compensation for the filtering stages. In the new digital receiver driver, there is an algorithm that calculates the digital gain in the filter stages, and then adjusts the coarse and fine gain control registers to provide a fixed gain through the digital receiver. The total gain through the receiver has been set to provide output baseband signal levels comparable to those of the old hardware receiver.

Initializing the receiver – Software Initialization

Implementing the new digital receiver driver in a way such that it seamlessly replaces the old hardware receiver and ADC required some changes to the radar control software. As has been mentioned, minimizing these changes and the effects they have on the operation of radar system was one of the most important design goals of this new receiver system. It has also been mentioned that the pre-existing ADC driver was used as a software model for the new digital receiver driver, and that all of the functions of the old ADC driver remain – with some minor changes. The function *do_scan* in the old ADC driver was the function that actually interfaced with the ADC and set it to sample the baseband signal. As has been mentioned, *do_scan* initialized the ADC card, set it to wait for a sample trigger from the timing computer, and set it to DMA transfer the samples to a memory buffer for access by the rest of the radar processing software. The implementation of the new digital receiver maintains the function *do_scan* and its basic procedure of operation. With the new digital receiver, however, there are many more settings required to get the digital receiver to operate properly. Many of these settings have already been discussed. The incorporation of these setting into *do_scan* is presented.

When *do_scan* is called, which occurs every time the radar transmits a pulse sequence, all of the parameters and setting on the digital receiver are calculated and set. The first thing *do_scan* does is set up the data format for the output data of the GC214 digital receiver. The baseband data is written to a FIFO buffer on the GC214 as a 16 bit

Reproduced with permission of the copyright owner. Further reproduction prohibited without permission.

in-phase sample and a 16 bit quadrature sample, in a 32 bit word. After the baseband data format is set, do_scan initiates an initialization routine. This routine, called *init_GC214*, actually calculates all of the parameters and sets all of the settings required to make the GC214 digital receiver operate properly.

The first action taken by *init_GC214* is to perform a master reset of the GC214. Next, the two RF inputs of the digital receiver are routed to appropriate receiver channels. There are two RF inputs and four independent receiver channels on the GC214, so each RF input is routed to two receiver channels. Since one of the RF inputs is the signal from the main antenna array, and the other is from the interferometry array, this configuration allows two receiver channels for each array. Typically, the radar is operated such that one receiver channel for the main array, and one for the interferometry array is dedicated to the normal operating modes of the radar. This allows one channel for each array to be dedicated to other simultaneous experiments, such as meteor edge detection. After the RF inputs have been routed to the proper receiver channels, *init_GC214* initiates several routines to calculate and set the receiver frequency, CIC decimation and output data rate, the CFIR and PFIR filter coefficients, and the coarse and fine gain. These functions have been described previously. Once all of the parameters of the digital receiver channels have been set, *init_GC214* sets a few more control and status registers and returns to *do_scan*.

Once all of the receiver parameters have been set, *do_scan* sets the GC214 to start collecting data when the scope synch single is triggered. *do_scan* then calls another routine, *wait_on_scan*, that monitors the status of the digital receiver. When the receiver has collected a predetermined amount of baseband samples, *wait_on_scan* initiates a DMA transfer of those samples into the memory buffer for access by the processing software.

The net effect of the actions in the new *do_scan* is the same as the function in the old ADC driver. The pseudo code in Figure 33 summarizes the operation of the new digital receiver driver with the modified *do_scan* function.

Reproduced with permission of the copyright owner. Further reproduction prohibited without permission.

```
MAIN
    • Create four 32 kB data buffers in memory
    • Initialize the PCI bus for DMA transfers
    • Etc.
    INFINITE LOOP
        Wait for message
        If message is received, then
                If message is GET_BUF_NUM, then
                        Return number of buffers
                If message is GET_BUF_SIZE, then
                        Return size of buffers
                If message is GET_BUF_NUM, then
                        Return number of buffers
                If message is DO_SCAN
                        Configure output data format
                        INIT_GC214
                                Master reset
                                Route RF inputs to appropriate receiver channels
                                Set receiver frequencies
                                Calculate and set CIC decimation factor
                                Calculate and set filter coefficients
                                Calculate and set the gain
                        Set the GC214 to trigger on the external synch input
                        WAIT_ON_SCAN
                                When scope synch trigger has occurred, collect
                                specified number of baseband samples
                                DMA transfer the baseband samples to a memory buffer
                .
                .
                .

    BACK TO BEGINNING OF LOOP
```

Figure 33: Pseudo code illustrating the new digital receiver driver structure with the modified *do_scan* function.

The new function *do_scan* sets some initialization registers, sets the receiver to collect data on an external trigger, and initiates a DMA transfer of the baseband samples into a shared memory buffer. Then new *do_scan* controls the new digital receiver, yet maintains the same functionality of the old ADC driver function as is required to interface with the rest of the radar control and processing software.

Reproduced with permission of the copyright owner. Further reproduction prohibited without permission.

Other changes to the radar control software

Since the new digital receiver does not behave exactly like the old receiver system, there were some changes that had to be made to the radar control software beyond writing a new driver.

One significant difference between the old receiver system and the new digital receiver is the format of the output baseband samples. The old ADC driver DMA transferred the baseband samples into the memory buffer as interleaved in-phase (I) and quadrature (Q) samples. When the samples were collected from the interferometry receiver, these too were interleaved into the memory buffer. The new digital receiver stores the baseband samples for the main array and the interferometry array independently. In the pre-existing system, the processing software that accesses the data buffer expected interleaved baseband samples. To accommodate the new digital receiver, the processing software that accesses the baseband data buffers was changed to access the data from the main array and the interferometry array independently.

Another difference between the implementation of the new digital receiver and the old receiver is the time at which data collection is initiated. Figure 27 illustrates this difference. On the old receiver system, in a typical mode of operation, baseband samples were not taken until 1200 μs after the middle of the transmit pulse. This delay exists because in the typical modes of operation, no data is collected for the first 180 km of range. In the new implementation of the digital receiver, however, the scope synchronization signal is used to trigger the beginning of data collection. A routine was added to the radar control software to calculate the time difference between the leading edge of the scope sync signal and the leading edge of the ADC trigger signal and to discard the corresponding samples.

The final difference between the implementations of the old receiver system and the new digital receiver system is data latency. In the new receiver system, there is a data latency of 24 samples through each receiver channel. This means that the first 24 samples of each data collection sequence must be discarded. The software that accesses

Reproduced with permission of the copyright owner. Further reproduction prohibited without permission.

the baseband sample data buffer was modified to discard these first 24 samples. However, a data latency of 24 samples at a data rate of 3.333 kHz corresponds to a time latency of 7.2 ms. This means that every time the parameters of a receiver channel change, there is a 7.2 ms delay before valid baseband samples are available. In the typical operation, when a pulse sequence is transmitted every 100 ms, this delay is small. But when fast frequency changes are required, and short data collection times are required, this delay becomes significant. The only place in the pre-existing radar operation code where fast frequency changes and short data collection periods were used was in the clear frequency search. The pre-existing clear frequency search operated by setting the receiver to a series of frequencies about some center frequency of interest, and collecting and integrating a number of samples to calculate the noise power as a function of frequency. With the new digital receiver, such an implementation of the clear frequency search would impose a time latency of 7.2 ms every time the receiver frequency changed. To overcome this problem, an improved clear frequency search method, which takes full advantage of the capabilities of the digital receiver, was implemented. The new clear frequency search sets the filter bandwidths of the digital receiver to cover the whole band of the clear frequency search. The receiver then takes a number of baseband samples at a high sample rate. The baseband samples are then Fourier transformed and the frequency with the lowest power is then selected from the Fourier transform. This method of clear frequency search, utilizing the wide bandwidth and high data rate capabilities of the receiver not only avoids the data latency problem associated with frequency changes, but actually reduces the average time of the clear frequency search from ~200 ms on the old receiver system to ~32 ms on the new system. To accommodate this new clear frequency search, a new function, *do_scan_fclr*, was added to the digital receiver driver. This function allows the radar control program (RCP) to specify a center frequency, a bandwidth, an output sample rate, and a number of samples. The function then sets the frequency and filter bandwidths, collects the specified number of samples, and then transfers those samples into the appropriate data

Reproduced with permission of the copyright owner. Further reproduction prohibited without permission.

buffer. The Fourier transforms, averaging, and frequency selection are then computed by a clear frequency search process.

Hardware Modifications

Since the old receiver has been replaced with the digital receiver some hardware modifications have been made to the HF radar at Kodiak. The most significant modification is the addition of an amplifier chain to the receive path of the radar.

In the old receiver system, the output of the phasing matrix provided the input for the analog receiver. The analog receiver had several stages of amplification, mixing, and filtering to provide the baseband signal to the ADC. A simplified block diagram of the old receiver path is provided in Figure 34.

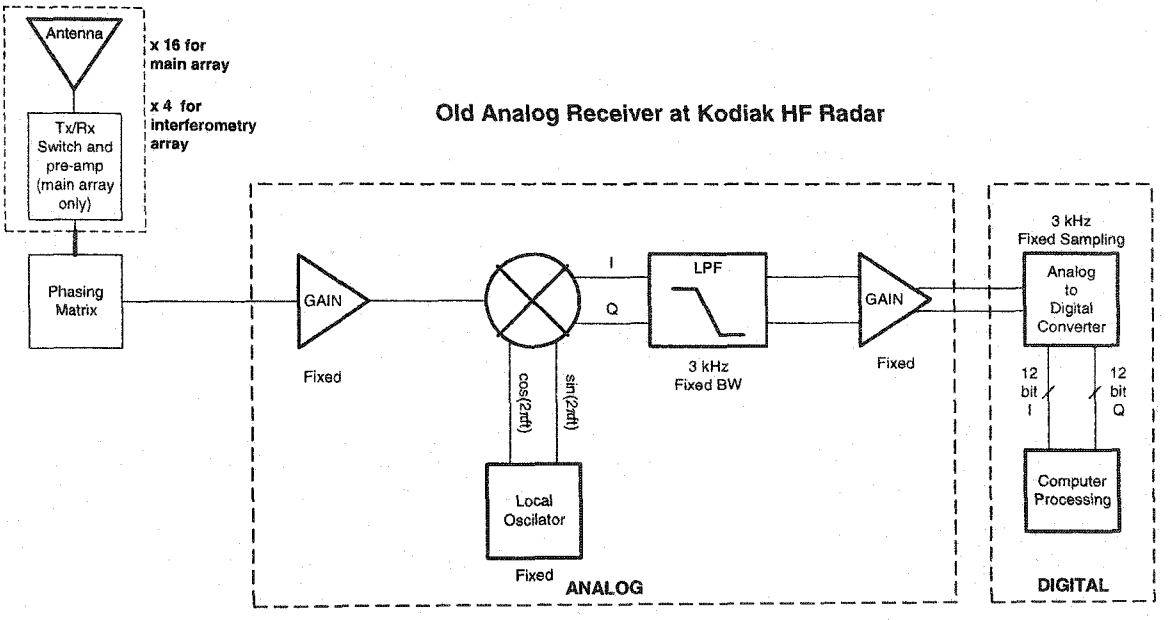

Figure 34: Pre-existing receive path block diagram

Since the new receiver has replaced the analog system, the signal from the phasing matrix must be amplified to the appropriate levels for the inputs GC214 ADCs.

Reproduced with permission of the copyright owner. Further reproduction prohibited without permission.

These ADCs saturate at an in input 1 V_{p-p}, or 4 dBm at 50 Ω impedance. The ADC are also rated at an absolute maximum input of 2 V_{p-p}, or 10 dBm, so the amplifier had to be designed such that the maximum power into the GC214 is less 10 dBm. To prevent damage to the ADC, the final amplifier in the chain was chosen with a 1 dB compression point of 4 dBm. The total amplification of the chain was chosen such that the empirically measured noise floor of -120 dBm on the main array is detectable on the ADCs. Since the detection floor of the GC214 is -92 dBm, a minimum of 28 dB of amplification was required. The amplification chain for the main array has a gain of 33 dB. Since the interferometry array does not have pre-amplifiers, a larger gain of 53 dB was implemented. An amplifier box was designed to house the amplifier chain, anti-aliasing filter, and an extra level of Tx/Rx switch protection for both the main array and interferometry array. A block diagram of the new receive path is provided in Figure 35.

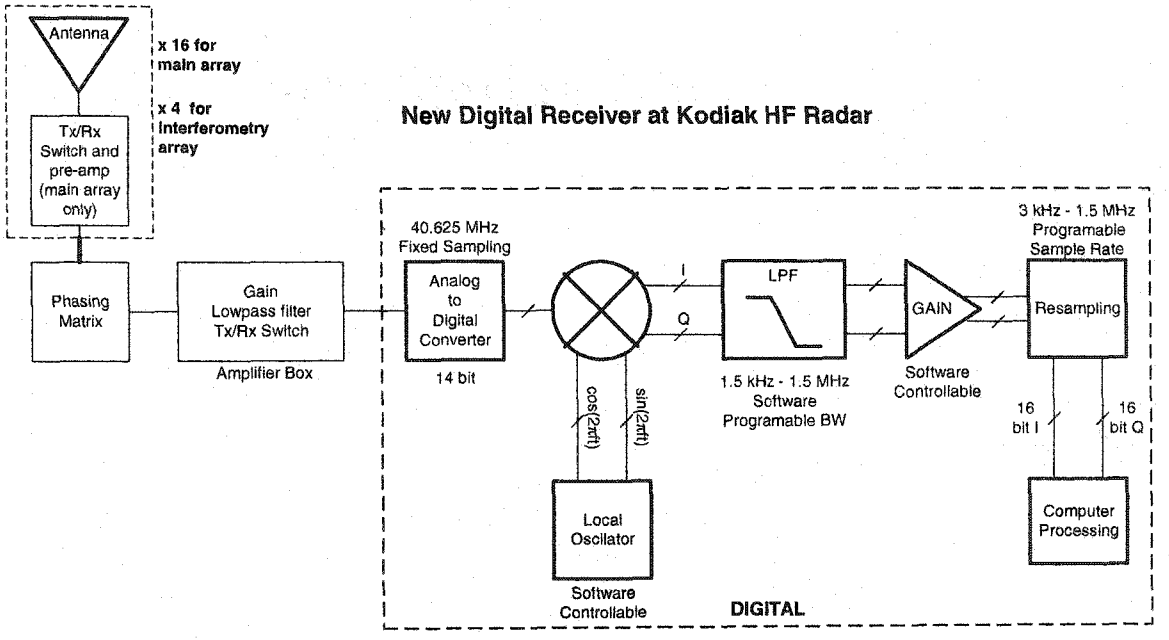

Figure 35: Block diagram of the new receive path

The amplifier box now sits between the phasing matrix and the GC214 digital receiver.

Reproduced with permission of the copyright owner. Further reproduction prohibited without permission.

When the amplifier system was installed, however, a problem on the interferometry array was discovered. Since the interferometry array is not used for transmitting, the antennas do not have Tx/Rx switches as do the antennas on the main array. With the addition of the amplifier box, the only Tx/Rx protection in the interferometry receive path was the new low power Tx/Rx switch. When the main array was transmitting, however, the signal coupled between the main array and the interferometry array was strong enough to unbias the Tx/Rx switch in the amplifier box, and couple high voltages into the GC214. As a temporary fix to prevent damage to the amplifiers and the new digital receiver, 10 dB of attenuation was placed between the phasing matrix and the interferometry channel in the amplifier box. This 10 dB of attenuation, combined with the high loss through the phasing matrix, and the lack of pre-amplification leads to a receiver system noise figure of 29 dB for the interferometry receive channel. Compared to the main array receive channel noise figure of 7.6 dB, this is unacceptable and greatly degrades the performance of the interferometer. Despite the high noise figure on the interferometry receiver channel, there has still been some very good data collected on the interferometry channel. Some of the data will be presented in Chapter 5.

Utilizing the new capabilities of the digital receiver

Up to this point, much has been presented about integrating the new digital receiver into the radar system without major changes to typical operation. The new receiver, however, was implemented to provide new capabilities to the radar system at Kodiak. While the implementation of the new digital receiver was based around making the new receiver behave similarly to the old receiver, a number of new functions were created to allow the new capabilities of the digital receiver to be utilized. These new functions are presented.

In a typical operating mode, the frequency of the receiver is the same as the frequency of the transmitter. In some experiments, however, the ability to set the

Reproduced with permission of the copyright owner. Further reproduction prohibited without permission.

receiver frequency independently from the transmit frequency is desirable. A new function, *set_receiver_freq*, was created to set the receiver frequency to some specified value – independent of the transmit frequency. Also, in typical operation a matched filter is desirable to maximize the SNR of the received signal. However, in some operation modes it is desirable to use different filter bandwidths. A new function, *set_receiver_BW,* was created for this purpose. The function *set_receiver_BW* allows any filter bandwidths within the capabilities of the receiver to be specified. Another function that has been created, and has proved useful, is *set_receiver_offset.* This function allows a fixed frequency offset between the transmitter and receiver to be specified. Another new function, *set_receiver_srate*, allows the user to specify an output sample rate independently from the transmit pulse width. A final new function, *set_meteor_buf*, was created to specify a buffer in which to place the baseband samples for the edge detection of meteor echoes and will be described in more detail later. All of these new functions allow the user to better utilize the capabilities of the receiver. A summary of all of the digital receiver driver functions, including these new functions, is provided in Table 5.

Reproduced with permission of the copyright owner. Further reproduction prohibited without permission.

Table 5: The functions of the new digital receiver driver

do_scan	Calculates and sets the receiver frequency, decimation, filter coefficients, gain, etc. Also sets the digital receiver to trigger data collection based on the scope synch signal, and DMA tranfers the baseband sample into a memory buffer.
do_scan_fclr	Performs the wide bandwidth, high sample rate collection of data required for a clear frequency search.
set_receiver_freq	Allows the receiver frequency to be set independent of the transmitter frequency.
set_receiver_offset	Allows a fixed receiver/transmitter offset frequency to be specified.
set_receiver_srate	Allows the output sample rate of the digital receiver to be set independent of the specified range resolution
set_receiver_BW	Allows the filter bandwidth to be set independent of the transmit pulse width
set_meteor_buf	Specifies a memory buffer in which to transfer samples for meteor processing
get_buf_adr	The digital receiver driver sets up several memory buffers into which the raw samples can be placed. This function requests the memory address of these buffers.
get_buf_num	The digital receiver driver sets up several memory buffers into which the raw samples can be placed. This function requests the number of memory buffers that have been created.
get_buf_size	The digital receiver driver sets up several memory buffers into which the raw samples can be placed. This function requests the size of the memory buffers.
get_scan_reset	This function returns a dummy interrupt proxy. This is a legacy function that has no real application in the digital receiver driver.
get_scan_status	This function request the staus of the last DMA tranfer of data from the digital receiver into one of the memory buffers. This serves as a flag to the rest of the software indicating whether the data in the buffers is valid.
scan_reset	This function resests the digital receiver.

All of the functions have been used in experiments performed on the HF radar at Kodiak and have proved very useful. It is likely that as more experiments are developed to make use of new capabilities of the digital receiver, new functions will be created to aid with those experiments.

Reproduced with permission of the copyright owner. Further reproduction prohibited without permission.

Chapter 5: Meteor Scatter Processing System

The original purpose of the implementation of a new digital receiver for the HF radar at Kodiak was to provide a system that is capable of providing high resolution meteor echo data for the derivation of upper-mesosphere/lower thermosphere wind profiles. The new digital receiver provides the bandwidth and sample rate capabilities required for the high resolution edge detection of meteor trail echoes. Using the interferometric abilities of the radar, combined with the new increased range resolution, the altitude of meteor echoes can be determined with accuracy. The Doppler measurements of these echoes can then be used to calculate the velocities of the meteor trail drift, and create wind profiles for the meteor region. The collection of high resolution meteor echo data and the generation of meteor region wind profiles is presented.

Data Collection and processing

Meteor Echo Profile

Since the reflection of electromagnetic energy from a meteor plasma trail is a specular, the refection point of the electromagnetic pulse from a radar is the point of orthogonality between the transmitted signal and the meteor trail. This leads to the radar geometry previously shown in Figure 1. The echo signal of a radar target is the spatial convolution of the spatial extent of the target with the transmit pulse. Since in the case of the specular reflection from a meteor trail, the spatial extent of the trail is significantly smaller than the spatial extent of the transmit pulse length, the meteor trail appears as an impulse in space, and the echo signal has the same shape as the transmit pulse as illustrated in Figure 36.

Reproduced with permission of the copyright owner. Further reproduction prohibited without permission.

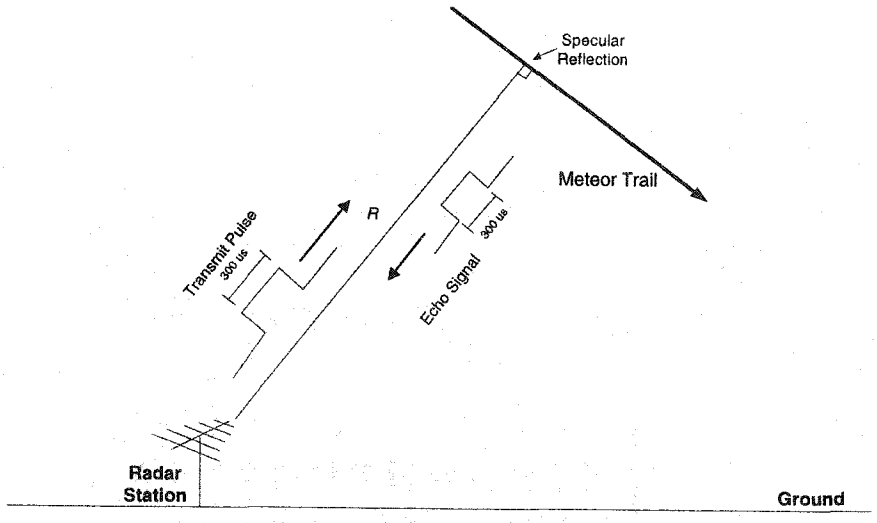

Figure 36: Geometry of backscatter from a meteor trail

When the 300 μs pulse typically used on the Kodiak system is incident on a meteor trail, it reflects specularly as a 300 μs pulse. If the echo signal is sampled several times within the reflected pulse, the shape of the pulse becomes evident, and the echo pulse profile can be used to separate meteor echoes from ionospheric echoes. Also, the leading edge of the echo pulse can be used for high spatial resolution edge detection of the meteor echo.

Oversampled meteor echo detection

The new capabilities of the digital receiver allow it to be used to oversample the echo signals during typical operation. For the detection and collection of meteor scatter data for the generation of wind profiles in the meteor region, some special processing software has been implemented on the HF radar at Kodiak. This software, which runs concurrently with most other radar operating modes, exploits the new receiver channels and their capabilities for meteor detection purposes.

Since normal operation of the radar requires the use of two of the GC214s four receiver channels, two channels are available for other uses. The new radar data collection and processing system uses these two channels for meteor scatter data

Reproduced with permission of the copyright owner. Further reproduction prohibited without permission.

collection. In the meteor software, one channel is allocated the main array of the radar, and the other is allocated to the interferometry array. In the current version of the radar software, these channels implement 10x oversampling. Typically, the radar transmits a 300 μs pulse, has a receiver filter bandwidth of 3.333 kHz and has an output data rate of 3.333 kHz. The meteor data collection and processing software sets the two unused receiver channels with a filter bandwidth of 33.33 kHz and an output sample rate of 33.33 kHz. With these settings, a meteor echo should have the shape of the transmit pulse and should contain 10 samples. This is evident when the magnitude of the raw samples of a meteor echo is examined. Figure 37 shows the echo magnitude profile of a meteor echo.

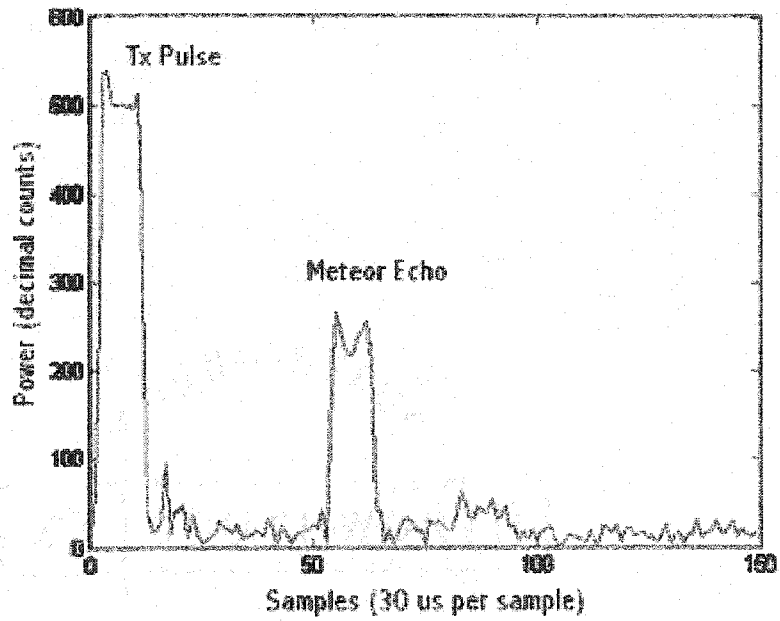

Figure 37: Meteor echo profile from baseband samples collected at 33.33 kHz

Since the new digital receiver is triggered off of the scope synchronization signal, data collection starts before the transmit pulse is transmitted. This allows the transmit pulse to be observed, as illustrated in the figure. It should be noted that the transmit pulse is not sampled directly, but is separated from the receiver by several stages of Tx/Rx switches. The transmitter pulse shown in Figure 37 is the signal that has leaked through these

Reproduced with permission of the copyright owner. Further reproduction prohibited without permission.

Tx/Rx switches. Figure 37 also clearly show the transmit pulse width of 300 μs and the meteor echo pulse width of 300 μs.

Range Resolution

Using the new digital receiver, the receiver filter bandwidth can be increased to greater than 1 MHz, which would provide a very small range resolution. Unfortunately, however, the FCC transmission bandwidth allocation allows a bandwidth of only 22 kHz for the radar transmissions. For this reason, there is a 22 kHz filter on the output of the radar transmitter. Since the filter bandwidth of the receiver is set to 33.33 kHz and the sample rate is 33.33 kHz, and the transmitter filter bandwidth is only 22 kHz, the rise and fall times of the transmit pulse can also bee seen in Figure 37. This transmitter bandwidth is now the limiting factor for attainable range resolution for the edge detection of meteors. Substituting the transmitter filter bandwidth into equation 39 describes the minimum attainable range resolutions as a function of echo signal-to-noise ratio. The minimum attainable range resolutions are provided in Table 6 for a series of SNRs.

Reproduced with permission of the copyright owner. Further reproduction prohibited without permission.

Table 6: Edge detection range error (resolution) as a function of SNR for the new digital receiver system

SNR (dB)	Time error (s)	Range Error (m)
0	2.27E-05	6818
2	1.81E-05	5416
4	1.43E-05	4302
6	1.14E-05	3417
8	9.05E-06	2714
10	7.19E-06	2156
12	5.71E-06	1713
14	4.53E-06	1360
16	3.60E-06	1081
18	2.86E-06	858
20	2.27E-06	682
22	1.81E-06	542
24	1.43E-06	430
26	1.14E-06	342
28	9.05E-07	271
30	7.19E-07	216
32	5.71E-07	171
34	4.53E-07	136
36	3.60E-07	108
38	2.86E-07	86

When compared with the achievable range resolutions for the old receiver system, as presented in Table 3, it is clear that the new digital receiver more than doubles the achievable resolution for a given SNR. It should also be noted that these range errors apply to using a threshold crossing edge detection of the target echo. This range error can be increased significantly by fitting the measured rise of the echo to the known rise of the transmit pulse. This technique, however, has not yet been implemented on the radar at Kodiak and is not presented.

Target Discrimination

The only two major scattering sources in the meteor region are meteor trails and E-region ionospheric field-aligned irregularities. A number of people (i.e. [Hall, et al., 1997], [Dai, 2000], etc) have developed methods for separating meteor echoes from these

Reproduced with permission of the copyright owner. Further reproduction prohibited without permission.

E-region ionospheric echoes in the typical SuperDARN data sets. These methods use assumptions about the statistical characteristics of meteor scatter and ionospheric scatter to discriminate between them. None of these methods however, use the echo profile as the means of discrimination. The new digital receiver allows the time profile of the echoes to be measured. Since the meteor trails are not distributed spatially in range from the radar, the meteor echoes appear as a reflected radar pulse. The E-region field-aligned irregularities, however, are distributed in range, and reflect a spatially distributed pulse. Also, due to potential constructive and destructive interferences within the distributed target, the amplitude of the echo signal is unpredictable. This is evident when a meteor echo and E-region ionospheric echo profiles are examined as presented in Figure 38.

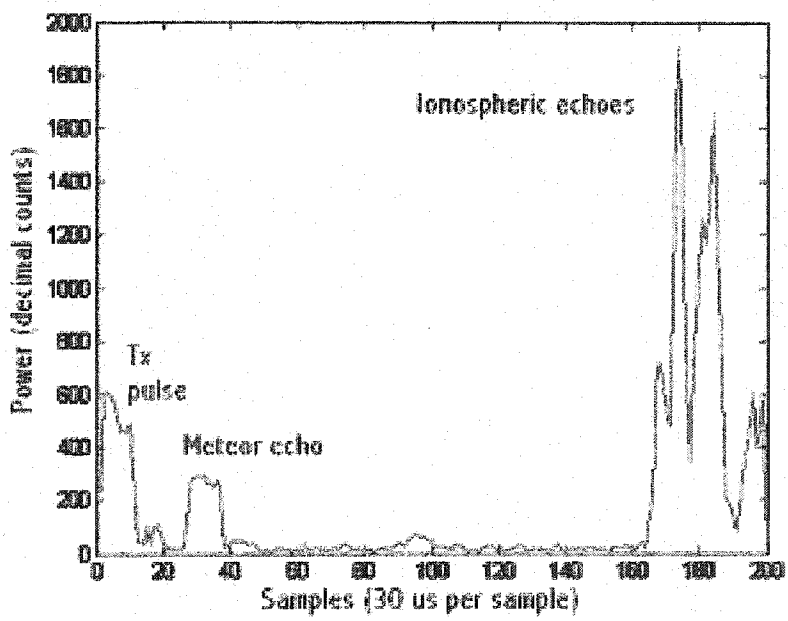

Figure 38: Meteor and Ionospheric echo profile from baseband samples collected at 33.33 kHz

Here it is clear that the meteor echo has the same shape, or time profile, as the transmit pulse. The ionospheric scatter, however, does not. Using the time profile of the echo signals is a very good means of discriminating meteor echoes from ionospheric echoes. Prior to the installation of the new digital receiver, the sampling frequencies and receiver

Reproduced with permission of the copyright owner. Further reproduction prohibited without permission.

filter bandwidths required to discriminate targets based on the echo time profile were not achievable.

Meteor detection algorithm

As has been mentioned, meteor detection and processing software is running concurrently with the existing radar control programs on the radar at Kodiak Island. This software collects baseband samples from the two unused receiver channels, which are set with a bandwidth of 33.33 kHz and a sample rate of 33.33 kHz. There is an algorithm that searches the baseband samples looking for meteor echoes in the baseband data.

In typical operation, the HF radar at Kodiak transmits a sequence of seven unequally spaced pulses. The pulse sequence is shown in Figure 21. To avoid range aliasing problems, the meteor detection algorithm searches only the samples collected between the transmission of the first pulse and the transmission of the second pulse. The algorithm searches for meteor echoes only in samples that correspond in range to the meteor region. In typical operation, the meteor detection algorithm searches the first 155 samples, corresponding to a range of 700 km, for meteor echoes. The algorithm begins by calculating a measure of the noise in the sampled signal. The noise is taken as the average of the lowest 30 sample amplitudes. The noise is then divided into the echo samples to provide a measure of the signal-to-noise ratio. The sample time series, expressed as SNR is then differentiated, and a difference value of greater than 4 dB is taken to indicate the potential leading edge of a meteor echo. Once the algorithm has identified the potential leading edge of a meteor trail, the algorithm then looks for a trailing edge 300 μs after the leading edge. This discriminates all echoes that have the same width as the transmit pulse. To further discriminate the meteor echoes from other echoes or spurious noise, the algorithm searches the samples between the leading edge and the trailing edge. If any of these samples drop below 4 dB SNR, then the echo is considered not a meteor echo and is discarded. If all of the echo samples between the leading edge and trailing edge are above the 4 dB threshold, then the algorithm makes

Reproduced with permission of the copyright owner. Further reproduction prohibited without permission.

sure the amplitude of those samples does not fluctuate more than 50% from their average. If all of these criteria are met, then the echo is considered a meteor echo. This algorithm simply sets some threshold values, and then looks for a 300 μs pulse in the echo signal. A detection threshold of 4 dB was chosen because the sample rate of 30 ms corresponds to a range of 4.5 km, and Table 6 shows that for SNRs of less than 4 dB, the range error is greater than 4.5 km.

Meteor data processing

Once a meteor has been detected in the baseband data, meteor echo processing begins. For each meteor echo, parameters such as range, velocity, angle of arrival (AOA), height, and average SNR are calculated and recorded. The methods by which these parameters are calculated are presented.

Range

The range is simply taken as the range to the leading edge of the meteor echo. In typical operation, the meteor detection sample rate is 33.33 kHz, which corresponds to a range resolution of 4.5 km. Since the edge detection threshold in the meteor echo detection algorithm is 4 dB SNR, the range error of a detected meteor is less than 4.5 km.

Velocity

The velocity of the meteor trail is essential for the determination of neutral winds in the meteor region. Velocity information is derived from the time varying phase of the complex autocorrelation function of the echo signal. To get the velocity, the complex autocorrelation must be calculated. Fortunately, the meteor detection and processing software operates concurrently with the normal radar control programs. In normal operation, the radar transmits a multi-pulse sequence to generate the autocorrelation functions of the ionospheric echoes. Formulation of the autocorrelation from the multi-

Reproduced with permission of the copyright owner. Further reproduction prohibited without permission.

pulse sequence was presented in chapter 2. When a meteor is detected, the autocorrelation function is calculated for a range corresponding to the middle of the echo pulse. A measured autocorrelation for a meteor is provided in Figure 39 as an example.

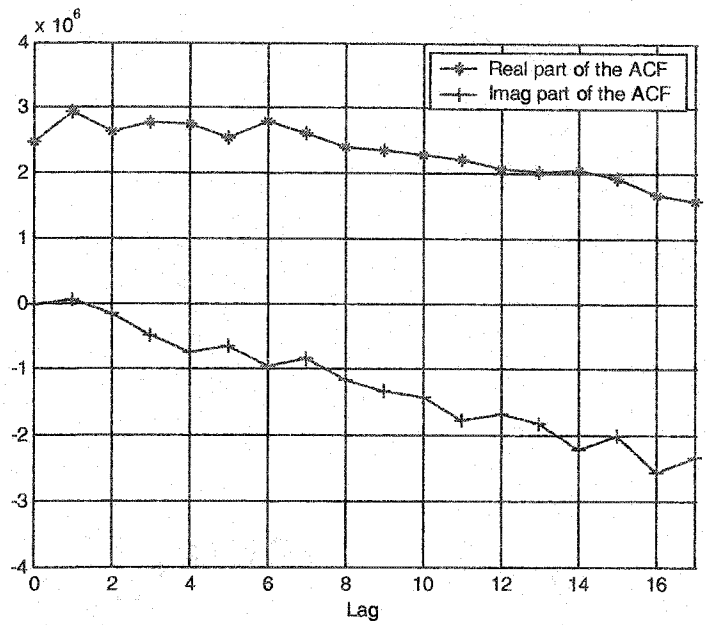

Figure 39: Measured autocorrelation of a meteor echo

The real part of this autocorrelation is calculated from equation 28 and the imaginary part is calculated from equation 29. The phase, ϕ_{ACF}, of the auto correlation can be determined for each lag using the relation

$$\phi_{ACF}(\tau) = \tan^{-1}\left(\frac{\mathrm{Im}(R_{xx'}(\tau))}{\mathrm{Re}(R_{xx'}(\tau))}\right). \qquad (52)$$

The phase of the autocorrelation function of a meteor echo shown in Figure 39 is shown in Figure 40.

Reproduced with permission of the copyright owner. Further reproduction prohibited without permission.

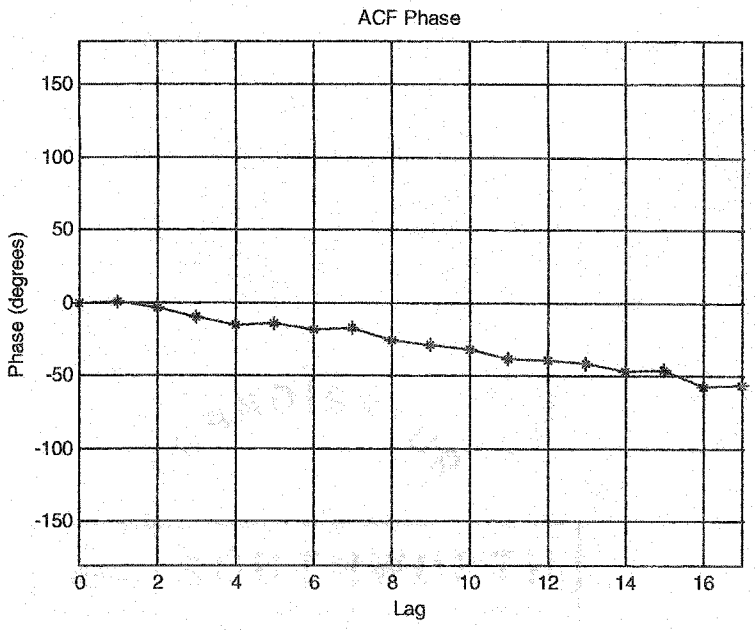

Figure 40: Phase of a complex autocorrelation of a meteor echo

The Doppler frequency, f_d, of the echo signal is simply the derivative of this phase with respect to time, as indicated by the relation

$$f_d = \frac{d\phi_{ACF}}{dt}. \tag{53}$$

The line-of-sight (LOS) velocity, v_{LOS}, of the meteor trail can be determined from the Doppler frequency using equation 22. The Doppler frequency of the meteor echo example shown in Figure 39 and Figure 40 is 3.88 Hz, which, at the radar frequency of 10.453 MHz, corresponds to a LOS velocity of 56 m/s. This means that the meteor has a velocity component toward the radar of 56 m/s.

In the radar processing software, the complex ACF is calculated for every meteor detected. Since the LOS velocity of the meteor trail should remain constant over the duration of a single pulse group, which lasts 64.8 ms, the phase of the complex ACF should be linear. To better discriminate meteor echo data from noise, a line is fit to the phase of the ACF. The slope of this line is used to calculate the Doppler frequency and corresponding Doppler velocity. The standard deviation of the phase data from the fitted line is recorded as an indication of the error in the velocity measurement. Fits with

Reproduced with permission of the copyright owner. Further reproduction prohibited without permission.

standard deviations greater than 0.3 radians are considered erroneous and no data is recorded for the echo. At the radar frequency of 10.453 MHz as in the example, a worst-case standard deviation of 0.3 radians corresponds to a velocity uncertainty of 16 m/s.

Angle of arrival

The HF radar at Kodiak employs an interferometer to determine the angle of arrival of a meteor echo signal. In the new implementation of the digital receiver, two receiver channels are dedicated to meteor echo detection. One is connected to the main array of the radar and the other is connected to the secondary, or interferometry array. Once a meteor has been detected, the complex crosscorrelation, R_{XY}^{*}, of the signals received at the main array and the interferometry array is calculated for that meteor echo. The crosscorrelation function (XCF) of the meteor echo used in the previous examples is shown in Figure 41.

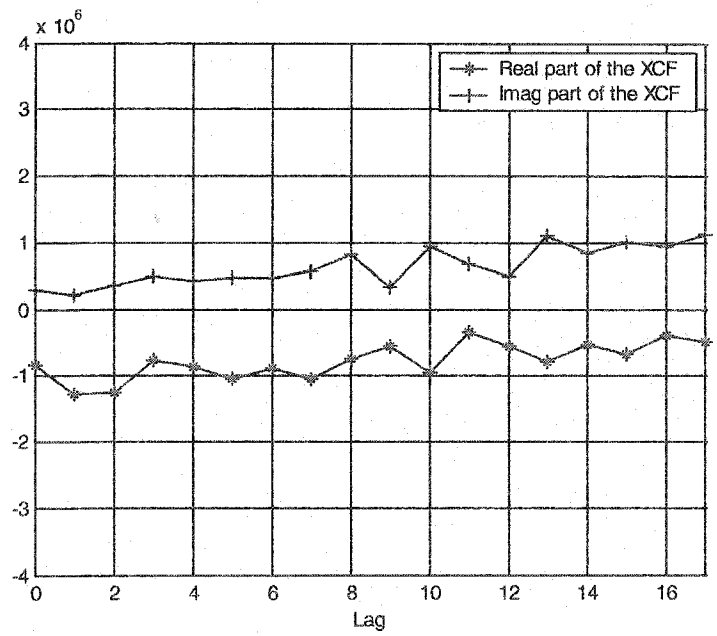

Figure 41: Measured crosscorrelation of a meteor echo

The phase, ϕ_{XCF}, of the crosscorrelation function can be calculated using

Reproduced with permission of the copyright owner. Further reproduction prohibited without permission.

$$\phi_{XCF}(\tau) = \tan^{-1}\left(\frac{\mathrm{Im}(R_{XY'}(\tau)}{\mathrm{Re}(R_{XY'}(\tau))}\right). \quad (54)$$

The phase difference, $\Delta\phi$, between the meteor echo received at the two arrays is simply

$$\Delta\phi(\tau) = \phi_{ACF}(\tau) - \phi_{XCF}(\tau). \quad (55)$$

This phase difference can then be applied to equation 43 to calculate the difference in range, Δr, between the meteor trail and the two arrays. This range difference can then be applied to equation 40 to calculate the angle of arrival. However, since the spacing, d, between the main array and the interferometry array is 100 meters, which is greater than half the shortest wavelength of the radar, there can be some ambiguity in the angle of arrival. Several possible angles of arrival can arise for a single measured phase difference.

The ambiguity in the angle of arrival can be limited by setting practical limits on possible values of the angle of arrival. Radar meteor echoes typically occur in an altitude range between 70 km and 130 km. By combining the range measurement of a meteor echo with the several possible angles of arrival, several possible echo reflection altitudes can be calculated. Any calculated altitudes that do not fall within the meteor region of 70-130 km can be discarded. This greatly limits the ambiguity in the angle of arrival measurement. Unfortunately, however, it does not remove all ambiguities. Figure 42 shows the received phase difference, $\Delta\phi$, for potential meteor echo ranges and altitudes.

Reproduced with permission of the copyright owner. Further reproduction prohibited without permission.

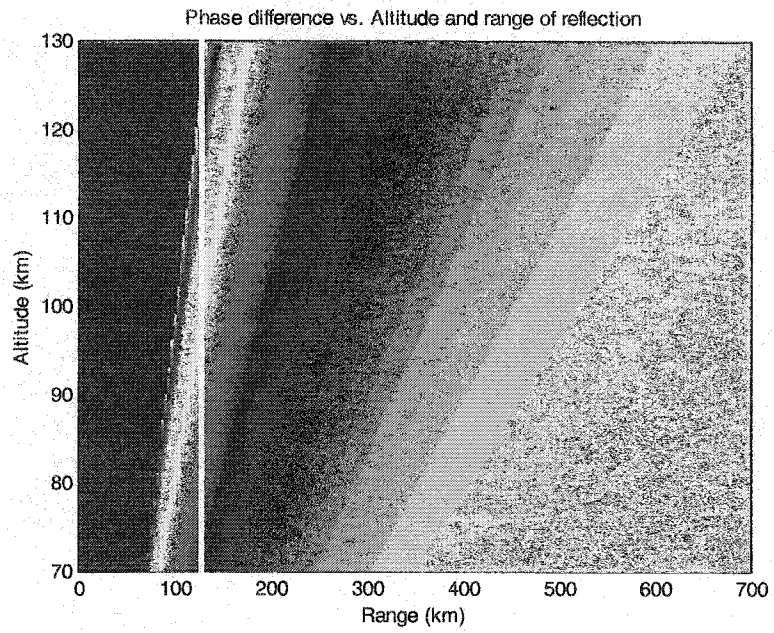

Figure 42: Interferometric phase differences at 10 MHz for echoes from the meteor region at ranges from 0 to 700 km

This figure clearly shows that for the indicated range of 120 km, the same interferometric phase indicates multiple possible echo altitudes. The echo locations, as a function of range and altitude, which present no altitude ambiguities can be calculated and are presented in Figure 43.

Reproduced with permission of the copyright owner. Further reproduction prohibited without permission.

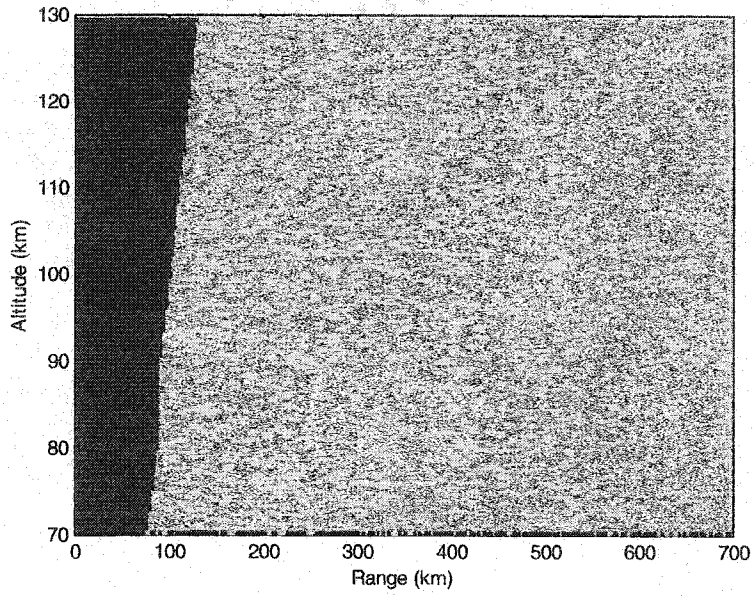

Figure 43: Unambiguous meteor echo locations as a function of altitude and range for a radar frequency of 10 MHz

The figure shows meteor echo locations as a function of range and altitude that correspond to unambiguous angles of arrival. The light regions on the figure represent the meteor echo locations for which there is no AOA ambiguity. While the AOA ambiguity does limit the number of detected meteor echo that can be located spatially with certainty, there are still many meteor echoes that can be located with certainty.

The current implementation of the meteor echo processing software calculates the ACF of the meteor echo, and fits a line to the phase of that ACF, as has been mentioned. The software then calculates the XCF of the echo between the main array and the interferometry array. A line with the same slope as that fitted to the ACF phase, is then fitted to the XCF phase. If the standard deviation of the XCF phase from the fit is greater than 0.3 radians, then the meteor echo is considered bad and is discarded. If the standard deviation is less than 0.3 radians, then the phase difference between the ACF and XCF is averaged over τ. This average phase difference is taken as the phase difference between the front array and interferometry array and the AOA is calculated. Currently, the processing software calculates the range difference, Δr, with equation 43. The AOA is

Reproduced with permission of the copyright owner. Further reproduction prohibited without permission.

then calculated using equation 40. If the meteor echo does not fall within the meteor region limits of 70-130 km altitude, the Δr is incremented by λ until the echo origin does map into the meteor region. When the meteor maps into the meteor region, the AOA is recorded. Currently there is no provision in the processing software to handle echoes that can map into the meteor region multiple times. If an echo does map into the region multiple times, the lowest altitude within the region is recorded. The original phase difference, however, is always recorded, and can be used in post processing to identify and filter echoes that have an AOA ambiguity.

SNR

The signal to noise ratio of all of the detected meteors is recorded as a parameter of the meteor. Since the meteors are detected with a detection threshold of 4 dB, there are no meteors that have a recorded SNR of less than 4 dB. Once a meteor echo has been identified by the detection software, and has been found to have an acceptable ACF and XCF phase fit, and has been successfully mapped into the meteor region, the SNR for that meteor is calculated. The recorded SNR for a meteor echo is simply the integration measured SNR values over the pulse width of echo pulse.

Final data product

The final data product of the meteor detection and processing software is a meteor data file. The meteor data file contains a detailed record of all acceptable meteor echoes. This record contains a timestamp with the year, day, month, hour, minute, and second of the echo detection. The record also contains radar beam number and RF wavelength at the time of the detection. Also recorded are the calculated parameters of the echo, such as the range of the echo, phase difference between the main array and interferometry array, the AOA, the LOS velocity, the altitude of the echo, the SNR, the standard deviations of the fits to the ACF and XCF phase, and the measured ACFs and XCFs. A

Reproduced with permission of the copyright owner. Further reproduction prohibited without permission.

data record is created for all acceptable meteor events. It should be noted that a meteor event is considered the detection of a single meteor echo within a single pulse sequence. There can be a record for several meteor echoes, at different ranges, within a single pulse sequence. Also, there are typically 10 pulse sequences transmitted every second, so if a meteor trail persists for more than 100 ms, as is often the case, there may be several records for the same meteor trial. The record size is 368 bytes for each meteor event, and is recorded as binary data files. These files are stored on the main computer at the radar site on Kodiak Island, and are available for download from the radar site.

These data files provide a detailed record of each good meteor echo event. The data files can be used in post processing for any number of experimental purposes. The purpose for which these records have been created, however, is the determination of meteor region wind profiles.

Meteor echo statistics

The meteor detection and processing software has been running continuously on the HF radar at Kodiak since April 5, 2003. In that time some meteor echo statistics have been collected and analyzed. These statistics are presented briefly in the following sections.

Hourly Meteor Event Distribution

Since it was implemented, the meteor detection system has identified on average more than 40,000 meteor events per day. As is expected, more meteors events are identified in the local morning than in the local evening. Figure 44 shows the hourly numbers of detected meteors for a typical day of meteor echo data collection.

Reproduced with permission of the copyright owner. Further reproduction prohibited without permission.

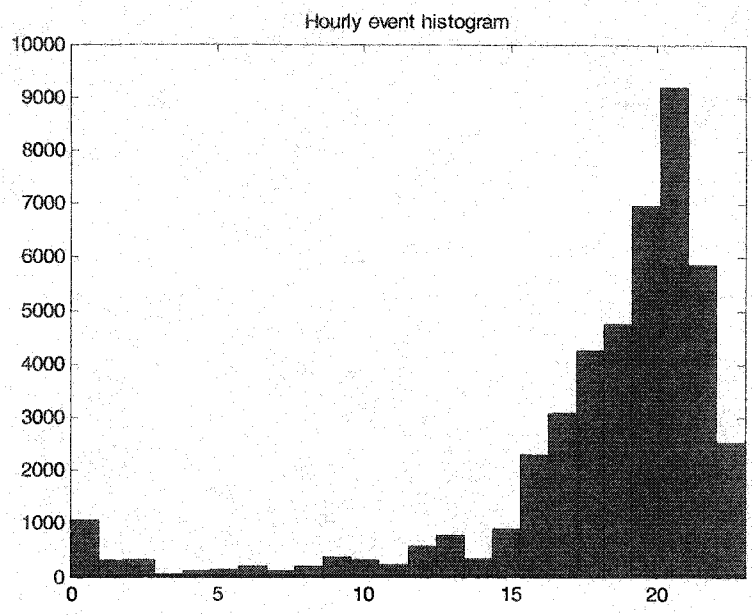

Figure 44: Typical hourly distribution of meteor echo events

The time axis is represented in Universal Time (UT). Since Alaska is eight hours behind UT, this figure shows a peak in meteor detection in the local morning, and a lull near local evening.

Meteor echo range distribution

The range over which the meteor detection algorithm searches for meteors is 70-700 km. The range limit of 700 km was chosen based on the lowest possible look angle of the radar above the horizon. The range limit of 700 km corresponds to an altitude of 70 km at the minimum AOA of 6°. When the range statistics of meteor echoes are observed, however, it is evident that this range limit is far greater than the practical range limit of meteor echo detection. The range distribution of meteor echoes for a typical day is shown in Figure 45.

Reproduced with permission of the copyright owner. Further reproduction prohibited without permission.

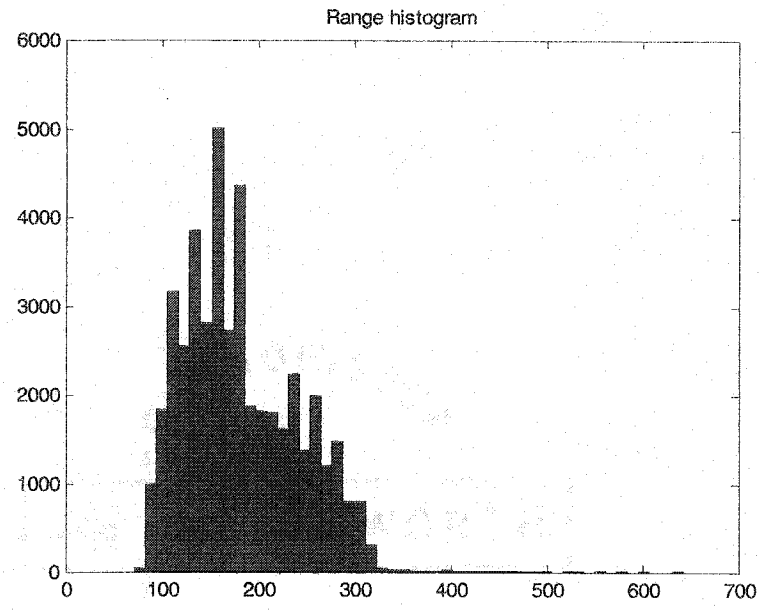

Figure 45: Typical daily meteor echo range distribution

This shows that there are no meteors detected below 70 km altitude and that there is a practical limit of meteor detection range at roughly 320 km. This range distribution also indicates that the peak range of meteor echo detection is between 140 and 150 km. This corresponds well with the radar geometry with a peak elevation beam angle of 27° and the expected peak meteor echo elevation of 95 km.

Altitude distribution

The meteor algorithm records data for an echo only of the reflection altitude of the echo can be mapped into the meteor altitudes of 70-130 km. Figure 46 shows the distribution of meteor echoes within this region.

Reproduced with permission of the copyright owner. Further reproduction prohibited without permission.

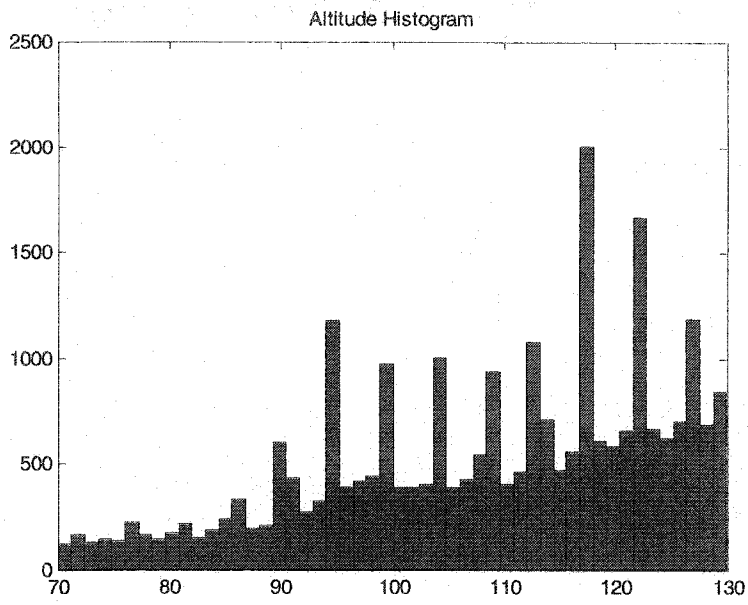

Figure 46: Typical daily meteor echo altitude distribution

This altitude distribution shows that the number of meteor echo detections increases with altitude. A typical altitude distribution of meteor trails for a radar frequency of 10 MHz would show a peak of meteor trails at about 100 km. Since the meteor detection algorithm, however, may count a echoes from a single meteor trial multiple times, the distribution shown in Figure 46 is not a meteor trail distribution, but is a distribution of detected meteor events as previously defined.

SNR distribution

Since the signal-to-noise ratio is a measure of the range uncertainly, the SNR statistics are of interest. Since the detection threshold of the meteor echoes is set at 4 dB, there are no meteors detected with an SNR below that threshold. The practical upper limit of meteor echo SNRs is shown in the typical daily distribution of the SNR measure of the meteor echoes is provided in Figure 47.

Reproduced with permission of the copyright owner. Further reproduction prohibited without permission.

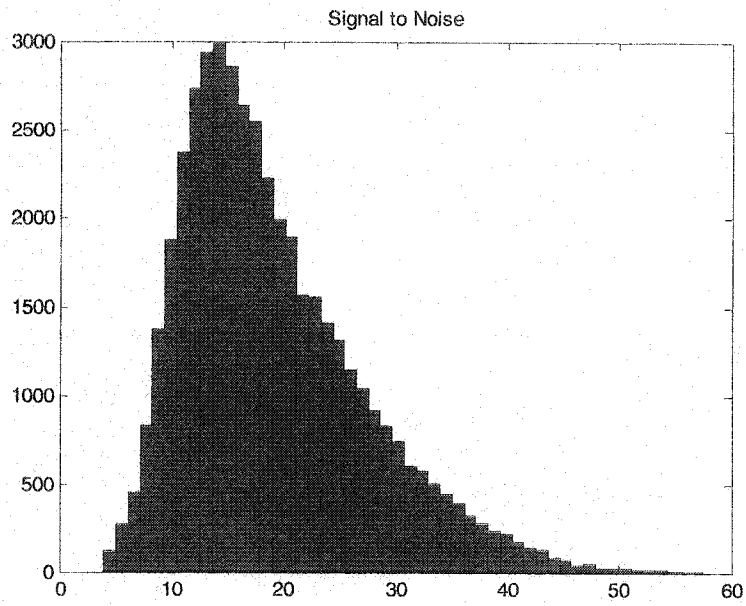

Figure 47: Typical daily meteor echo SNR distribution

This indicates that the SNR distribution of meteor echoes tapers off at higher SNRs. It is evident, however, that echoes with SNRs of greater than 30 dB are not uncommon. This distribution also shows that the peak SNR of the meteor echoes detected is 14 dB, which corresponds to an average range uncertainty of 1.36 km. It should be noted that this distribution does not represent the SNR distribution of meteor echoes in general, but rather indicates the distribution of the echoes detected by the meteor detection and processing software on the HF radar at Kodiak. This distribution represents only those meteor echoes that were detected, had good fits to the ACF phase and XCF phase, and could be mapped into the altitude region of 70-130 km.

Deriving meteor region wind profiles from the meteor echo data

While one of the primary goals of the research presented in this thesis is to develop a system to gather high spatial resolution meteor echo data, one of the secondary goals is to use that data to derive wind profiles in the meteor region. The large number of

Reproduced with permission of the copyright owner. Further reproduction prohibited without permission.

meteor events detected per day and the large data set of meteor echo measurements provide a good base for the post processing derivation of meteor region winds. Some preliminary post processing has been performed to explore the derivation of meteor region winds from the meteor echo data and the results are presented.

Since greater than 40,000 meteor events are detected daily, and each meteor event record includes an altitude of refection and a line of sight velocity, there is a very large data set from which to derive the meteor region winds. One typical meteor region wind data product is hourly meridional and zonal wind velocities. Several researchers, (i.e. [Hall et al., 1998] and [Dai, 2000]) have developed method for deriving such hourly meridional and zonal wind velocities from previously existing SuperDARN data. These meridional and zonal winds can also be derived from the new meteor data.

If the meteor region winds are assumed to be constant over the field of view of the radar, and the winds are assumed to be horizontal in direction, such that there is no vertical component of the wind velocity, then the velocities measured at the different beam look directions can be used to derive the meridional and zonal winds. Using a singular value decomposition method similar to that employed by Dai [2000], and averaging the measured meteor echo velocities over beam direction and time, yields hourly measures of the meridional and zonal winds. The derived hourly meridional and zonal winds for April 9, 2003 are shown in Figure 48.

Reproduced with permission of the copyright owner. Further reproduction prohibited without permission.

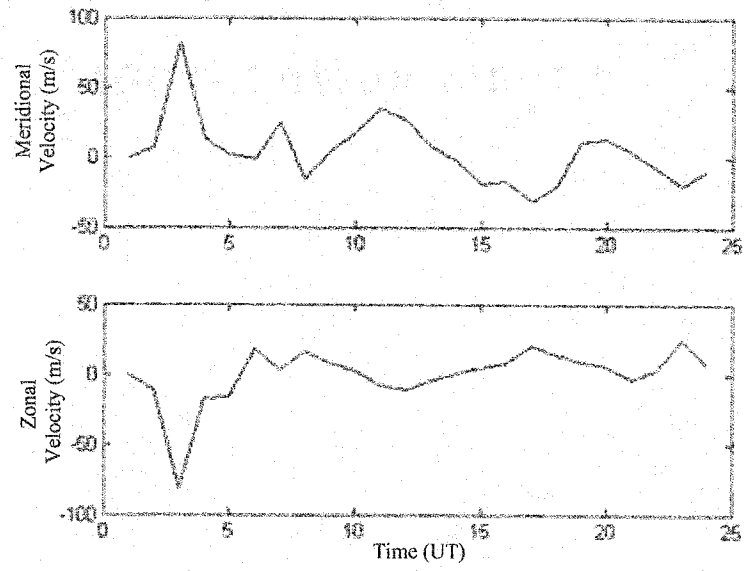

Figure 48: Hourly meridional and zonal winds for April 9, 2003

The data shown in Figure 48 is derived by assuming there is no vertical component of the velocity, and finding the horizontal velocity toward the radar, v_h, from the LOS velocity with the equation

$$v_h = \frac{v_{LOS}}{\cos(\alpha)}, \tag{56}$$

where α is the angle of arrival. The horizontal velocities are then averaged beam direction for every hour, and the equation

$$\begin{bmatrix} v_0 \\ \vdots \\ v_{15} \end{bmatrix} = \begin{bmatrix} \cos(\theta_0) & \sin(\theta_0) \\ \vdots & \vdots \\ \cos(\theta_{15}) & \sin(\theta_0) \end{bmatrix} \begin{bmatrix} v_M \\ v_Z \end{bmatrix}, \tag{57}$$

where v_0 through v_{15} are the beam averaged velocities, is solved using a singular value decomposition for the meridional velocity, v_M, and the zonal velocity, v_Z.

Using the altitude measurements of the recorded meteor echo data, an altitude profile of the winds in the meteor region can be created. To get a wind profile, the meteor echoes collected over an hour are grouped into altitude bins of 5 km altitude, and the meteor echo velocities are averaged with these bins. These averaged velocities then

Reproduced with permission of the copyright owner. Further reproduction prohibited without permission.

give a measure of the hour-averaged winds at the within the corresponding altitude bins. Figure 49 shows the derived wind profile in the meteor region for 1:00 to 2:00 UTC on April 9, 2003.

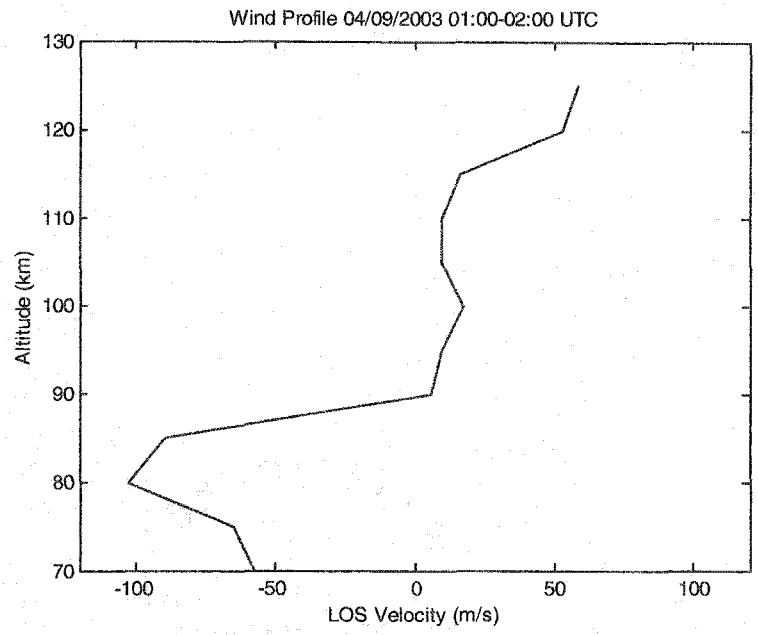

Figure 49: Wind profile for 1:00-2:00 UTC on April 9, 2003

Applying this method to an entire day of meteor echo data provides a plot showing changed in the winds profile over the course of the day. Figure 50 shows the hourly wind profiles for April 9, 2003.

Reproduced with permission of the copyright owner. Further reproduction prohibited without permission.

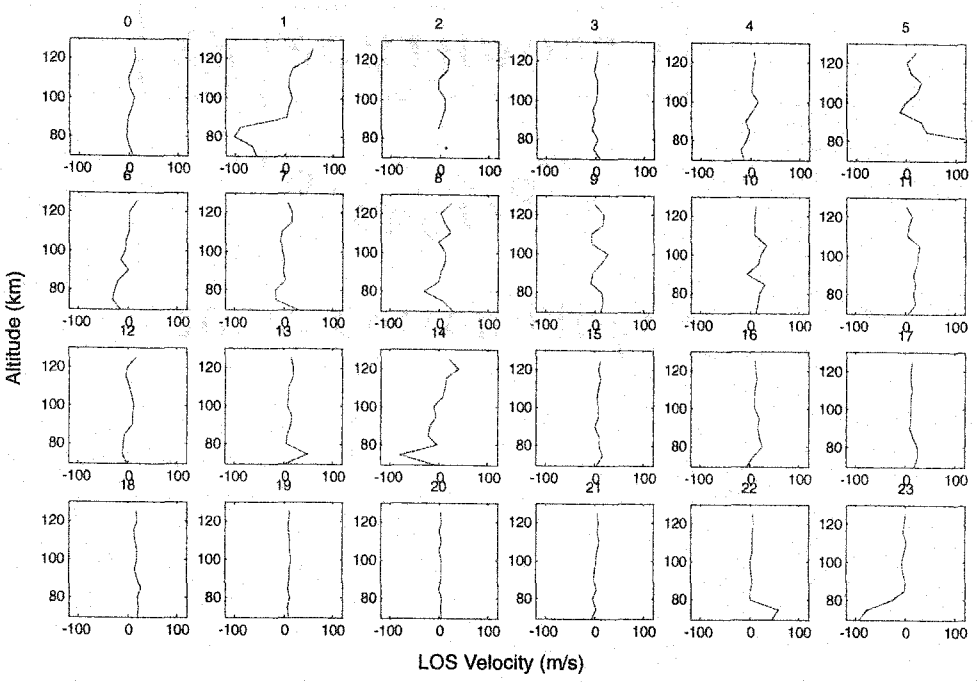

Figure 50: Hourly wind profiles for April 9, 2003

This figure shows only the LOS velocities in the meteor region. Using the singular value decomposition method in conjunction with the beam directions, the meridional and zonal wind profiles can be generated. However, this is not presented.

This presentation of the derived meteor wind profiles simply provides some examples of how the meteor region winds can be derived from the meteor echo data recorded by the software implemented on the HF radar at Kodiak. Much more development is required to create a refined meteor region wind profile data product. With the high rate of detected meteor echoes it is conceivable that a realtime wind profile data product with a time resolution on the order of minutes could be created. This is one of the goals for the future development of this system.

Reproduced with permission of the copyright owner. Further reproduction prohibited without permission.

Chapter 6: Conclusions and suggestions for future improvement

The new digital receiver in the HF radar at Kodiak has successfully been incorporated into the radar system, and seems to work well. This new receiver greatly increases the experimental flexibility of the radar and allows much greater user control of the receiver parameters.

A meteor echo detection and processing system has been implemented, and has been collecting meteor echo data since April 5, 2003. The data collected by this system has many experimental uses, and should find application for some time. However, there are some significant improvements that can be made to this collection system that would increase the research applications of the meteor data.

Suggested improvements to the digital receiver system

One significant problem with the digital receiver system as it is currently implemented on the HF radar at Kodiak is the receiver noise figure on the receiver path for the interferometry array. The receiver noise figure for the interferometry array could drastically be improved by placing a more effective Tx/Rx switch between the antennas and the GC214 digital receiver card. This would eliminate the unbiasing effect on the existing low-power Tx/Rx switch and would allow the removal of 10 dB of attenuation in the receive path. Also, the implementation of low noise pre-amplifiers on the interferometry array would place a low noise amplifier before the significant loss of the phasing matrix in the receive path. The net result of Tx/Rx switches and pre-amplifiers would be a reduction of greater than 20 dB in the noise figure of the receiver for the interferometry array. This would significantly increase the signal to noise ratio for the meteor echoes on the interferometry array and would provide better crosscorrelation data. This would in turn decrease the number of meteor echoes discarded due to bad XCF fits.

Reproduced with permission of the copyright owner. Further reproduction prohibited without permission.

There are currently plans to install Tx/Rx switches and pre-amplifiers on the antennas of the interferometry array in August of 2003.

Another improvement that is planed for the new receiver system is the inclusion of a highpass filter with a cutoff of 8 MHz between the phasing matrix and the GC214. This would eliminate the high power transmitter signals from the AM radio band and would eliminate all signals below the operating frequencies of the radar.

Suggested improvements to the meteor detection and processing system

Currently, there is no discrimination between underdense and overdense echoes. Implementing a time series analysis algorithm that searches the echo data for the signature exponential decay in underdense meteor echo power would allow the decay times of underdense echoes to be measured and recorded. These decay times could then be used to derive useful information such as temperature or density. Combining such measurements with the altitude information currently collected, it is conceivable that the radar could be used to derive temperature or density profiles within the meteor region. The underdense echo decay times could also be used to limit the potential echo reflection altitudes. This would put greater altitude constraints than the currently used 70-130 km on the reflection altitudes, which would decrease the ambiguities in altitude due to the interferometry spacing.

The range certainty of the meteor echo detections could be improved by collecting high speed samples and fitting the known rise of the echo pulse to the measured echo pulse rise. The range certainty would no longer depend on the SNR of the echo signal, but on the goodness of fit of the leading edge of the echo pulse. With the sampling speed capabilities of the new receiver, range certainties of less than 1 km should be attainable.

Reproduced with permission of the copyright owner. Further reproduction prohibited without permission.

Bibliography

Aalfs, D. Bailey. **Model 608 Log-Periodic Antenna 8-20 MHz ST-50 KDHB Tower: Instruction Manual**. Sabre Communications Corporation. Sioux City, IA, 51102.

Analog Devices. **Data Sheet: AD6644-65 Rev. 0**. Analog Devices. Norwood, MA, 02062. 2000.

Baker, Kile. **FITACF: A SuperDARN Tutorial.** SuperDARN Workshop, Valdez. May 2002.

Barnes, R. J. **Radops 2000 Reference Manual**.

Chen, Francis F. **Introduction to Plasma Physics and Controlled Fusion; Volume 1: Plasma Physics, 2nd Ed**. Plenum Press. New York and London. 1984.

Childers, Donald G. **Probability and Random Processes**. Irwin. Chicago. 1997.

Dai, Wei. **Meteor Wind Wave Analysis of SuperDARN Observations**. Masters Thesis. University of Alaska Fairbanks. August 2000.

Echotek Corporation. **ECDR-GC214-PCI/TS User Manual: Revision 3.0**. Echotek Corporation, Huntsville, AL. 2001.

Farley, D. T. **Multi-pulse Incoherent-Scatter Correlation Function Measurements**. *Radio Science*. Vol. 7, No 6, pp 661-666. June 1972

Greenwald, R. A., K. B. Baker, J. R. Dudeney, M. Pinnock, T. B. Jones, E. C. Thomas, J.-P. Villain, J.-C. Cerisier, C. Senior, C. Hanuise, R. D. Hunsucker, G. Sofko, J. Koehler, E. Nielsen, R. Pellinen, A. D. M. Walker, N. Sato, and H. Yamagishi. **DARN/SuperDARN: A Global View of the Dynamics of High Latitude Convection**. *Space Science Reviews*. Vol 71, pp 761-796. 1995.

Greenwald, R. A., K. B. Baker, R. A. Hutchins, and C. Hanuise. **An HF phased-array radar for studying small-scale structure in the high-latitude ionosphere**. *Radio Science*. Vol. 7, No. 6, pp 63-79, Jan.-Feb. 1985.

Hall, G. E., J. W. MacDougall, D. R. Moorcroft, J.-P. St.-Maurice, A. H. Manson, and C. E. Meek. **Super Dual Auroral Radar Network observations of meteor echoes.**

Reproduced with permission of the copyright owner. Further reproduction prohibited without permission.

Journal of Geophysical Research, Vol 102, No. A7. pp 14603-14614. July 1, 1997.

Jones, W. **The decay of radar echoes from meteors with particular reference to their use in determination of temperature fluctuations near the mesopause.** *Annales Geophysicae.* Vol. 13. pp 1104-1106. 1995.

Kraus, John D. **Antennas**. 2nd Edition. McGraw-Hill. New York. 1988.

Kraus, John D. **Electromagnetics**. 4th Edition. McGraw-Hill. New York. 1992.

Lester, Mark, Steve Milan, Julian Thornhill, Chris Thomas, Jim Wild, and Tim Yeoman. **CUTLASS Tutorial.** *CUTLASS Workshop, University of Leicester.* December, 1998.

Levanon, Nadev. **Radar Principles**. John Wiley & Sons, Inc. New York. 1988.

McKinley, D. W. R. **Meteor Science and Engineering**. McGraw-Hill. New York. 1961.

McWilliams, Kathryn, D. Andre, R. Greenwald, A. Schiffler, G. Sofko, and T. Yeoman. **SuperDARN Pulse Sequences – Optimization and Testing**. SuperDARN Workshop, Finland. May 2003.

Mitra, Sanjit K. **Digital Signal Processing: A Computer-Based Approach, 2nd Edition**. McGraw-Hill Irwin. Boston. 2001.

Peebles, Peyton Z. Jr. **Radar Principles**. John Wiley & Sons, Inc. New York. 1998.

Texas Instruments. **Data Sheet: GC4016 Multi-standard Quad DCC Chip Rev. 1.0**. Grey Chip. Palo Alto, CA, 94306. 2001.

University of Leicester, Radio and Space Plasma Physics Group. **Software Organization Chart**. SuperDARN Page: A Guide to the SuperDARN Radar Systems and Software. http://ion.le.ac.uk/cutlass/superdarn.html. 2001.

Yukimatu, Sessai Akira, Tsutsumi Masaki. **A new SuperDARN raw time series analysis method and its application to mesopause region dynamics.** *Geophysical Research Letters.* Submitted 2002.

Reproduced with permission of the copyright owner. Further reproduction prohibited without permission.